

# **MEMS-Based System for Particle Exposure Assessment Using Thin-Film Bulk Acoustic Wave Resonators and IR / UV Optical Discrimination**

*Justin Phelps Black*



Electrical Engineering and Computer Sciences  
University of California at Berkeley

Technical Report No. UCB/EECS-2006-193

<http://www.eecs.berkeley.edu/Pubs/TechRpts/2006/EECS-2006-193.html>

December 22, 2006

Copyright © 2006, by the author(s).  
All rights reserved.

Permission to make digital or hard copies of all or part of this work for personal or classroom use is granted without fee provided that copies are not made or distributed for profit or commercial advantage and that copies bear this notice and the full citation on the first page. To copy otherwise, to republish, to post on servers or to redistribute to lists, requires prior specific permission.

MEMS-Based System for Particle Exposure Assessment Using Thin-Film Bulk  
Acoustic Wave Resonators and IR / UV Optical Discrimination

by

Justin Phelps Black

B.S. (University of Virginia) 1995

M.S. (University of California Berkeley) 2005

A dissertation submitted in partial satisfaction of the

requirements for the degree of

Doctor of Philosophy

in

Engineering – Electrical Engineering and Computer Sciences

in the

Graduate Division

of the

University of California, Berkeley

Committee in charge:

Professor Richard M. White, Chair

Professor Albert P. Pisano

Professor Kristofer S. J. Pister

Fall 2006

The dissertation of Justin Phelps Black is approved:

---

Chair

Date

---

Date

---

Date

University of California, Berkeley

Fall 2006

MEMS-Based System for Particle Exposure Assessment Using Thin-Film Bulk  
Acoustic Wave Resonators and IR / UV Optical Discrimination

Copyright © 2006

by

Justin Phelps Black

## Abstract

MEMS-Based System for Particle Exposure Assessment Using Thin-Film Bulk

Acoustic Wave Resonators and IR / UV Optical Discrimination

by

Justin Phelps Black

Doctor of Philosophy in Engineering – Electrical Engineering and Computer

Sciences

University of California, Berkeley

Professor Richard M. White, Chair

Airborne particulates are responsible for severe adverse effects on human health, examples being the lung disease caused by tobacco smoke and severe asthmatic reactions to certain other particulates. Present instrumentation to measure such particulates is bulky, costly to purchase, and difficult to operate; its use in field studies usually requires sending samples collected to an analytical laboratory in order to identify the particulates. This dissertation describes a miniaturized MEMS particulate matter (PM) monitor that employs:

- the deposition of particulates from a sample stream onto a piezoelectric thin-film bulk acoustic wave resonator (FBAR) by means of thermophoresis;
- determination of the mass deposited by measuring the resonant frequency shift of the resonator; and,

- determination of the nature of the particulates from the absorption characteristics of the deposited film by the use of infrared and ultraviolet LED light sources and photodetectors.

Thermophoretic PM precipitation was implemented with a quartz / polysilicon heater that establishes a temperature gradient across the channel through which the sample flows. Under the test conditions, the rate of frequency shift for environmental tobacco smoke was approximately 1 kHz/min for a concentration of 400  $\mu\text{g}/\text{m}^3$ . Sensitivity to a PM concentration as small as 18  $\mu\text{g}/\text{m}^3$  was observed. The monitor has a volume of 250  $\text{cm}^3$ , a mass of 0.114 kg, and a power consumption <100 mW. With some minor redesign, the monitor could be made considerably smaller and lighter and to consume significantly less power.

---

Professor Richard M. White, Chair

Date

## Table of Contents

Abstract.....	1
Table of Contents .....	i
Acknowledgements .....	iv
1 Introduction .....	1
1.1 Measurement and Discrimination of Airborne Particulate Matter (PM)....	1
1.2 MEMS PM: MEMS-Based PM Detector Using Thin-Film Bulk Acoustic Wave Resonators (FBARs) and IR / UV Optical Discrimination.....	6
1.2.1 Thin-Film Bulk Acoustic Wave (FBAR) Technology .....	7
1.2.2 Thermophoretic Deposition.....	19
1.2.3 Optical Discrimination of PM Composition.....	21
1.2.4 Packaging .....	23
1.3 Aerosol Monitoring Experiments .....	24
1.4 Outline of Subsequent Chapters .....	26
1.5 Chapter 1 References.....	27
2 Principle of Operation of MEMS PM Monitor .....	37
2.1 FBAR Admittance and Mode Shape .....	37
2.1.1 Acoustically Thin Electrodes with PM Layer .....	44
2.1.2 Acoustically Thick Bottom FBAR Electrode.....	52
2.2 FBAR Admittance Derived from Transmission-Line Mason Model.....	56
2.3 FBAR Pierce Oscillator Analysis.....	62
2.3.1 Oscillator Loop Gain Analysis .....	62
2.3.2 Negative-Resistance Oscillator Model .....	67



2.4	Chapter 2 References.....	70
3	Fabrication and Characterization of MEMS PM Components.....	72
3.1	FBAR Microfabrication.....	72
3.1.1	ZnO FBAR Process Flow .....	72
3.1.2	AlN FBAR Process Flow .....	75
3.2	FBAR Electrical Characterization .....	79
3.2.1	ZnO FBAR Impedance .....	79
3.2.2	AlN FBAR Impedance .....	81
3.3	Calibration of ZnO FBAR Mass Sensitivity with Al Loading .....	85
3.4	ZnO FBAR Imaging with Optical Interferometry .....	87
3.5	AlN FBAR Mode-Shape Imaging with Novel Tapping-Mode Atomic Force Microscopy .....	90
3.6	FBAR Pierce Oscillator .....	99
3.6.1	MEMS PM FBAR Oscillator Performance .....	99
3.6.2	Analysis of Oscillator Startup .....	103
3.6.3	Oscillator Temperature Dependence .....	108
3.7	Fabrication and Characterization of Thermal Precipitator .....	109
3.8	Chapter 3 References.....	113
4	MEMS PM Calibration and Monitoring Experiments .....	114
4.1	Experimental Preliminaries .....	114
4.1.1	LBNL Environmental Chamber Test Setup .....	114
4.1.2	Generation of Challenge Aerosols.....	117
4.1.3	MEMS PM FBAR Mass Sensor Packaging .....	119

4.2	ETS Detection with MEMS PM Prototype .....	122
4.3	Calibration of the MEMS PM in the LBNL Environmental Chamber with ETS .....	124
4.4	MEMS PM FBAR Sensor Response to Fresh Diesel PM .....	130
4.5	Discrimination of PM Composition by Thermal Spectroscopy .....	133
4.6	Discrimination of PM Composition by Optical Interrogation.....	135
4.6.1	Reflectance-Based Optical Module .....	137
4.6.2	Transmission-Based Optical Module .....	140
4.7	Field Study in Berkeley Residence.....	143
4.7.1	Site Description, Instrumentation, and Experimental Methods.....	144
4.7.2	Aerosol Monitoring Protocols .....	147
4.7.3	Calibration of the MEMS PM monitor: Comparison of MEMS PM Monitor Response to Gravimetric Measurements of PM <sub>2.5</sub> and PM <sub>grav</sub> .....	148
4.8	Chapter 4 References.....	150
5	Conclusions .....	152

## **Acknowledgements**

I am indebted to Professor White for his unwavering support and guidance throughout my studies in BSAC. I'm grateful for the assistance and encouragement of Professors Al Pisano, Roger Howe, Kris Pister, Luke Lee, and Jeff Bokor, and owe particular gratitude to Professor Pister and Professor Pisano for reviewing this dissertation.

The project was a collaborative effort with Dr. Mike Apte, Dr. Lara Gundel, Dr. Rossana Cambie, Zhuo Zhang, and George Stern, all from Lawrence Berkeley National Laboratory. It was a distinct pleasure working with them all and the success of this project was a result of their hard work, creativity, and perseverance.

I reserve distinct accolades for many colleagues who directly facilitated the success of this project, including Noel Arellano, Sunil Bhave, Jonathan Foster, Brenda Haendler, Bert Liu, Dan McCormick, Veljko Milanovic, Brian Otis, Gianluca Piazza, Alvaro San Paulo, Phil Stephanou, and many others.

The assistance of Matt Wasilik, Bob Hamilton, Dr. Bill Flounders, Joe Donnelly, Xiaofan Meng, Helen Kim, Tom Parsons, Katalin Voros, John Huggins, Ruth Gjerde, Loretta Lutchter, Susan Kellogg, Richard Lossing, and many other BSAC, Microlab, and EECS staff is greatly appreciated.

I thank my father, mother, Olya, Edward, Helena and grandparents for their support and encouragement.

# **1 Introduction**

## **1.1 Measurement and Discrimination of Airborne Particulate Matter (PM)**

Airborne particulate matter (PM) typically consists of a mixture of organic and inorganic solids and liquids suspended in air, whose size varies over four orders of magnitude, from a few nanometers to tens of microns. Based on their diameter, particles are typically divided into two groups, coarse and fine, with the boundary between the two ranging from 1  $\mu\text{m}$  and 2.5  $\mu\text{m}$ . The coarse particles typically originate from the break-up of other, yet larger, solid particles, or, particles that originate from plants such as pollen and spores. Fine particles are formed from combustion, recondensed organic and metal vapors, and secondarily formed aerosols (gas-to-particle conversion). Sub-100 nm particles formed by nucleation reactions typically grow by coagulation or condensation, such that most particle diameters tend to range from 0.1 to 1  $\mu\text{m}$ <sup>1</sup>. Figure 1.1a shows a scanning electron micrograph (SEM) of environmental tobacco smoke (ETS) particulate matter (PM) deposited on an aluminum film in the Lawrence Berkeley National Laboratories (LBNL) environmental chamber; Figure 1.1b is an SEM of particulate matter collected at a distance of 100 m from a busy urban road in Castiglione Olona, Italy<sup>2</sup>.

Airborne particulate matter (PM) is a major public health issue worldwide. PM pollution is estimated to cause 20,000 to 50,000 deaths per year in the United States,<sup>3</sup> while in Europe exposure to fine PM in outdoor air leads to about 100,000 deaths (and 725,000 years of life lost) annually<sup>1</sup>. Reporting about levels of PM currently observed in Europe, the World Health Organization states:

*Long-term exposure to current ambient PM concentrations may lead to a marked reduction in life expectancy. The reduction in life expectancy is primarily due to increased cardio-pulmonary and lung cancer mortality<sup>1</sup>.*

The epidemiological mechanisms of PM exposure are not yet well understood, and the exposure of the public is not fully established. This lack of information on the health effects of airborne PM originates in part from the lack of affordable population-based exposure assessment tools. In addition to providing need localized exposure data, low-cost PM sensors would also assist in ventilation and process control and enable better indoor and outdoor air quality.

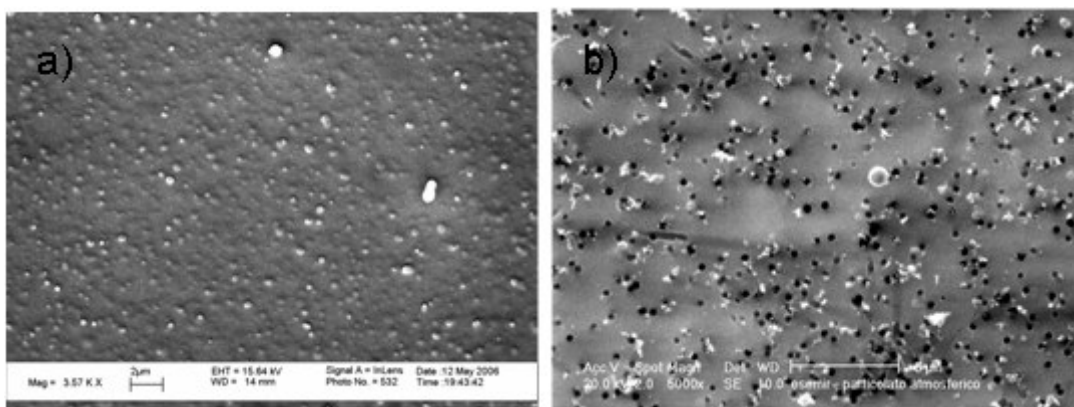


*Figure 1.1: (a) Scanning electron micrograph (SEM) of ETS particles deposited on an Al film at Lawrence Berkeley National Laboratories (LBNL); (b) SEM of ambient particulate matter collected 100 m from a busy urban road in Castiglione Olona, Italy<sup>2</sup>. The dark submicron circles are filter pores.*

There are also numerous biodefense applications of particulate matter detection. One of the most efficient methods of delivery of a biological weapon such as anthrax, plague, and smallpox is an aerosol<sup>4</sup>. Figure 1.2 shows an SEM of anthrax spores<sup>5</sup>.

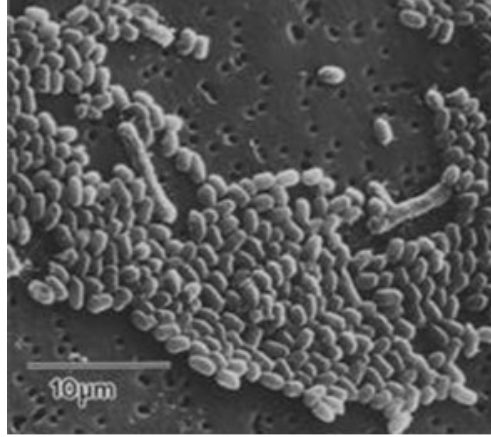


Figure 1.2: SEM of anthrax spores<sup>5</sup>.

PM measurements are typically collected with expensive and bulky instruments. Table 1.1 below compares commonly employed aerosol monitoring instruments.

Table 1.1: Comparison of PM monitoring instruments.

Type	Principle	Cost	Complexity	Volume, m <sup>3</sup>	Pro	Con
MEMS PM	Acoustic wave microbalance, optical absorbance	\$300 (est)	Low	250x10 <sup>-3</sup>	Real-time mass and PM source	Periodic module exchange
Filtration	Gravimetry, chemical and physical analysis	≤ \$1K	Labor intensive	0.4	Accurate	Integrating
Aethalometer	Filtration, optical absorbance	≤ \$20K	Low	0.3	Real-time	Limited PM source ID
TEOM	Tapered element oscillating microbalance	≤ \$20K	Low	0.4	Real-time	Non-specific
Laser Particle Counter	Light scattering and pulse counting	\$4K – 20K	Low	0.2	Real-time	Inferred mass
Dustrac	Optical particle counters	\$2K – 4K	Low	0.1	Real-time	Non-specific
QCM Impactor	Quartz crystal microbalance	≥ \$20K	Labor intensive	0.3	Real-time	Complex operation

The work of this thesis, the MEMS-based monitor for Particulate Matter (MEMS PM), is also included for comparison. It is seen the MEMS PM has

significant advantages over the other instruments with respect to size, cost, and complexity.

Other researchers have been developing low-cost particle counters to monitor indoor biomass from combustion and cooking. Using MEMS-based fabrication principles, Chua<sup>6</sup> has investigated a miniaturized corona discharge and differential mobility analyzer for PM monitoring. At Lawrence Berkeley National Laboratory (LBNL), Drs. Michael Apte and Lara Gundel<sup>7</sup> have developed the Miniaturized System for Particle Exposure Assessment (MSPEA). Designed for the detection of PM<sub>2.5</sub> (PM with a diameter smaller than 2.5  $\mu\text{m}$ ), the MSPEA uses a 10 MHz quartz crystal microbalance (QCM) for mass detection and optical probes for species discrimination.

The MEMS PM monitor of this work is based on the concepts developed in the MSPEA. The MSPEA consists of five major components<sup>8</sup>:

1. A downward pointing size-selective inlet that balances particle size-dependent gravitational settling velocities against the upward sampling velocity (here, competition between the viscous flow force (surface area) and gravity (volume) determines a cutoff particle diameter);
2. A QCM real-time mass sensor and PM deposition surface;
3. A thermophoretic (TP) collection mechanism that precipitates PM from the air onto the QCM surface where it is captured by van der Waal's forces;
4. An optical unit with a spectrophotometer to monitor the surface reflectance of ultraviolet (UV, 370 nm) and near-IR (800 nm) light; and,
5. An air pump.

The MSPEA QCM consists of a matched pair of AT-cut quartz crystals. Each QCM is configured as an oscillator, and mass loading by PM is inferred from the crystal's downward frequency shift. The TP force is generated by an electrically heated fine wire (25  $\mu\text{m}$  diameter) that consumes 90 mW. Air is sampled through a 500  $\mu\text{m}$  tall, 1 cm wide, and several cm long channel; for particle collection, the TP wire and QCM are situated at the top and bottom of the channel. Figure 1.3a shows particles, indicated by the lighter region near the middle of the crystal, thermophoretically collected on a QCM. Figure 1.3b compares the responses of the MSPEA mass and optical modules to an optical particle counter when exposed to the PM generated by a cigarette smoked every four hours in a 20  $\text{m}^3$  environmental chamber<sup>9</sup>. The QCM was shown experimentally to have a limit of detection (LOD) of 8 and 50  $\mu\text{g} / \text{m}^3$  with integration periods of six hours and one hour, respectively.

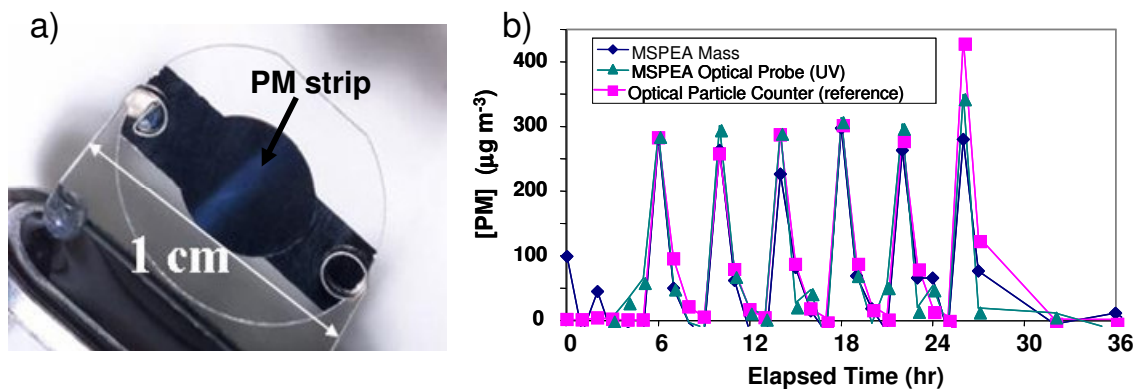


Figure 1.3: (a) ETS particles, indicated by the lighter strip in the middle of the resonator, thermophoretically precipitated onto a QCM; (b) the response of the MSPEA and an optical particle counter to the PM generated by a cigarette smoked once every four in a 20  $\text{m}^3$  environmental chamber<sup>9</sup>.

To determine the composition of the deposited mass, the MSPEA exploits differences in optical absorbance of the deposits between PM sources. As shown by



Gundel et al., diesel exhaust and black PM absorbs light in the UV and near-IR, environmental tobacco smoke (ETS) has enhanced UV absorbance with little near-IR absorbance, and woodsmoke particles have enhanced UV absorbance and significant near-IR absorbance<sup>7</sup>.

This dissertation documents the efforts to further miniaturize the MSPEA device by replacing the QCM, optical probe, and thermophoretic heater with MEMS components.

## **1.2 MEMS PM: MEMS-Based PM Detector Using Thin-Film Bulk Acoustic Wave Resonators (FBARs) and IR / UV Optical Discrimination**

This section describes the components of the MEMS-based system for Particulate Matter monitoring (MEMS PM). The MEMS PM consists of five major components:

1. A downward pointing size-selective inlet that balances particle size-dependent gravitational settling velocities against the upward sampling velocity (here, competition between the viscous flow force (surface area) and gravity (volume) determines a cutoff particle diameter);
2. A thin-film bulk acoustic wave resonator (FBAR) real-time mass sensor that serves as the PM deposition surface and a reflective surface for optical adsorption measurements;
3. A thermophoretic (TP) deposition module consisting of a polysilicon heater on a quartz substrate that precipitates PM from the air onto the FBAR surface;

4. An optical module, comprised of an array of ultraviolet (UV, 370 nm) and near-IR (800 nm) light-emitting diodes and a photodiode detector; and
5. Compact packaging that forms a flow channel driven by a low-power fan.

We will now discuss each component in detail.

## **1.2.1 Thin-Film Bulk Acoustic Wave (FBAR) Technology**

### **1.2.1.1 FBAR Resonators**

Modern embodiments of thin-film bulk acoustic wave resonators (FBAR) consist of a piezoelectric film such zinc-oxide (ZnO), aluminum nitride (AlN), or lead-zirconium titanate (PZT), sandwiched between metal electrodes, that resonates, nominally, in a thickness extensional (TE) mode. The piezoelectric film, with typical thicknesses of 1 to 6  $\mu\text{m}$  and a resonant frequency of a few hundred MHz to several GHz, functions both as the transducer and sustaining medium of the resonator. In the fundamental mode of resonance, the piezoelectric film thickness corresponds to one-half of an acoustic wavelength (if one ignores the influence of the electrodes, Chapter 2 of this dissertation analyzes the influence of the electrodes on the resonator).

Depending on the manner in which energy is confined in the piezoelectric medium, FBARs typically take one of the three forms shown in cross-sections in Figure 1.4: surface-mounted resonator (SMR), composite resonator, or edge-supported resonator.

The SMR, Figure 1.4a, is acoustically isolated from the substrate with a reflector composed of alternating high and low acoustic impedance quarter-

wavelength-thick layers. The composite resonator, Figure 1.4b, is supported by a thin membrane and is acoustically isolated by removing the underlying substrate (either by removal of the underlying bulk silicon or by use of a surface micromachined sacrificial layer). The edge-supported FBAR, Figure 1.4c, consists of a freestanding metal-piezoelectric-metal stack connected to the substrate by metal / piezoelectric tethers, with the underlying substrate removed by a surface micromachined etch.

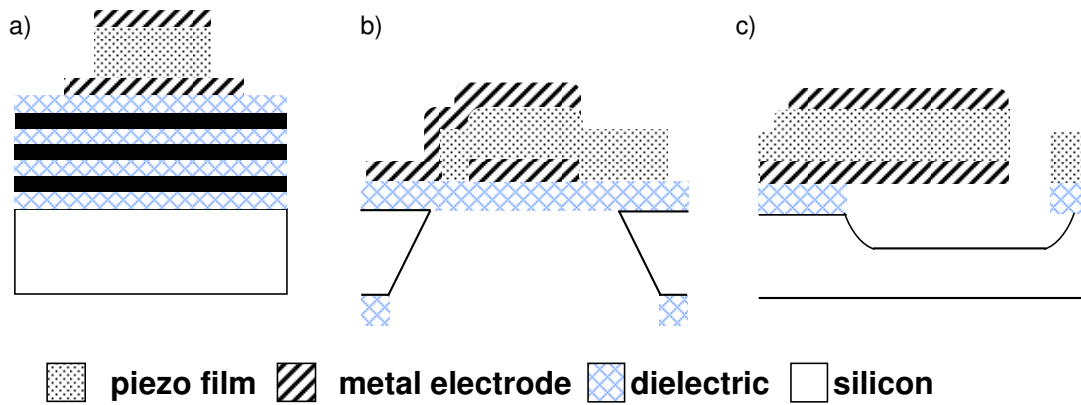


*Figure 1.4: Cross-sections of the three types of thin-film bulk acoustic wave resonators, distinguished by the manner in which energy is confined in the piezoelectric medium: (a) solidly-mounted resonator (SMR); (b) composite resonator; and (c) edge-supported resonator.*

FBARs originated from bulk acoustic wave (BAW) quartz resonator technology developed for low-phase-noise oscillators and filters<sup>10,11</sup>. Operating in a thickness shear or thickness extensional mode, where the frequency of operation is determined by the quartz thickness, the fundamental resonance of quartz BAW crystals is typically limited to frequencies in the tens of MHz range. The scope of the commercial quartz BAW applications is impressive – in 2005 about 5.2 billion MHz quartz crystal resonators were shipped worldwide with an average selling

price (ASP) of 16.9¢, representing about \$900 million in revenue<sup>12</sup>. GSM and CDMA cellular handsets, for example, use high-performance 13 or 26 MHz and 19.2 MHz crystals, respectively, that exhibit + / - 10 ppm stability over a range of demanding operating conditions.

Researchers have made UHF quartz BAW resonators by thinning the quartz with an ion mill or other etching techniques<sup>13,14,15,16</sup>. However, such devices are not mechanically robust and the machining techniques have yet to be scaled economically to commercial devices.

In the late 1960s, Silker and Roberts<sup>17</sup> first demonstrated a 297 MHz composite resonator composed of a thin film cadmium sulfide (CdS) transducer evaporated onto a bulk quartz substrate. A year later, Page<sup>18</sup> replaced the quartz with a 3-mil thick silicon substrate. In the late 1970s and early 1980s, high-overtone bulk acoustic wave resonators (HBARs) appeared for use as the feedback elements in ultra-low-noise microwave oscillators<sup>19,20</sup>. In an HBAR, a thin-film ZnO or AlN transducer is deposited onto the surface of a highly polished crystal that has low acoustic loss. The virtue of this configuration is that the resonant crystal itself need not be piezoelectric, which has opened the way for the use of materials that have an order of magnitude lower acoustic loss than quartz (and two orders of magnitude lower than silicon). With the use of crystal media such as sapphire, lithium niobate, lithium tantalite, spinel, and yttrium-aluminum-garnet (YAG), researchers have achieved Q-frequency products approaching  $10^{14}$  Hz, and the best of non-superconducting Q in any VHF resonator<sup>21</sup>.

In 1980, with the emergence of silicon micromachining techniques<sup>22</sup>, the modern composite FBAR was first fabricated by Lakin and Wang<sup>23</sup> and Grudkowski et al.<sup>24</sup>. Here, composite FBARs, made from ZnO films sputtered onto bulk-etched, p+-doped Si membranes, exhibited fundamental frequencies approaching 500 MHz and series- resonance quality factors of 3000. Because of the high-quality factors and small form factors of these devices, considerable attention was subsequently directed towards their development. Researchers demonstrated temperature-compensated AlN thickness extensional<sup>25</sup> and thickness-shear<sup>16</sup> composite resonators, filters<sup>26</sup>, GHz AlN resonators on gallium arsenide<sup>27</sup>, and monolithic integration of filters on SiO<sub>2</sub> membranes with passive components<sup>28,29</sup>. The edge-supported FBAR<sup>30</sup> and the solidly mounted resonator<sup>31</sup> were first reported in 1982 and 1995, respectively.

Figure 1.5a shows an SEM of a typical edge-supported AlN FBAR employed in the MEMS PM. The resonator consists of a Pt bottom electrode and Al top electrode, and is isolated acoustically by the removal of the underlying silicon. As shown in Figure 1.5b, the MEMS PM incorporates four FBAR sensors to extend the life of the instrument – when particles overload the sensor, one can simply move on to the next unsullied FBAR. AlN FBARs with fundamental frequencies around 1.6 GHz, quality factors over 2000, and motional resistances less than 2  $\Omega$  were developed in BSAC for the MEMS PM.

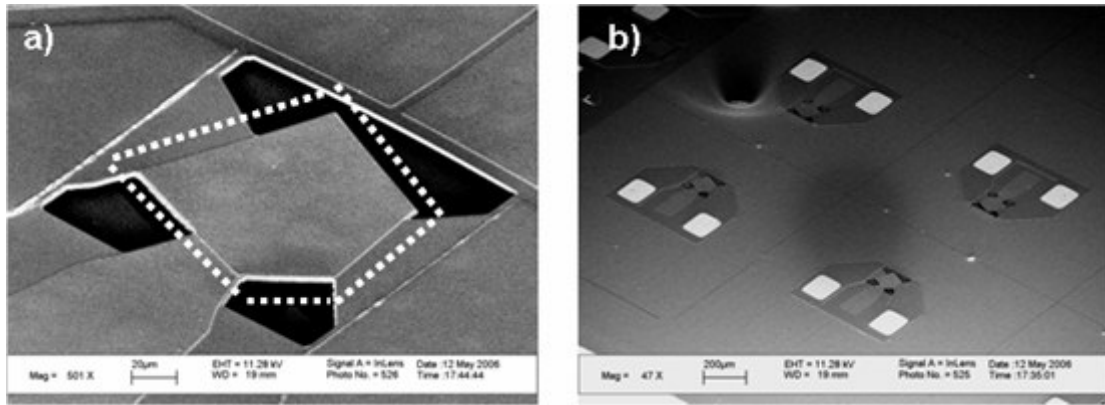


*Figure 1.5: (a) SEM of a typical AlN FBAR employed in the MEMS PM (the active FBAR area is outlined by the dotted white line); (b) as implemented, the MEMS PM consists of an array of four FBAR mass sensors.*

### 1.2.1.2 FBAR Filters

The suitability of FBARs for miniaturized RF filtering became apparent early on<sup>32</sup>. However, it wasn't until the manufacturing innovations pioneered by Agilent Technologies in the late 1990's that the FBAR technology became cost-competitive with RF surface acoustic wave (SAW) filter technology<sup>33,34,35</sup>. The primary manufacturing obstacles were wafer-level packaging and the ability to deposit AlN and metal electrodes with  $\pm 500$  ppm (0.1%) uniformity across 6" and 8" substrates<sup>36,37</sup>. Within the semiconductor industry, film uniformity tolerances are typically a few percent. TFR Technologies Inc. (acquired by Triquint) also sold low volumes of AlN SMR filters to the U.S. military<sup>38</sup>.

Today, cellular handset FBAR RF filter and duplexer products are shipped by Agilent Technologies (edge supported) and Infineon Technologies (SMR)<sup>39,40</sup>, but FBAR technology in general continues to be plagued by yield issues related to film uniformity. Recently emerged contour-mode AlN piezoelectric<sup>41</sup> and electrostatic<sup>42</sup> technologies promise to address the FBAR manufacturing issues.

While FBAR technology has significant performance advantages over SAW in both the cell (800-900 MHz) and Personal Communications Service(PCS, 1800-1900 MHz) bands, as of the year 2006 only FBAR duplexers for the CDMA PCS bands are cost competitive, and even there the advantage is tenuous. By 2003, Agilent had 60 design wins in CDMA handsets and was shipping millions of duplexers per month<sup>43</sup>. Worldwide, in 2005, Agilent shipped about 52 million PCS band duplexers with an ASP of \$2.27 per duplexer. In comparison, 155 million SAW duplexers and 37 million ceramic duplexer were shipped at an ASP of \$1.80 and \$1.16 per duplexer, respectively<sup>44</sup>. This represents a fairly modest inroads given that the market for cellular RF SAW filters in 2005 amounted to around 2 billion units worth close to 1\$ billion in revenue. The scale of the commercial market for FBARs suggests that they could be manufactured for MEMS PM purposes for around 0.20\$ each<sup>45</sup>.

#### **1.2.1.3 FBAR Oscillators**

FBARs have also found extensive application as the feedback, frequency determining element of high-performance oscillators. FBAR-based oscillators reported in the literature are summarized in Table 1.2 (phase noise denotes the single-side band noise in a 1 Hz bandwidth at the stated offset frequency). No discussion of the long-term stability of the oscillators, a key concern in the operation of MEMS PM, was found in the literature.

The MEMS PM incorporates a four-element Pierce FBAR oscillator array designed in a 0.25  $\mu\text{m}$  CMOS technology. Figure 1.6 shows the oscillator topology and the oscillator spectra.

Table 1.2: FBAR-based oscillators in the literature.

FBAR Description	Oscillator Topology	Phase Noise [dBc / Hz at (offset)]	Frequency [MHz]	Output Power [dBm]	Temperature Coefficient of Frequency [ppm / °C]	Ref.
Composite–ZnO on p+ Si membrane	BJT Pierce	-112 (1 kHz)	262	-22	not stated	46
Composite–AlN on p+ Si membrane	BJT Pierce	-110 (1 kHz)	335	not stated	-8	47
Composite–SiO <sub>2</sub> / ZnO / Au electrode membrane	Colpitts with monolithically integrated BJTs	-90 (20 kHz)	423	-19.4	-5	48
Composite–ZnO on p+ Si membrane	Pierce with monolithic BJTs	-90 (1 kHz)	257	3	-8.5	49
Two-pole monolithic ZnO crystal filter	Pierce with BJTs	-90 (1 kHz)	1185	not stated	not stated	50
Edge supported AlN double-stacked crystal filter	VCO and Pierce with monolithic BJTs	-72 (1kHz)	1043	not stated	not stated	51,52
Edge supported AlN with Mo electrodes	Pierce in 0.18 $\mu$ m CMOS	-100 (10 kHz)	1900	6	-25	53
Edge supported AlN with Pt / Al electrodes	Pierce in 0.25 $\mu$ m CMOS	-102 (10 kHz)	1600	-5	-25	this work

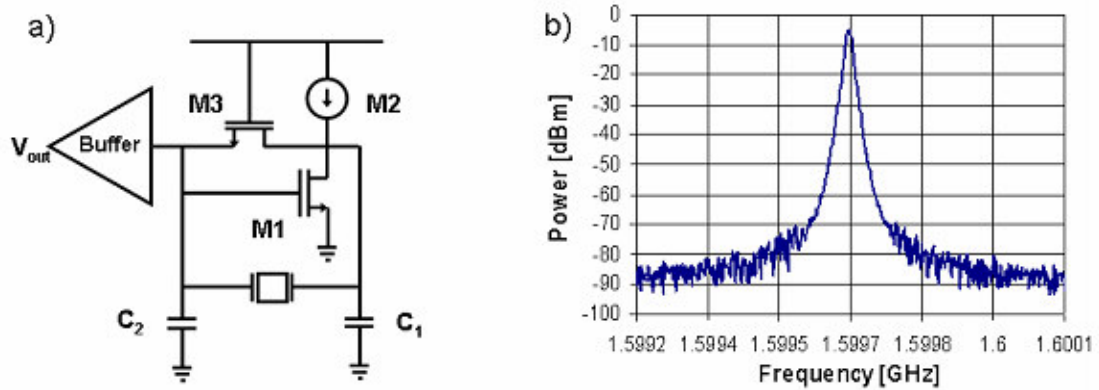


Figure 1.6: (a) Pierce oscillator employing FBAR resonator as feedback element; (b) output spectrum of 1.6 GHz FBAR-based oscillator.



#### 1.2.1.4 FBAR Acoustic-Wave Sensors

Acoustic wave devices have been used for the detection of a wide variety of measurands. In most acoustic sensors, a piezoelectric crystal or thin film serves both as the propagation medium and the transducer for wave excitation. Detection may be achieved by monitoring the velocity shift or attenuation of acoustic waves due to a change in an electromechanical property of the path of propagation. The most straightforward technique is to employ a network analyzer (NA) to measure the resonator impedance. Since NAs are bulky and expensive, for low-cost portable applications, the use of an oscillator and frequency counter is more practical. With the resonator configured as the feedback element of an electrical oscillator, measurands can be readily detected as a shift in resonant frequency or electrical amplitude. The advantages of acoustic-wave devices for mass sensing include:

- cost, as low as a few dollars per device
- size, as small as a few hundred microns on a side
- robust and simple principle of operation
- the technology is ubiquitous in electronic and communication systems

Figure 1.7 shows schematics of the cross-sectional mode shapes of several common acoustic sensors. The quartz crystal microbalance (QCM) is a piece of AT-cut quartz operating in its thickness-shear mode (TSM). QCMs have found extensive use in chemistry to monitor surface reactions, detect vapors, and measure the viscosities of fluids. In the surface acoustic wave (SAW) device, Rayleigh waves propagate on the surface of a bulk piezoelectric crystal such as quartz or lithium niobate. The amplitude of motion decays exponentially away from the

crystal surface, and the motion persists to a depth of approximately one acoustic wavelength. As the frequency of excitation increases, the acoustic energy becomes more closely confined to the crystal surface, increasing the sensitivity to mass loading. In the flexural plate wave (FPW) device, zeroth order anti-symmetric Lamb waves propagate in a plate with a thickness,  $d$ , much smaller than the acoustic wavelength,  $\lambda$  ( $d / \lambda \ll 1$ ). The entire plate undergoes mechanical deformation and the wave velocity, usually a few hundred meters per second, decreases as the plate thickness decreases. In the thin-film bulk acoustic wave resonator (FBAR), the crystal resonates in its fundamental thickness extensional mode, the thickness oscillating between dilation and contraction. Other sensors not included in the Figure include shear-horizontal acoustic plate mode devices (SH-APM) and shear-horizontal SAW devices (SH-SAW).

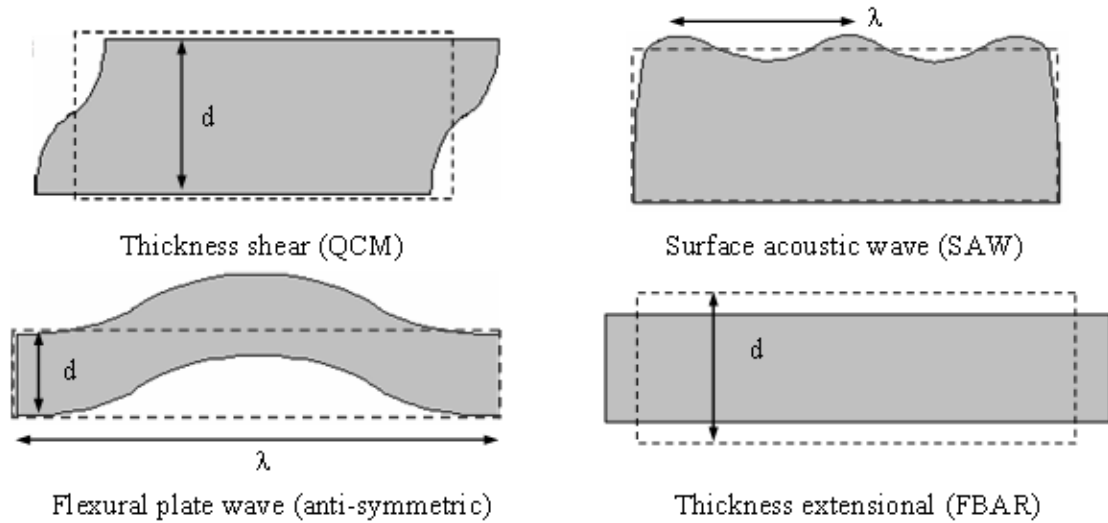


*Figure 1.7: Mode shapes of common acoustic-wave devices.*

The behavior of acoustic wave devices subjected to mass loading is governed by the Sauerbrey equation<sup>54</sup>:

$$\frac{\Delta f}{f} = \frac{\Delta m'}{m'} = S_m \Delta m' \quad \text{Eq. 1.1}$$

where:

$f$	=	resonant frequency of the crystal [Hz];
$\Delta f$	=	change in frequency due to the added mass [Hz];
$m'$	=	mass per unit area of the crystal [gm / cm <sup>2</sup> ];
$\Delta m'$	=	added mass per unit area [gm / cm <sup>2</sup> ];
$S_m$	=	mass sensitivity [gm / cm <sup>2</sup> ].

Table 1.3 compares the mass sensitivity and frequency of operation of the QCM, SAW, FPW, and FBAR.

The use of resonating piezoelectric crystals for sensing is well established. TSM resonators were first employed for use in monitoring the deposition of metals in vacuum systems<sup>54</sup>. In 1964, King<sup>55</sup> first employed AT-cut, TSM quartz resonators to sense polar vapor molecules. Subsequently, QCMs have been employed in a vast number of analytical areas such chemical vapor detection, immunosensing, fluid characterization, DNA biosensing, and drug analysis<sup>56,57,58,59</sup>.

*Table 1.3: Mass sensitivity of common acoustic-wave devices.*

Sensor type	Theoretical Mass Sensitivity, $S_m$ [cm <sup>2</sup> / g]	Device Description	Typical Operating Frequency [MHz]	Typical Mass Sensitivity, $S_m$ [cm <sup>2</sup> / g]
Thickness shear mode (QCM)	1 / $\rho d$	AT-cut quartz, metal electrodes	6	14
Surface acoustic wave (SAW)	$K(\nu)/\rho\lambda^\dagger$	ST-cut quartz, metal electrodes	100-500	130 (100 MHz)
Flexural plate wave (FPW)	1 / $2\rho d$	ZnO, SiN, Al electrodes	1-30	450
Thin-film bulk acoustic wave resonator (FBAR)	1 / $\rho d$	ZnO or AlN, Au, Pt, or Mo electrodes	1000-2000	750

<sup>†</sup> here  $\rho$  is the material density,  $\nu$  is Poisson's ratio, and  $K(\nu)$  ranges from 1 to 2 for most solids.

SAW sensors were first employed as pressure sensors<sup>60</sup> and as the chemical vapor detector in a gas chromatograph<sup>61</sup>. Subsequently, SAW sensors have found

use in a wide range of commercial and research applications, such as commercially available gas chromatographs (GCs)<sup>62,63,64</sup>, automotive tire pressure monitoring<sup>65</sup>, humidity sensing<sup>66</sup>, and inertial sensing<sup>67</sup>.

The FPW device has been shown to function well as a sensor in both the liquid and vapor phases. Researchers have examined the sensitivity of the FPW device to chemical vapors<sup>68,69,70,71</sup>. Wang et al. used the FPW device to measure the diffusion of solutes in gels<sup>72</sup> and for the detection of breast cancer antigens<sup>73</sup>, and Martin<sup>74</sup> demonstrated the liquid viscosity and density sensing properties of the FPW device.

As a sensor, the FBAR was first employed for methanol vapor detection and monitoring the adsorption of poly(methyl methacrylate)<sup>75,76</sup>. Taking impedance measurements of an edge-supported AlN GHz FBAR with a network analyzer, the authors investigated the response of thiolate-coated FBARs to methanol vapors. An SMR vapor sensor has also been patented<sup>77</sup>.

More recently, a renewed interest in sensing with FBARs has emerged. Zhang et al. have employed ZnO composite FBARs to monitor ethanol vapors<sup>78</sup>, characterized the operation of the resonator in a fluid medium, and detected mass loading of metal ions onto a Ti layer added to the FBAR membrane.<sup>79,80,81</sup> Liquid loading was found to reduce the quality factor of the FBAR by more than an order of magnitude. Gabl et al. used a 2 GHz ZnO SMR to monitor biotin-streptavidin conjugation (measurements taken after dessication), and added a polyimide film for detection of CO<sub>2</sub> and condensed water vapors<sup>82,83</sup>. In all of these publications, no oscillator-based measurements were reported, rather, FBAR impedance

measurements were taken with an NA. Bredelow et al.<sup>84</sup>, however, describe the use of both an NA and an oscillator to characterize the response of a silane-coated 2 GHz AlN SMR to loading with water and bovine-serum albumin.

Researchers have previously employed acoustic-wave devices for aerosol detection. In 1970, Chuan developed a QCM-based aerosol mass detection instrument with a reported resolution of 50 pg<sup>85</sup>. In the device, aerosol particles were directed toward and impacted upon a 10 MHz QCM coated with an adhesive layer. Subsequently, Bowers and Chuan demonstrated a 158 MHz SAW delay-line oscillator<sup>86</sup> and a 200 MHz SAW MHz resonator oscillator<sup>87</sup> for aerosol detection, with a reported mass resolution in the low picogram range. The 200 MHz SAW resonator sensor was found to be two orders of magnitude more sensitive than Chuan's 10 MHz QCM, and, with a higher Q, showed an order of magnitude greater frequency stability than the sensor based on the SAW delay line.

Commercial QCM-based aerosol monitors sold by Thermo-Systems Inc. (St. Paul, MN) were studied extensively in the 1970s and 1980s<sup>88,89,90,91,92</sup>. The instruments incorporated 5 MHz AT-cut quartz crystals, a series of impactors to remove large particles (for example, with a 5  $\mu\text{m}$  cutoff) from the sample stream, an electrostatic PM precipitator, and a microcomputer for automated operation. The reported mass-sensing resolution was 0.0056  $\mu\text{g} / \text{m}^3$  and, in side-by-side comparisons with filter measurements, the instruments functioned well for the detection of a wide range of particle types except dry carbon black, diesel exhaust, and large cenospheres (a cenosphere is a lightweight, inert, hollow sphere filled with

inert air or gas, which are mainly produced from the combustion of coal in power plants).

To the author's knowledge, our present work constitutes the first use of an FBAR oscillator as a real-time mass monitor, and the first application of FBARs for aerosol detection.

### 1.2.2 Thermophoretic Deposition

In 1870, J. Tyndall observed that in a dust-laden chamber, particle-free regions formed around a hot metal ball or a heated platinum wire. This phenomenon, subsequently studied by Rayleigh and others, was correctly explained in 1884 by Aitken who concluded that the particles were driven away from the heated surface by collisions with gas molecules of differing kinetic energies<sup>93</sup>. As Figure 1.8 illustrates, in the presence of a temperature gradient,  $\nabla T$ , gas molecules collide with particle and generate a thermophoretic force,  $F_T$ .

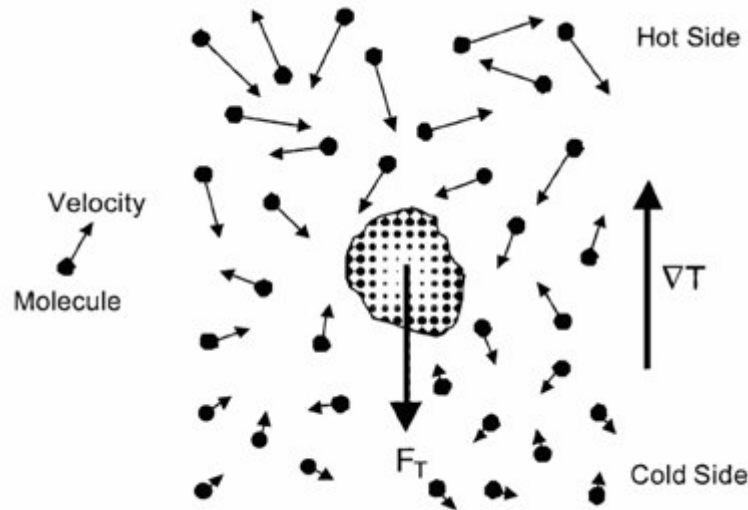


*Figure 1.8: Origin of the thermophoretic force: in the presence of a temperature gradient  $\nabla T$ , a thermophoretic force,  $F_T$ , is generated by the net momentum imparted*

*from collisions with air molecules [after <sup>93</sup>]. Since molecules closer to the “Hot side” possess greater kinetic energy than those near the “Cold side”, the particle experiences a net force in a direction opposite to that of the temperature gradient.*

The physics of thermophoresis depend on the Knudsen number,  $Kn$ , defined as the ratio of the gas mean free path,  $L$ , to the radius of the particle,  $a$ :

$$Kn = \frac{L}{a} \quad \text{Eq. 1.2}$$

For  $Kn \rightarrow \infty$ , known as the “free-molecule regime”, the velocity distribution of the gas molecules is not significantly disturbed by the particle, and the particle dynamics can be modeled as a large gas molecule. For  $Kn \rightarrow 0$ , known as the “near-continuum regime”, the gas can be modeled as a continuum using the Navier-Stokes equations with the appropriate slip boundary conditions. The boundary conditions model the particle-air molecule interaction within a few mean free paths of the particle surface. Brock derived a near-continuum solution for the thermophoretic force as<sup>94</sup>:

$$f_T = \frac{24\pi}{5} \frac{C_{tc} Kn (\kappa_{21} + C_t Kn)}{(1 + 3C_m Kn)(1 + 2\kappa_{21} + 2C_t Kn)} \quad \text{Eq. 1.3}$$

where:

$$\begin{aligned} \kappa_{21} &= \text{thermal conductivity of the gas to that of the particle;} \\ C_m, C_{tc}, C_t &= \text{boundary conditions, derived from kinetic gas theory.} \end{aligned}$$

With a typical particle diameter of 1  $\mu\text{m}$  and a mean free path for air molecules of approximately 80 nm, the MEMS PM principally operates in this near-continuum regime (this dissertation does not further explore the physics of thermophoresis).

The use of thermal precipitators for the collection of aerosol and airborne bacteria has been previously demonstrated<sup>95,96,97</sup>. Researchers have demonstrated collection efficiencies approaching 100%, where particles directed toward the substrate surface attach by van der Waal's forces. The thermophoretic heater in the MEMS PM, shown in the SEM of Figure 1.9a, consists of a released polysilicon serpentine structure affixed to an optically transparent fused quartz substrate. As shown in the SEM of Figure 1.9b, the MEMS PM incorporates an array of four addressable heaters that are aligned to a four-element FBAR array.

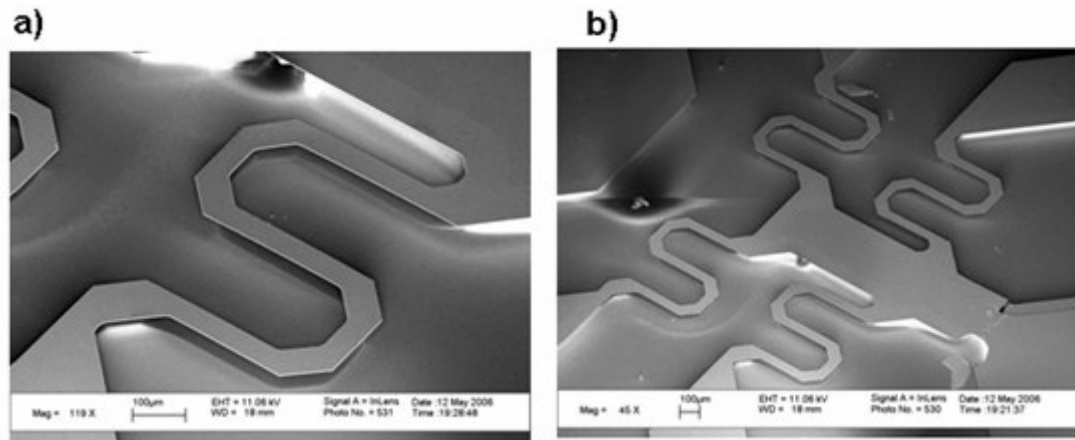


*Figure 1.9: (a) SEM of polysilicon serpentine heater released from an optically transparent quartz substrate; (b) the MEMS PM consists of an array of four addressable heaters which align to the four-element FBAR array (Figure 1.5).*

### **1.2.3 Optical Discrimination of PM Composition**

Common airborne particulates absorb near-infrared and ultraviolet light (UV) differently. For example, Gundel and Apte first demonstrated that environmental tobacco smoke (ETS) particles adsorb in the UV<sup>7</sup>. Figure 1.10 compares the absorbance of common types of particulate matter<sup>8</sup>. The differential adsorption characteristics of the airborne sources shown allow one to estimate the composition of deposited PM.



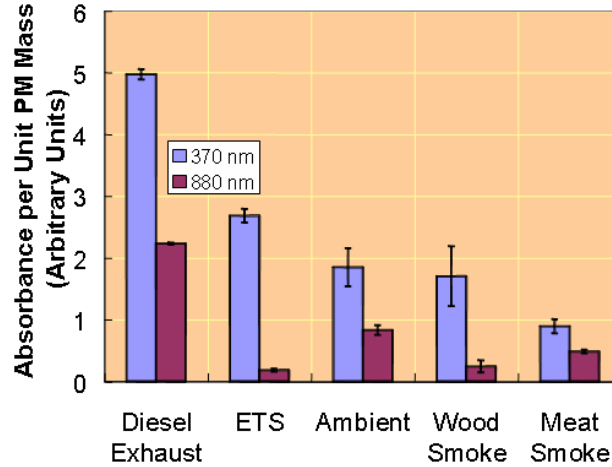


*Figure 1.10: Comparison of absorbance in the near-UV and near-IR for combustion sources that generate airborne PM (after<sup>8</sup>).*

A number of different MEMS PM optical module configurations were investigated during the project. In the final design, shown in Figure 1.11a, light from UV and IR LEDs is transmitted through an aperture in an aluminum housing to a photodetector. ETS PM thermophoretically deposited onto a quartz slide covering the aperture reduces the amount of light transmitted. Figure 1.11c and Figure 1.11d compare the UV and IR transmission characteristics before and after thermophoretic deposition of ETS. In the experiment, the transmitted light intensity was measured with an Ocean Optics (Dunedin, FL) spectrophotometer. The fractional change in transmission intensity at 375 nm is twice that at 810 nm (the final design was not integrated into the MEMS PM due to time constraints).

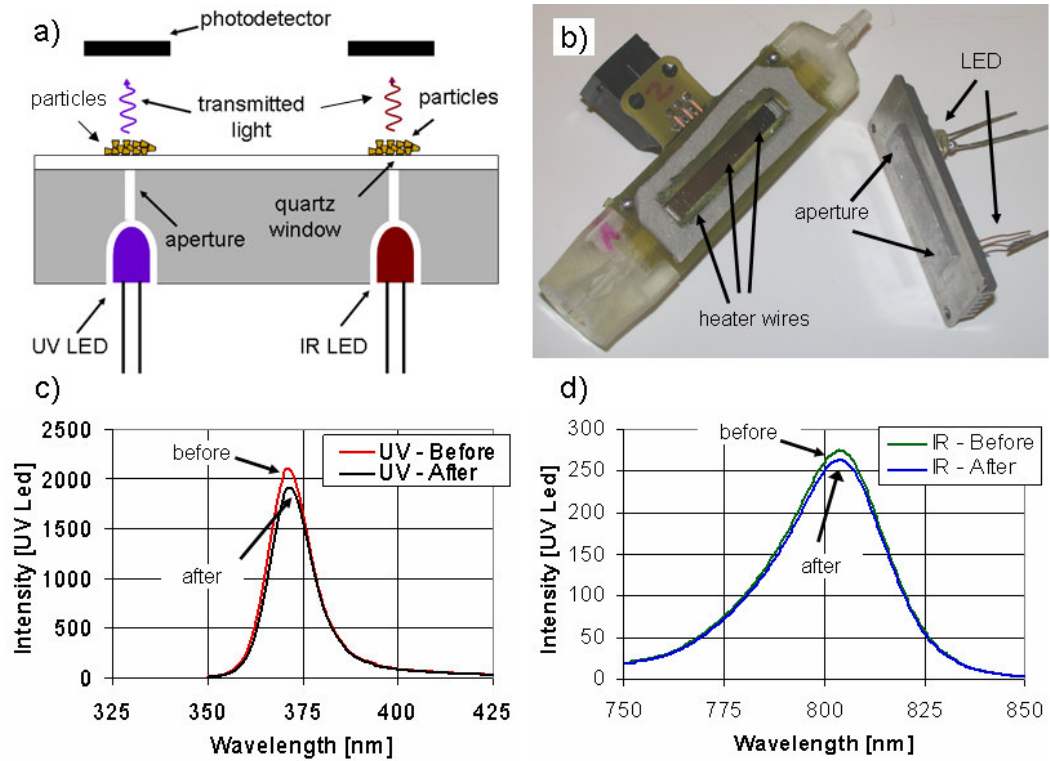


Figure 1.11: (a) Cross-sectional schematic of optical module with IR / UV LEDs and two apertures in an aluminum housing; (b) photograph of the final transmission-based optical module; (c), (d) UV and IR transmission characteristics of ETS PM showing differential absorption.

#### 1.2.4 Packaging

The compact integration and accurate alignment of the MEMS PM modules required a number of package design iterations. Figure 1.12a is a SolidWorks schematic of the final package (schematic created by Dr. Rossana Cambie) consisting of the optical module, thermophoretic precipitator, FBAR / CMOS mass sensor, and flow channel and fluidic interconnects. The optical module design shown in Figure 1.12a was a preliminary design that suffered from scattering problems and was discarded in favor of that of Figure 1.11.

Figure 1.12b contains a photograph of an assembled FBAR mass sensor module (without the optics module). The 2 mm wide, 500  $\mu\text{m}$  tall flow channel is

defined by a machined brass housing, channel sidewall spacers, an aperture, and a CMOS / FBAR spacer, all secured to the FBAR PCB with twelve screws. The spacers provide clearance for the CMOS and FBAR bondwires and define the distance between thermophoretic heaters and the FBAR surface. In order to prevent air leaks, a bead of silicone is added along the outside edges of the interface between parts after the module is bolted together.

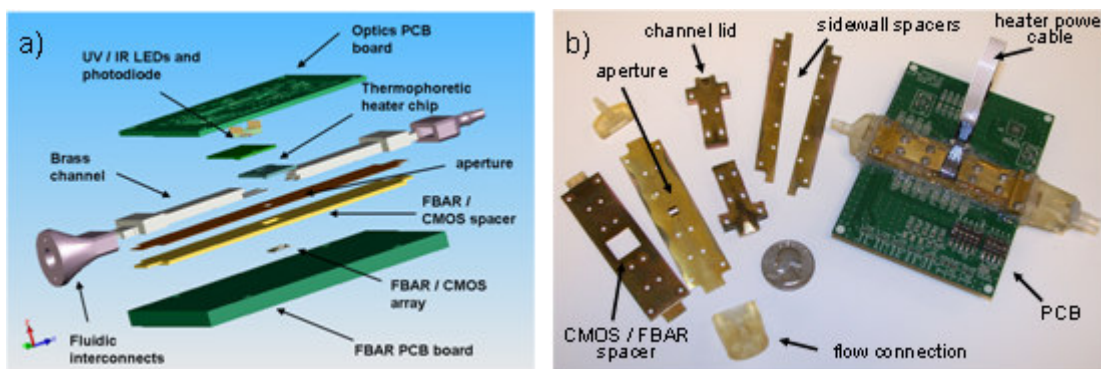


Figure 1.12: (a) Exploded SolidWorks view of the MEMS PM package; (b) photograph of the assembly and the individual parts.

### 1.3 Aerosol Monitoring Experiments

The initial testing and characterization of the MEMS PM took place in an environmental chamber at Lawrence Berkeley National Laboratories (LNBL); later the monitor was tested in a Berkeley, CA dwelling. The chamber, shown in Figure 1.13a, was outfitted with an automated cigarette smoking machine that generated ETS particles. The room was also retrofitted to inject the exhaust from a diesel generator located next to the building. During experiments, one or a combination of commercial instruments measured particle concentration; these included a Quartz Crystal Microbalance (QCM) Cascade Impactor, an Optical Particle Counter, and an Aethelometer.

Figure 1.13b compares the responses of the MEMS PM and the commercial QCM impactor when one cigarette is smoked in the chamber; good agreement between the two sensors is evident. In the Figure, the negative of the derivative of the FBAR frequency is plotted as a function of time (the right y-axis is the QCM sensor reading).

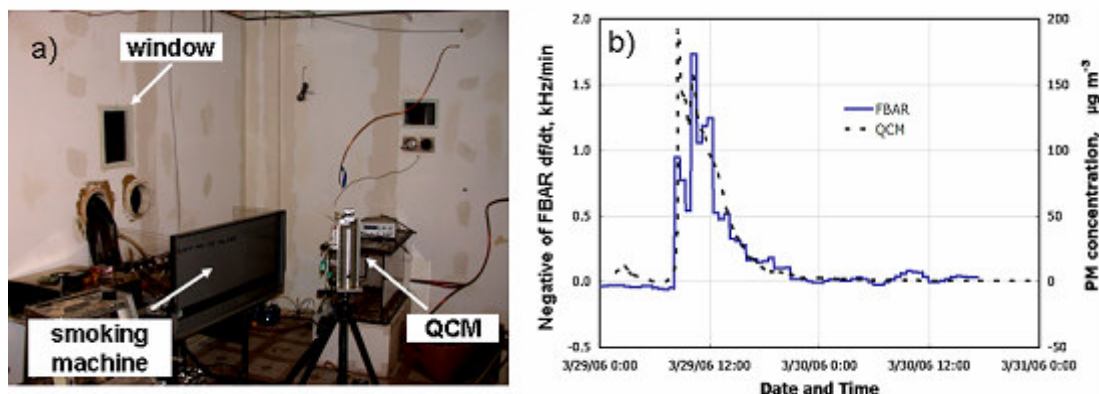


Figure 1.13: (a) Photograph of the LBNL environmental chamber; (b) responses of the MEMS PM and the commercial QCM impactor when one cigarette is smoked in the environmental chamber (the right y-axis is the QCM sensor reading).

These environmental chamber experiments demonstrated that the MEMS PM satisfies the EPA Federal Reference Method (FRM) for aerosol detection. This key benchmark – a requirement for any commercial aerosol monitor – mandates a minimum detection limit of a  $30 \mu\text{g} / \text{m}^3$  aerosol concentration measured over a 24-hour period.

The MEMS PM was evaluated in a field study in a Berkeley residence (the optical module was not evaluated in the field). Figure 1.14a is a photograph of the experimental setup. A number of common residential sources of particulate matter were used including burnt toast, burnt eggplant, diesel combustion, wood smoke

from a fireplace, cigarette smoke, and ambient particulate matter. Particle concentrations were corroborated with several commercial instruments – a QCM impactor, an Aethalometer, an optical particle counter (OPC), a high-flow sampler for measuring episodic source-enriched  $PM_{2.5}$ , and a Federal Reference Method (FRM) sampler for  $PM_{2.5}$ . As shown in Figure 1.14b, there was good agreement between the MEMS PM and FRM sampler measurements.

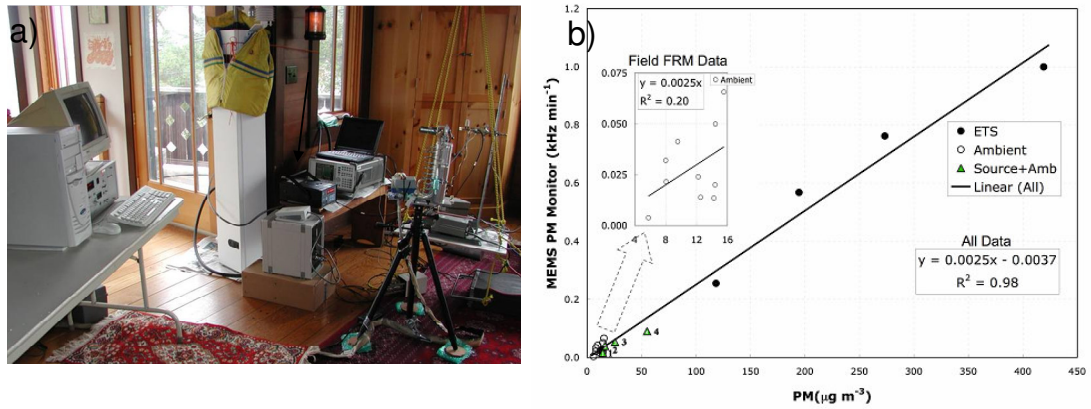


Figure 1.14: (a) Equipment setup for field test in a Berkeley, CA dwelling including quartz crystal microbalance (QCM), Aethalometer, optical particle counter (OPC), high-flow sampler for measuring episodic source-enriched  $PM_{2.5}$ , FRM sampler for  $PM_{2.5}$ , and the MEMS particulate matter monitor (MEMS PM); (b) summary test results showing good agreement between the MEMS PM and the FRM sampler for  $PM_{2.5}$ .

## 1.4 Outline of Subsequent Chapters

Chapter 2 of this dissertation describes the underlying physics governing the FBAR mass sensor and the design of the sensor interface circuitry. The FBAR electromechanical governing equations are analyzed in order to characterize its response to particulate matter and to derive equivalent circuits used in the design of CMOS oscillator sustaining circuitry.

Chapter 3 documents the fabrication and characterization of ZnO and AlN FBARs and the thermophoretic heater. The chapter also discusses:

- Resonator electrical characterization;
- ZnO FBAR mass loading with Al films to characterize the mass sensitivity;
- ZnO FBAR imaging with an optical interferometer; and,
- AlN FBAR imaging with a novel tapping-mode atomic force microscope (AFM) technique.

Chapter 4 reports the results of MEMS PM monitoring experiments. The optical module was calibrated separately and was not used in the MEMS PM. The key experiments reported in this chapter are:

- ETS detection with an early FBAR mass sensor prototype;
- MEMS PM calibration with ETS in the LBNL environmental chamber;
- optical module characterization;
- discrimination of PM composition by thermal spectroscopy;
- MEMS PM response to fresh diesel exhaust; and,
- field study in Berkeley residence.

Chapter 5 summarizes the dissertation and suggests directions for future work.

## **1.5 Chapter 1 References**

---

<sup>1</sup> “Health aspects of air with particulate matter, ozone, and nitrogen dioxide”, Report on World Health Organization Working Group, Bonn, Germany, January, 2003.

- 
- <sup>2</sup> “ESEMIR, Particulate Matter in Air”, August, 2006, [http://www.esemir.it/partic\\_i.htm](http://www.esemir.it/partic_i.htm).
- <sup>3</sup> A.H. Mokdad, et al., "Actual causes of death in the United States, 2000", *J. Amer. Medical Assoc.*, vol. 291, no. 10, pp. 1238-1235, 2005.
- <sup>4</sup> W.D. Burrows and S.E. Renner, “Biological warfare agents as threats to potable water”, *Environmental Health Perspectives*, vol. 107, no. 12, pp. 975-84, 1999.
- <sup>5</sup> “Anthrax”, August, 2006, <http://fig.cox.miami.edu/~cmallery/150/anthrax/anthrax.htm>.
- <sup>6</sup> B. Chua and N.C. Tien, “Corona MEMS for wide study area air particulate monitoring”, Fall 2005 Industrial Advisory Board Semi-Annual Research Report, Berkeley Sensor & Actuator Center, University of California at Berkeley, Berkeley, CA, 2005.
- <sup>7</sup> L.A. Gundel, M.G. Apte, A.D. Hansen, and D.R. Black, “Apparatus for particulate matter analysis”, US Patent Application 20040259267, December 23, 2004.
- <sup>8</sup> R.M. White, M.G. Apte, L.A. Gundel, and M.J. Vestel, “Development of a low-cost particulate matter monitor”, *Proposal* Submitted to the Innovative Clean Air Technologies 2003 Grant Program, California Air Resources Board, December, 2002.
- <sup>9</sup> R.M. White and M.G. Apte, “Development of a low-cost particulate matter monitor”, Presentation to the Innovative Clean Air Technologies Grant Program, California Air Resources Board, July, 2003.
- <sup>10</sup> E.A. Gerber, T. Lukaszek, and A. Ballato, “Advances in microwave acoustic frequency sources”, *IEEE Trans. Microwave Theory and Techniques*, vol. 34, no. 10, pp. 1002-1016, 1986.
- <sup>11</sup> A. Ballato and T. Lukaszek, “Stack-crystal filters”, *IEEE Proc.*, pp. 1495-1496, 1973.
- <sup>12</sup> “Crystal and Oscillator Market Research H1 2005”, Market Research Report, Frequency Control Insights, 2005.
- <sup>13</sup> G.K. Guttwein, A.D. Ballato, and T.J. Lukaszek, “VHF-UHF piezoelectric resonators”, *US Patent* 3,694,677, September 26, 1972.

- 
- <sup>14</sup> M. Berte and P. Hartemann, "Quartz resonators at fundamental frequencies greater than 100 MHz", *Proc. IEEE Ultrasonics Symp.*, 125 pp. 148-151, 1978.
- <sup>15</sup> J.P. Aubry, "Quartz and LiTaO<sub>3</sub> VHF resonators for direct frequency generation in the GHz range", *Proc. IEEE Ultrasonics Symp.*, pp. 487 – 490, 1983.
- <sup>16</sup> J.S. Wang, A. Kong, K.F. Lau, and K.H. Yen, "Recent developments on membrane bulk-acoustic-wave resonators", *Proc. IEEE Freq. Control Symp.*, pp. 356-360, 1985.
- <sup>17</sup> T.R. Silker and D.A. Roberts, "A thin-film CdS-quartz composite resonator", *J. App. Phys.*, vol. 38, no. 5, pp. 2350-2358, 1967.
- <sup>18</sup> D.J. Page, "A cadmium sulfide-silicon composite resonator", *IEEE Proc.*, vol. 56, no. 10, pp. 1748-1749, 1968.
- <sup>19</sup> R.A. Moore, J.T. Haynes, and B.R. McAvoy, "High overtone bulk resonator stabilized microwave sources", *Proc. IEEE Ultrasonics Symp.*, pp. 414-424, 1981.
- <sup>20</sup> M.M. Driscoll, R.A. Jelen, and N. Matthews, "Extremely low phase noise UHF oscillators utilizing high-overtone bulk acoustic resonators", *Proc. IEEE Ultrasonics Symp.*, pp. 513-518, 1990.
- <sup>21</sup> M.M. Driscoll, "Low noise microwave signal generation: resonators / oscillator comparisons", *IEEE MTT-S Intl. Microwave Symp. Digest*, pp. 261-264, 1989.
- <sup>22</sup> K.E. Peterson, "Silicon as a mechanical material", *IEEE Proc.*, vol. 70, no. 3, pp. 420-457, 1982.
- <sup>23</sup> K.M. Lakin and J.S. Wang, "UHF composite bulk wave resonators", *Proc. IEEE Ultrasonics Symp.*, pp. 834-837, 1980.
- <sup>24</sup> T.W. Grudkowski, J.F. Black, and T.M. Reeder, "Fundamental mode VHF / UHF bulk acoustic wave resonators and filters on silicon", *Proc. IEEE Ultrasonics Symp.*, pp. 829-833, 1980.
- <sup>25</sup> J.S. Wang and K.M. Lakin, "Low-temperature coefficient bulk acoustic wave composite resonators", *Appl. Phys. Lett.*, vol. 40, no. 4, pp. 308-310, 1982.
- <sup>26</sup> K.M. Lakin, J.S. Wang, G.R. Kline, A.R. Landin, Y.Y. Chen, and J.D. Hunt, "Thin film resonators and filters", *Proc. IEEE Ultrasonics Symp.*, pp. 466-475, 1982.



- 
- <sup>27</sup> G.R. Kline and K.M. Lakin, "1.0-GHz thin-film bulk acoustic wave resonators on GaAs", *Appl. Phys. Lett.*, vol. 43, no. 8, pp. 750-751, 1983.
- <sup>28</sup> M.M. Driscoll, R.A. Moore, J.F. Rosenbaum, S.V. Krishnaswamy, and J.R. Szedon, "Recent advances in monolithic film resonator technology", *Proc. IEEE Ultrasonics Symp.*, pp. 365-369, 1986.
- <sup>29</sup> S.V. Krishnaswamy, J. Rosenbaum, S. Horwitz, C. Vale, and R.A. Moore, "Film bulk acoustic wave resonator technology", *Proc. IEEE Ultrasonics Symp.*, pp. 529-536, 1990.
- <sup>30</sup> K.M. Lakin, J.S. Wang, and A.R. Landin, "Aluminum nitride thin film and composite bulk wave resonators", *Proc. IEEE Freq. Control Symp.*, pp. 517-524, 1982.
- <sup>31</sup> K.M. Lakin, G.R. Kline, and K.T. McCarron, "Development of miniature filters for wireless applications", *IEEE Trans. Microwave Theory and Techniques*, vol. 42, no. 12, pp. 2933-2939, 1995.
- <sup>32</sup> D. Cushman, K.F. Lau, E.M. Garber, K.A. Mai, A.K. Oki, and K.W. Kobayashi, "SBAR filter monolithically integrated with HBT amplifier", *Proc. IEEE Ultrasonics Symp.*, pp. 519-524, 1990.
- <sup>33</sup> R. Ruby and P. Merchant, "Micromachined thin film bulk acoustic resonators", *Proc. IEEE Freq. Control Symp.*, pp. 135-138, 1994.
- <sup>34</sup> R. Ruby, "Micromachined cellular filters", *IEEE MTT-S Intl. Microwave Symp. Digest*, pp. 1149-1152, 1996.
- <sup>35</sup> J.D. Larson, R. Ruby, P. Bradley, and Y. Oshmyansky, "A BAW antenna duplexer for the 1900 MHz PCS band", *Proc. IEEE Ultrasonics Symp.*, pp. 887-890, 1999.
- <sup>36</sup> J.D. Larson, P.D. Bradley, S. Wartenberg, and R.C. Ruby, "Modified Butterworth-Van Dyke circuit for FBAR resonators and automated measurement system", *Proc. IEEE Ultrasonics Symp.*, pp. 863-868, 2000.
- <sup>37</sup> K. Wang, W. Mueller, R. Ruby, M. Gat, P. Bradley, A. Barfknecht, F. Geefay, C. Han, G. Gan, A. Chien, and B. Ly, "High rejection RX filters for GSM handsets with wafer level packaging", *Proc. IEEE Ultrasonics Symp.*, pp. 925-929, 2002.

- 
- <sup>38</sup> K.M. Lakin, G.R. Kline, and K.T. McCarron, "Development of miniature filters for wireless applications", *IEEE Trans. Microwave Theory and Techniques*, vol. 42, no. 12, pp. 2933-2939, 1995.
- <sup>39</sup> G.G. Fattinger, J. Kaitila, R. Aigner, and W. Nessler, "Single-to-balanced filters for mobile phones using coupled resonator BAW technology", *Proc. IEEE Ultrasonics Symp.*, pp. 416-419, 2004.
- <sup>40</sup> R. Aigner, "MEMS in RF-filter applications: thin film bulk-acoustic-wave technology", *Proc. of Transducers '05*, pp. 5-8, 2005.
- <sup>41</sup> G. Piazza, P.J. Stephanou, J.M. Porter, M.B.J. Wijesundara, and A.P. Pisano, "Low motional resistance ring-shaped contour-mode aluminum nitride piezoelectric micromechanical resonators for UHF applications", *Proc. IEEE Intl. Conf. on MEMS*, pp. 20-23, 2005.
- <sup>42</sup> J. Wang, Z. Ren, and C.T.-C. Nguyen, "1.156-GHz self-aligned vibrating micromechanical disk resonator", *IEEE Trans. Ultrasonics, Ferroelectrics, and Frequency Control*, vol. 51, no. 12, pp. 1607-1628, 2004.
- <sup>43</sup> R. Ruby, P. Bradley, D. Clark, D. Feld, T. Jamneala, and K. Wang, "Acoustic FBAR for filters, duplexers, and front end modules", *IEEE MTT-S Intl. Microwave Symp. Digest*, pp. 931-934, 2004.
- <sup>44</sup> S. Smyser (private communication), 2005.
- <sup>45</sup> R. White (private communication), 2006.
- <sup>46</sup> S.G. Burns and R.S. Ketcham, "Fundamental-mode pierce oscillators utilizing bulk-acoustic-wave resonators in the 250-300 MHz Range", *IEEE MTT-S Intl. Microwave Symp. Digest*, pp. 83-84, 1984.
- <sup>47</sup> M.M. Driscoll, S.V. Krishnaswamy, R.A. Moore, and J.R. Szedon, "UHF film resonator evaluation and resonator-controlled oscillator design using computer aided design techniques", *Proc. IEEE Ultrasonics Symp.*, pp. 411 – 416, 1984.
- <sup>48</sup> H. Satoh, H. Suzuki, C. Takahashi, C. Narahara, and Y. Ebata, "A 400 MHz one-chip oscillator using an air-gap type thin film resonator", *Proc. IEEE Ultrasonics Symp.*, pp. 363-368, 1987.

- 
- <sup>49</sup> W.A. Burkland, A.R. Landin, G.R. Kline, and R.S. Ketcham, "A thin-film bulk-acoustic-wave resonator-controlled oscillator on silicon", *IEEE Electron Dev. Lett.*, vol. EDL-8, no. 11, pp. 531-533, 1987.
- <sup>50</sup> S.G. Burns, G.R. Kline, and K.M. Lakin, "UHF oscillator performance using thin film resonator based topologies", *Proc. of the IEEE Freq. Control Symp.*, pp. 382-387, 1987.
- <sup>51</sup> S.G. Burns and R.J. Weber, "Design and performance of UHF and L-band oscillators using thin-film resonators on semiconductor substrates", *Proc. 34th Midwest Symp. Circuits and Systems*, pp. 307 – 310, 1991.
- <sup>52</sup> R.J. Weber, S.G. Burns, and S.D. Braymen, "A semiconductor process for cointegration of BAW thin-film piezoelectrics with microwave BJTs", *Proc. of the IEEE Ultrasonics Symp.*, pp. 525 – 528, 1990.
- <sup>53</sup> B.P. Otis and J.M. Rabaey, "A 300  $\mu$ W 1.9 GHz CMOS Oscillator Utilizing Micromachined Resonators", *Proc. 28<sup>th</sup> European Solid-State Circuits Conf.*, pp. 151-154, 2002.
- <sup>54</sup> G. Sauerbrey, "Use of oscillator quartz crystals for weighing thin layers and microweighing", *Zeitschrift fur Physik*, vol. 155, pp. 206-222, 1959.
- <sup>55</sup> W.H. King, "Piezoelectric Sorption Detector", *Anal. Chem.*, vol. 36, no. 9, pp. 1735-1739, 1964.
- <sup>56</sup> T. Nakamoto, Y. Suzuki, and T. Moriizumi, "Study of VHF-band QCM gas sensor", *Sensors and Actuators B (Chemical)*, vol. 84, pp. 98-105, 2002.
- <sup>57</sup> H. Huang, J. Zhou, S. Chen, L. Zeng, and Y. Huang, "A highly sensitive QCM sensor coated with  $\text{Ag}^+$ -ZSM-5 film for medical diagnosis", *Sensors and Actuators B (Chemical)*, vol. 101, pp. 316-321, 2004.
- <sup>58</sup> C.K. O'Sullivan and G.G. Guibault, "Commercial quartz crystal microbalances - theory and applications", *Biosensors & Bioelectronics*, vol. 14, pp. 663-670, 1999.

- 
- <sup>59</sup> J. Hartmann, P. Hauptmann, S. Levi, and E. Dalcanele, "Chemical sensing with cavitands: influence of cavity shape and dimensions on the detection of solvent vapors", *Sensors and Actuators B (Chemical)*, vol. 35-36, pp. 154-157, 1996.
- <sup>60</sup> D. Cullen and T. Reeder, "Measurement of SAW velocity versus strain for YX and ST quartz", *Proc. IEEE Ultrasonics Symp.*, pp. 441-444, 1975.
- <sup>61</sup> H. Wohltjen and R. Dessy, "Surface Acoustic Wave Probes for Chemical Analysis, II. Gas Chromatography Detector", *Anal. Chem.*, vol. 51, pp. 1465-1470, 1979.
- <sup>62</sup> H. Wohltjen, "Mechanisms of Operation and Design Considerations for Surface Acoustic Wave Device Vapour Sensors", *Sensors and Actuators*, vol. 5, pp. 307-325, 1984.
- <sup>63</sup> D.S. Ballantine, R.M. White, S.J. Martin, A.J. Ricco, G.C. Frye, E.T. Zellers, and H. Wohltjen, *Acoustic Wave Sensors: Theory, Design, and Physiochemical Applications*, Boston: Academic Press, 1997.
- <sup>64</sup> E.J. Staples, "The First Quantitative Validated Electronic Nose for Environmental Testing of Air, Water, and Soil", *Proc. Amer. Chem. Soc.*, 2000.
- <sup>65</sup> A. Pohl, G. Ostermayer, L. Reindl, and F. Seifert, "Monitoring the tire pressure at cars using passive SAW sensors", *Proc. IEEE Ultrasonics Symp.*, pp. 471-474, 1997.
- <sup>66</sup> D.W. Galipeau, J.D. Stroschine, K.A. Snow, K.A. Vetelino, K.R. Hines, and P.R. Story, "A study of condensation and dew point using a SAW sensor", *Sensors and Actuators B (Chemical)*, vol. 25, no. 1, pp. 696-700, 1995.
- <sup>67</sup> M. Kurosawa, Y. Fukuda, M. Takasaki, and T. Higuchi, "A surface acoustic wave gyro sensor", *Proc. Transducers*, pp. 863-866, 1997.
- <sup>68</sup> S.W. Wenzel and R.M. White, "Flexural plate wave gravimetric chemical sensor", *Sensors and Actuators*, vol. A21-A23, pp. 700-703, 1990.
- <sup>69</sup> B. Cunningham, M. Weinberg, J. Pepper, C. Clapp, R. Bousquet, B. Hugh, R. Kant, C. Daly, and E. Huser, "Design, fabrication and vapor characterization of a microfabricated flexural plate

---

resonator sensor and application to integrated sensor arrays”, *Sensors and Actuators B (Chemical)*, vol. 73, pp. 112-123, 2001.

<sup>70</sup> J.W. Grate, S.W. Wenzel, and R.M. White, “Flexural plate wave devices for chemical analysis”, *Anal. Chem.*, vol. 63, pp. 1552-1561, 1991.

<sup>71</sup> S.W. Wenzel and R.M. White, “Flexural plate-wave sensor: chemical vapor sensing and electrostrictive excitation”, *Proc. IEEE Ultrasonics Symp.*, pp. 595-598, 1989.

<sup>72</sup> A.W. Wang, “Gel-coated FPW Biosensors”, M.S. Thesis, U.C. Berkeley, Berkeley, CA, 1993.

<sup>73</sup> A.W. Wang, R. Kiwan, R.M. White, and R.L. Ceriani, “A silicon-based ultrasonic immunoassay for detection of breast cancer antigens”, *Sensors and Actuators B (Chemical)*, vol. B49, pp. 13-21, 1998.

<sup>74</sup> B.A. Martin, S.W. Wenzel, and R.M. White, “Viscosity and density sensing with ultrasonic plate waves”, *Sensors and Actuators A (Physical)*, vol. A22, pp. 704-708, 1990.

<sup>75</sup> R.J. Weber, S.G. Burns, C.F. Campbell, and R. O’Toole, “Applications of AlN thin-film resonator topologies as antennas and sensors”, *IEEE MTT-S Intl. Microwave Symp. Digest*, pp. 161-164, 1992.

<sup>76</sup> R.P. O’Toole, S.G. Burns, G.J. Bastiaans, and M.D. Porter, “Thin aluminum nitride film resonators: miniaturized high sensitivity mass sensors”, *Anal. Chem.*, vol. 64, pp. 1289-1294, 1992.

<sup>77</sup> P.H. Kobrin, C.W. Seabury, A.B. Harker, and R.P. O’Toole, “Thin film resonant chemical sensor with resonant acoustic isolator”, *United States Patent*, 5,936,150, August 10, 1999.

<sup>78</sup> H. Zhang and E.S. Kim, “Vapor and liquid mass sensing by micromachined acoustic resonator”, *Proc. IEEE Intl. Conf. on MEMS*, pp. 470-473, 2003.

<sup>79</sup> H. Zhang, M.S. Marma, E.S. Kim, C.E. McKenna, and M.E. Thompson, “Implantable resonant mass sensor for liquid biochemical sensing”, *Proc. IEEE Intl. Conf. on MEMS*, pp. 347- 350, 2004.

<sup>80</sup> H. Zhang and E.S. Kim, “Micromachined acoustic resonant mass sensor”, *J. Microelectromechanical Sys.*, vol. 14, no. 4, pp. 699-706, 2005.

- 
- <sup>81</sup> H. Zhang, M.S. Marma, E.S. Kim, C.E. McKenna, and M.E. Thompson, "A film bulk acoustic resonator in liquid environments", *J. Micromechanics and Microengineering*, vol 15, pp. 1911-1916, 2005.
- <sup>82</sup> R. Gabl, E. Green, M. Schreiter, H.D. Feucht, H. Zeininger, R. Primig, D. Pitzer, G. Eckstein, W. Wersing, W. Reichl, and J. Runch, "Novel integrated FBAR sensors: a universal technology platform for bio- and gas-detection", *Proc. IEEE Sensors Conf.*, pp. 1184-1188, 2003.
- <sup>83</sup> W. Reichl, J. Runch, M. Schreiter, E. Green, and R. Gabl, "Novel gas sensors based on thin film bulk acoustic resonators", *Proc. IEEE Sensors Conf.*, pp. 1504 – 1505, 2004.
- <sup>84</sup> R. Bredelow, S. Zauner, A.L. Scholtz, K. Aufinger, W. Simburger, C. Paulus, A. Martin, M. Fritz, H.J. Timme, H. Heiss, S. Marksteiner, L. Elbrecht, R. Aigner, and R. Thewes, "Biochemical sensors based on bulk acoustic wave resonators", *Proc. Intl. Electron Dev. Meet.*, pp. 32.7.1 – 32.7.3, 2003.
- <sup>85</sup> R.L. Chuan, "An instrument for the direct measurement of particulate mass", *J. Aerosol Sci.*, vol. 1, pp. 111-114, 1970.
- <sup>86</sup> W.D. Bowers and R.L. Chuan, "Surface acoustic-wave piezoelectric crystal aerosol mass microbalance", *Rev. Sci. Inst.*, vol. 60, no. 7, pp. 1297-1302, 1989.
- <sup>87</sup> W.D. Bowers, R.L. Chuan, and T.M. Duong, "A 200 MHz surface acoustic wave resonator mass microbalance", *Rev. Sci. Inst.*, vol. 62, no. 6, pp. 1624-1629, 1991.
- <sup>88</sup> J.G. Olin, G.J. Sem, and D.L. Christenson, "Piezoelectric-electrostatic aerosol mass concentration monitor", *Amer. Industrial Hygiene Association J.*, vol. 32, pp. 209-220, 1971.
- <sup>89</sup> G.J. Sem and K. Tsurubayashi, "A new mass sensor for respirable dust measurement", *Amer. Industrial Hygiene Association J.*, vol. 36, pp. 791-800, 1975.
- <sup>90</sup> G.J. Sem, K. Tsurubayashi, and K. Homma, "Performance of the piezoelectric microbalance respirable aerosol sensor", *Amer. Industrial Hygiene Association J.*, vol. 38, pp. 580-588, 1977.
- <sup>91</sup> G.J. Sem, and P.S. Daley, "Performance evaluation of a new piezoelectric aerosol sensor", *Aerosol Measurement*, Gainesville: University Presses of Florida, pp. 672-686, 1979.

- 
- <sup>92</sup> G.J. Sem and F.R. Quant, “Automatic piezobalance respirable aerosol mass monitor for unattended real-time measurements”, in *Aerosols in the Mining and Industrial Work Environments: Volume 3 Instrumentation*, Ann Arbor: Ann Arbor Science, pp. 1039-1054, 1983.
- <sup>93</sup> F. Zheng, “Thermophoresis of spherical and non-spherical particles: a review of theories and experiments”, *Advances in Colloid and Interface Science*, vol. 97, pp. 255-278, 2002.
- <sup>94</sup> J.R. Brock, “On the theory of thermal forces acting on aerosol particles”, *J. Colloid Sci.*, vol. 17, pp. 768-780, 1962.
- <sup>95</sup> T.W. Kethley, M.T. Gordon, and C. Orr, “A thermal precipitator for aerobacteriology”, *Science*, vol. 116, no. 3014, pp. 368-369, 1952.
- <sup>96</sup> C. Orr, M.T. Gordon, and M.C. Kordecki, “Thermal precipitation for sampling air-borne microorganisms”, *Appl. Microbiology*, vol. 4, no. 3, pp. 116-118, 1956.
- <sup>97</sup> D. Gonzales, A.G. Nasibulin, A.M. Baklanov, S.D. Shandakov, D.P. Brown, P. Queipo, and E.I. Kauppinen, “A New Thermophoretic Precipitator for Collection of Nanometer-Sized Aerosol Particles”, *Aerosol Sci. and Tech.*, vol. 39, pp. 1064-1071, 2005.

## **2 Principle of Operation of MEMS PM Monitor**

In this chapter, the theory governing the operation of the FBAR mass sensor and CMOS sustaining oscillator is described. The FBAR input admittance and mode shape is first derived using a direct solution of coupled differential equations. A second admittance derivation using electromechanical transmission lines is then presented. Finally, the startup behavior and resonant frequency of the CMOS Pierce oscillator are derived using small-signal loop-gain and negative resistance models.

### **2.1 FBAR Admittance and Mode Shape**

The admittance and particle displacement of the FBAR may be derived from one-dimensional, electromechanical differential equations subject to displacement and stress boundary conditions at the interfaces between layers<sup>1,2,3</sup>. As shown in the cross-section of Figure 2.1, the MEMS PM FBAR consisted of an AlN piezoelectric film sandwiched between platinum (Pt) and aluminum (Al) electrodes. PM is deposited onto the Al electrode. As will be discussed in Chapter 3, this four-layer model also facilitates analysis of an early ZnO FBAR design used in a series of preliminary mass detection experiments.



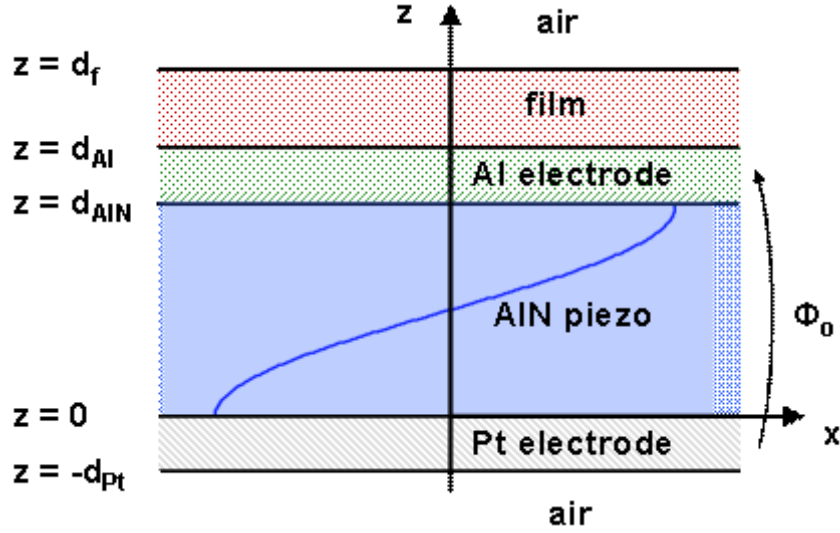


Figure 2.1: Cross-section of the AlN FBAR and geometry used in the boundary-value solution.

To simplify the analysis, a one-dimensional solution for particle displacement in the  $z$ -direction is sought. This thickness-extensional (TE) mode consists of two counter-propagating waves with polarization and displacement along the  $z$ -axis:

$$u_z(z, t) = (A_1 e^{jkz} + A_2 e^{-jkz}) e^{j\omega t} \quad \text{Eq. 2.1}$$

where:

$u_z(z, t)$	particle displacement component in $z$ -direction (m);
$k = \beta - j\alpha$	wavenumber (1 / m);
$\beta = 2\pi / \lambda$	propagation constant (1 / m);
$\alpha$	attenuation constant (1 / m);
$\omega$	angular frequency (rad / sec);
$\lambda$	acoustic wavelength (1 / m);
$A_1, A_2$	constants of integration.

Conservation of linear momentum requires that inertial, body, and surface traction forces sum to zero. For an infinitesimal volume of the resonator, this force balance is expressed in vector form as:

$$\nabla \cdot \mathbf{T} + \bar{\mathbf{f}} = \rho \ddot{\mathbf{u}} \quad \text{Eq. 2.2}$$

where

$\mathbf{T}$	6 x 1 stress vector representing independent elements of stress tensor at a material point (N / m <sup>2</sup> );
$\ddot{\mathbf{u}}$	second time derivative of the displacement vector (m / s <sup>2</sup> );
$\rho$	mass density (kg / m <sup>3</sup> );
$\bar{\mathbf{f}}$	body forces per unit volume (N / m <sup>3</sup> ) (equal to zero for this analysis).

The stress in the piezoelectric film may be shown to be<sup>1</sup>:

$$\mathbf{T} = c^E \mathbf{S} + \eta \frac{d\mathbf{S}}{dt} - e \bar{\mathbf{E}} \quad \text{Eq. 2.3}$$

where:

$\mathbf{S}$	6 x 1 strain vector representing independent strain elements at a material point (unit-less);
$c^E$	stiffness matrix at constant (zero) electric field (N / m <sup>2</sup> );
$\bar{\mathbf{E}}$	electric field (V / m);
$e$	piezoelectric constant (C / m <sup>2</sup> );
$\eta$	material viscosity coefficient (N·s / m <sup>2</sup> ).

Eq. 2.3 is Hooke's law with two added terms, one to model viscous material loss and a second that expresses piezoelectric coupling between the stress and electric field. Eq. 2.3 applies also to the non-piezoelectric FBAR layers (see Figure 2.1) if  $e \equiv 0$  and the superscript on the stiffness is omitted.

The electric displacement in the piezoelectric film is given by:

$$\vec{\mathbf{D}} = \epsilon^s \vec{\mathbf{E}} + e\mathbf{S} \quad \text{Eq. 2.4}$$

where:

$$\begin{array}{ll} \vec{\mathbf{D}} & \text{electric displacement vector (C / m}^2\text{);} \\ \epsilon^s & \text{material permittivity at constant (zero) strain (F / m);} \end{array}$$

Since there is no free space charge in the piezoelectric film, the gradient of the electric displacement is zero:

$$\nabla \cdot \vec{\mathbf{D}} = \rho_f = 0 \quad \text{Eq. 2.5}$$

In fact, for longitudinal waves propagating along the c-axis of hexagonal crystals such as AlN, it can be readily shown that  $\vec{\mathbf{D}}$  itself is identically zero<sup>1</sup>.

Restricting the analysis to one-dimensional longitudinal displacements in the z-direction, for the piezoelectric layer Eq. 2.3 reduces to:

$$T_{33} = c_{33}^E \frac{\partial u_z}{\partial z} + \eta \frac{\partial^2 u_z}{\partial z \partial t} + e_{33} \frac{\partial \phi}{\partial z} \quad \text{Eq. 2.6}$$

where  $\phi$  is the potential and  $\vec{\mathbf{E}} = -\nabla \phi$ . For the non-piezoelectric layers, Eq. 2.6 applies with  $e \equiv 0$ . Similarly, Eq. 2.4 for the piezoelectric film reduces to:

$$D_3 = \epsilon_{33}^s E_3 + e_{33} \frac{\partial u_z}{\partial z} \quad \text{Eq. 2.7}$$

From Eq. 2.2, Eq. 2.3, and Eq. 2.5:

$$\bar{c}_{33} \frac{\partial^2 u_z}{\partial z^2} = \rho \frac{\partial^2 u_z}{\partial t^2} \quad \text{Eq. 2.8}$$

where, for the piezoelectric layer,

$$\bar{c}_{33} = c_{33}^E + \frac{e_{33}^2}{\epsilon^S} + j\omega\eta = c_{33}^E(1 + k_t^2) + j\omega\eta = c_{33}' + j\omega\eta \quad \text{Eq. 2.9}$$

Here  $c_{33}'$  is the piezoelectrically stiffened modulus and  $k_t^2$  is the electromechanical coupling coefficient of the piezoelectric:

$$k_t^2 = \frac{e_{33}^2}{\epsilon^S c_{33}^E} \quad \text{Eq. 2.10}$$

It is also useful to define a complex coupling coefficient:

$$\bar{k}_t^2 = \frac{e_{33}^2}{\epsilon^S \bar{c}_{33}^E} \quad \text{Eq. 2.11}$$

Superscripts denoting piezoelectric boundary conditions (e.g.,  $\epsilon^S$ ) are dropped in the subsequent analysis. For the non-piezoelectric layers the complex stiffness is:

$$\bar{c}_{33} = c_{33} + j\omega\eta \quad \text{Eq. 2.12}$$

In steady state, the general solution for the wave equation of Eq. 2.8 is the harmonic solution of Eq. 2.1. For example, in the AlN piezoelectric film and Pt bottom electrode the particle displacements are:

$$u_z(z, t)_{AlN} = (Ae^{jk_{AlN}z} + Be^{-jk_{AlN}z})e^{j\omega t} \quad \text{Eq. 2.13}$$

$$u_z(z, t)_{Pt} = (Ce^{jk_{Pt}z} + De^{-jk_{Pt}z})e^{j\omega t} \quad \text{Eq. 2.14}$$

The wavenumber  $k$  for each material is:

$$k = \frac{\omega}{\sqrt{\frac{\bar{c}_{33}}{\rho}}} = \beta - j\alpha \quad \text{Eq. 2.15}$$

where, with the phase velocity given by  $v_p$ :

$$\beta = \frac{\omega}{\sqrt{\frac{c_{33}}{\rho}}} = \frac{\omega}{v_p} \quad \text{Eq. 2.16}$$

For non-piezoelectric materials, the propagation constant is calculated employing the material stiffness  $c_{33}$ . An important material property used in our subsequent analysis is the acoustic impedance  $Z$ , defined as the ratio of the stress  $\mathbf{T}$  to the particle velocity  $\bar{\mathbf{v}}$ <sup>1</sup>:

$$Z = \frac{\mathbf{T}}{\bar{\mathbf{v}}} = \rho v_p = \sqrt{\rho c_{33}} \quad \text{Eq. 2.17}$$

From Eq. 2.5, the electric potential may be determined as:

$$\phi(z, t) = \frac{e_{33}}{\epsilon_{33}} u_z(z, t)_{AlN} + (Ez + F)e^{j\omega t} \quad \text{Eq. 2.18}$$

where  $E$  and  $F$  are constants of integration determined from the boundary conditions ( $E$  is *not* the electric field in the  $z$ -direction, which given by  $\vec{\mathbf{E}} = E_3 \hat{\mathbf{z}}$ ). The potential at the bottom and top electrodes prescribes two electrical boundary conditions. At  $z = 0$ , the bottom electrode, a potential is applied with form:

$$\phi(0, t) = \frac{\phi_0}{2} e^{j\omega t} \quad \text{Eq. 2.19}$$

Eq. 2.13 and Eq. 2.18 yield the electrical boundary condition:

$$\frac{e_{33}}{\epsilon_{33}} (A + B) + F = \frac{\phi_0}{2} \quad \text{Eq. 2.20}$$

Similarly, at  $z = d_{AlN}$ , the top electrode potential is prescribed as:

$$\phi(d_{AlN}, t) = -\frac{\phi_0}{2} e^{j\omega t} \quad \text{Eq. 2.21}$$

Eq. 2.13 and Eq. 2.18 then yield a second electrical boundary condition:

$$\frac{e_{33}}{\epsilon_{33}} \left( A e^{jk_{AIN} d_{AIN}} + B e^{-jk_{AIN} d_{AIN}} \right) + E d_{AIN} + F = -\frac{\phi_o}{2} \quad \text{Eq. 2.22}$$

Continuity of stress and velocity at the boundary between material layers results in eight additional mechanical boundary conditions. At  $z = 0$  (see Figure 2.1), displacement must be continuous across the AlN / Pt interface. Equating Eq. 2.13 and Eq. 2.14 yields:

$$A + B = C + D \quad \text{Eq. 2.23}$$

At  $z = 0$ , the stress must also be continuous across the interface. From Eq. 2.6:

$$jk_{AIN} \bar{c}_{33_{AIN}} (A - B) + e_{33} E = j \bar{c}_{33_{Pt}} k_{Pt} (C - D) \quad \text{Eq. 2.24}$$

At  $z = -d_{Pt}$ , the Pt-air interface, the stress is zero, which requires:

$$C e^{-jk_{Pt} d_{Pt}} - D e^{jk_{Pt} d_{Pt}} = 0 \quad \text{Eq. 2.25}$$

Particle motions in the Al and PM layer are described by:

$$u_z(z, t)_{Al} = \left( G e^{jk_{Al} z} + H e^{-jk_{Al} z} \right) e^{j\omega t} \quad \text{Eq. 2.26}$$

$$u_z(z, t)_f = \left( I e^{jk_f z} + J e^{-jk_f z} \right) e^{j\omega t} \quad \text{Eq. 2.27}$$

At  $z = d_{AIN}$  (see Figure 2.1), the Al-AlN interface, displacement and stress must be continuous, consequently:

$$A e^{jk_{AIN} d_{AIN}} + B e^{-jk_{AIN} d_{AIN}} = G e^{jk_{Al} d_{AIN}} + H e^{-jk_{Al} d_{AIN}} \quad \text{Eq. 2.28}$$

$$j \bar{c}_{33_{AIN}} k_{AIN} (A e^{jk_{AIN} d_{AIN}} - B e^{-jk_{AIN} d_{AIN}}) + e_{33} E = j \bar{c}_{33_{Al}} k_{Al} (G e^{jk_{Al} d_{AIN}} - H e^{-jk_{Al} d_{AIN}}) \quad \text{Eq. 2.29}$$

Similarly, at  $z = d_{Al}$ , the equations for displacement and stress continuity are:

$$G e^{jk_{Al} d_{Al}} + H e^{-jk_{Al} d_{Al}} = I e^{jk_f d_{Al}} + J e^{-jk_f d_{Al}} \quad \text{Eq. 2.30}$$

$$jk_{Al} \bar{c}_{33_{Al}} (G e^{jk_{Al} d_{Al}} - H e^{-jk_{Al} d_{Al}}) = j k_f \bar{c}_{33_f} (I e^{jk_f d_{Al}} - J e^{-jk_f d_{Al}}) \quad \text{Eq. 2.31}$$

Finally, since at the top film-air interface  $z = d_f$ , the stress on the film is zero:

$$Ie^{jk_f d_f} - Je^{-jk_f d_f} = 0 \quad \text{Eq. 2.32}$$

With the layer thicknesses and material properties prescribed, the ten boundary conditions (Eq. 2.20, Eq. 2.22, Eq. 2.23, Eq. 2.24, Eq. 2.25, and Eq. 2.28 through Eq. 2.32) form a system of linear equations with ten unknowns (constants  $A$  through  $J$ ). The solution to this system of equations specifies the particle displacements and the resonator admittance.

The resonator current density is related to the electric displacement as:

$$\bar{\mathbf{J}} = \frac{\partial \bar{\mathbf{D}}}{\partial t} \quad \text{Eq. 2.33}$$

From Eq. 2.7 and Eq. 2.18, the current flowing from the bottom to top electrode in Figure 2.1 is:

$$I = -j\omega\epsilon_{33}\mathbf{A}Ee^{j\omega t} \quad \text{Eq. 2.34}$$

where  $\mathbf{A}$  is the resonator area ( $\text{m}^2$ ). The resonator admittance  $Y$  is expressed as:

$$Y = \frac{I}{V} = -j\omega\epsilon_{33}\mathbf{A}E \quad \text{Eq. 2.35}$$

It is useful to consider several limiting cases.

### 2.1.1 Acoustically Thin Electrodes with PM Layer

If the effect of the electrodes and PM film on the AlN resonator is negligible, constants  $C$ ,  $D$ ,  $G$ ,  $H$ ,  $I$ , and  $J$  can be approximated to be zero and the system of equations simplifies considerably. Expressions for  $A$ ,  $B$ , and  $E$  become:

$$A = \frac{je_{33}}{\bar{c}_{33AIN} k_{AIN}} \frac{\sin(\frac{k_{AIN} d_{AIN}}{2})}{\sin(k_{AIN} d_{AIN})} e^{-jk_{AIN} d_{AIN}} E \quad \text{Eq. 2.36}$$

$$B = \frac{-je_{33}}{\bar{c}_{33AIN} k_{AIN}} \frac{\sin(\frac{k_{AIN} d_{AIN}}{2})}{\sin(k_{AIN} d_{AIN})} e^{jk_{AIN} d_{AIN}} E \quad \text{Eq. 2.37}$$

$$E = \frac{-\phi_o}{d_{AIN} - \frac{2\bar{k}_t^2}{k_{AIN}} \tan \frac{k_{AIN} d_{AIN}}{2}} \quad \text{Eq. 2.38}$$

With  $E$  defined in Eq. 2.38, the expression for the admittance Eq. 2.35 is readily determined to be:

$$Y = \frac{j\omega C_o}{1 - \frac{2\bar{k}_t^2}{k_{AIN} d_{AIN}} \tan \frac{k_{AIN} d_{AIN}}{2}} \quad \text{Eq. 2.39}$$

where  $C_o$  is the static capacitance of the resonator:  $C_o = \frac{\epsilon_{33}\mathbf{A}}{d_{AIN}}$ . The magnitude and

phase of the admittance of a 2  $\mu\text{m}$  thick AlN resonator are plotted in Figure 2.2.

The following FBAR material constants were assumed:  $c_{33AIN} = 410 \text{ GPa}$ ,  $\rho_{AIN} = 3255 \text{ kg / m}^3$ ,  $e = 1.48 \text{ pC / m}^2$ ,  $\mathbf{A} = 15563 \text{ }\mu\text{m}^2$ ,  $\epsilon = 10.5$ ,  $\eta_{AIN} = 0.001 \text{ kg / s}\cdot\text{m}$ .



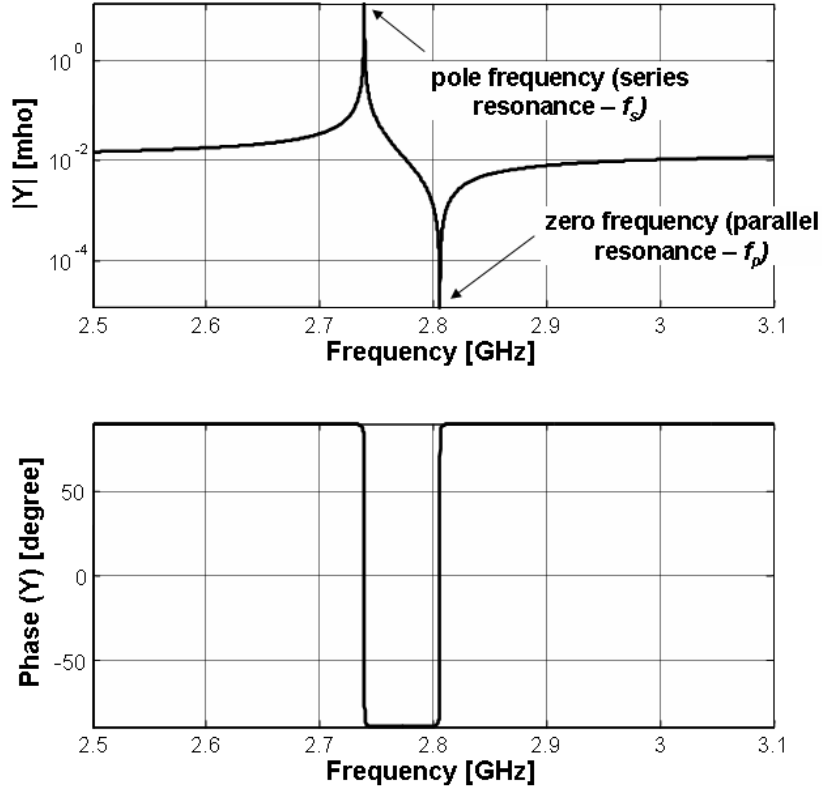


Figure 2.2: Magnitude and phase of the admittance of a resonator consisting of an unloaded 2  $\mu\text{m}$  AlN film. Between the pole and zero of the resonator, the admittance looks like a low-loss inductor; outside of this range the resonator admittance is capacitive.

From Eq. 2.39, the pole frequency ( $f_{max}$ ), where the magnitude of the admittance is at its maximum is:

$$\tan \frac{k_{AIN} d_{AIN}}{2} = \frac{k_{AIN} d_{AIN}}{2k_t^2} \quad \text{Eq. 2.40}$$

The zero frequency occurs where:

$$\frac{k_{AIN} d_{AIN}}{2} = N \frac{\pi}{2} \quad N = 1, 3, 5, \dots \quad \text{Eq. 2.41}$$

The resonator response can be further understood from Figure 2.3a, a parametric plot of the resonator conductance and susceptance from 1 to 4 GHz. The

two frequencies where the resonator looks real (zero susceptance) are defined as the series ( $f_s$ ) and parallel ( $f_p$ ) resonant frequencies, respectively. Between  $f_s$  and  $f_p$  the crystal looks like a low-loss inductor (admittance has  $-90^\circ$  phase) while outside this frequency range the crystal appears capacitive. As shown in Figure 2.3b, for high quality factor (Q) resonators such as the FBAR,  $f_s$  and  $f_p$  are essentially indistinguishable from the resonator admittance pole and zero frequencies given by Eq. 2.40 and Eq. 2.41. Thus approximating the admittance pole and zero with  $f_s$  and  $f_p$ , as is commonly done in the literature, introduces very little error (less than 1 ppm in this example).

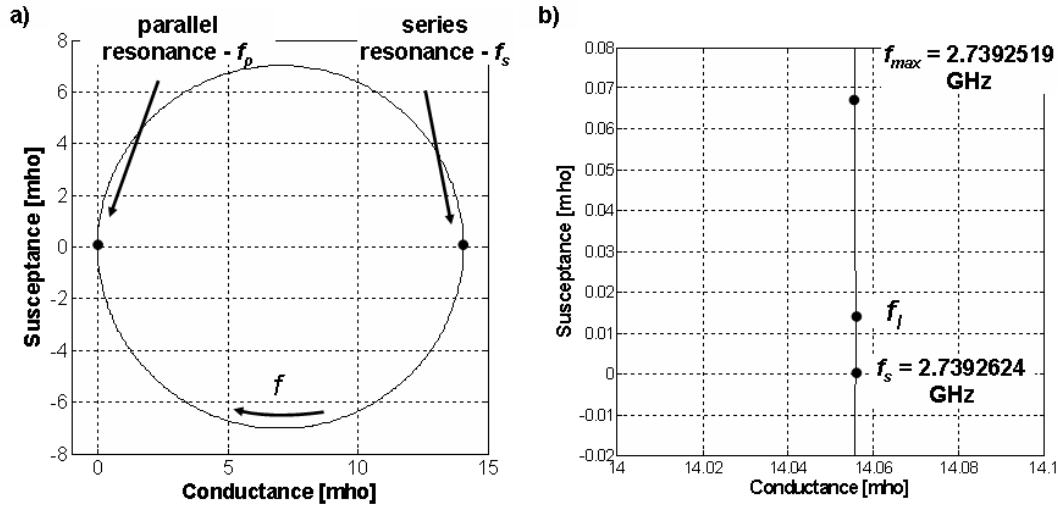


Figure 2.3: (a) Parametric plot of resonator conductance and susceptance from 1 GHz to 4 GHz; (b) plot of resonator conductance and susceptance in the vicinity of the series resonance. The maximum magnitude of the admittance ( $f_{max}$ ), maximum conductance ( $f_l$ ), and series resonance ( $f_s$ ) differ in frequency by less than 1 ppm. Thus approximating the admittance pole and zero with  $f_s$  and  $f_p$  introduces very little error.

For frequencies where the acoustic phase shift across the layer satisfies

$k_{AIN}dA_{IN} \cong N\pi$  (Eq. 2.41), Eq. 2.40 can be expanded as<sup>2</sup>:

$$\tan\left(\frac{k_{AIN}d_{AIN}}{2}\right) \cong \frac{k_{AIN}d_{AIN}}{(N\pi)^2 - (k_{AIN}d_{AIN})^2} \quad \text{Eq. 2.42}$$

With this approximation, the series resonant frequency simplifies considerably:

$$f_s = \frac{v_p}{2\pi d_{AIN}} \left[ (N\pi)^2 - 8k_t^2 \right]^{\frac{1}{2}} \quad \text{Eq. 2.43}$$

The mechanical quality factor of the resonator (at the series resonance) can also be shown to be:

$$Q_s = \frac{c_{33AIN}}{\omega_s \eta_{AIN}} \quad \text{Eq. 2.44}$$

Inspection of Eq. 2.36 and Eq. 2.37 shows that for small  $\eta_{AIN}$ ,  $A \cong B^*$  and the resonator mode shape in the piezoelectric AlN simplifies to:

$$u_z(z, t)_{AIN} = 2 \text{Re} \left\{ A e^{jk_{AIN}z} \right\} \quad \text{Eq. 2.45}$$

$$u_z(z, t)_{AIN} = \frac{-2e_{33} \sin\left(\frac{k_{AIN}d_{AIN}}{2}\right) \phi_o \sin\left[k_{AIN}\left(z - \frac{d_{AIN}}{2}\right)\right]}{\bar{c}_{33AIN} k_{AIN} \sin(k_{AIN}d_{AIN}) \left[ d_{AIN} - \frac{2\bar{k}_t^2 \tan\left(\frac{k_{AIN}d_{AIN}}{2}\right)}{k_{AIN}} \right]} \quad \text{Eq. 2.46}$$

Figure 2.4 plots the resonator amplitude and phase at the bottom surface ( $z = 0$ ) as a function of frequency. It is seen that for a high-Q resonator ( $\eta_{AIN} = 0.001 \text{ kg / s}\cdot\text{m}$ ), the mechanical resonance is less than 1 ppm from the series resonant frequency (in this case, less than 50 Hz). This result contrasts to that of some authors who report that the mechanical resonance corresponds most closely to the parallel resonance<sup>3,4</sup>. Figure 2.5 shows the resonator mode shape at the mechanical resonance.

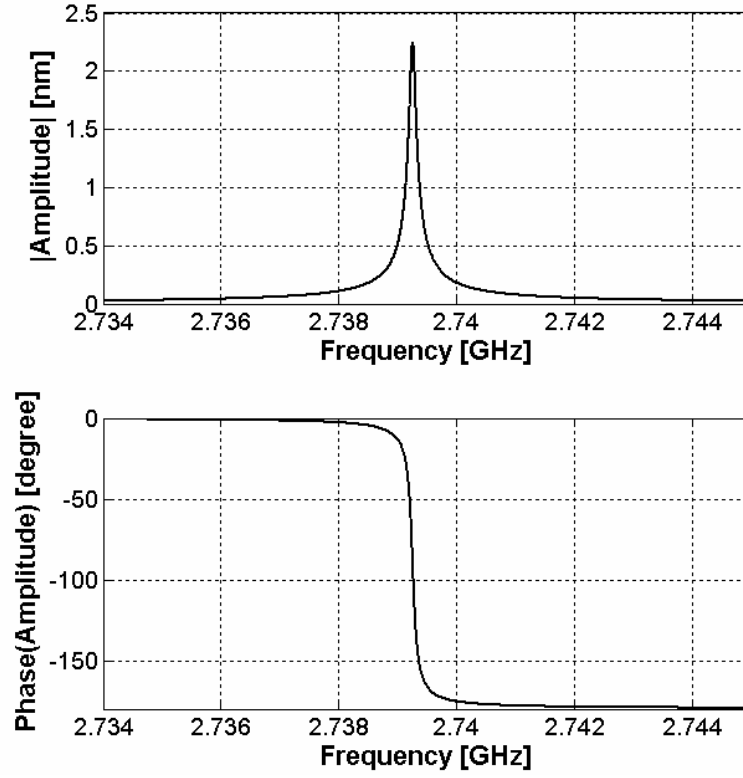


Figure 2.4: Magnitude and phase of the resonator displacement at the bottom surface of the crystal ( $z = 0$ ).

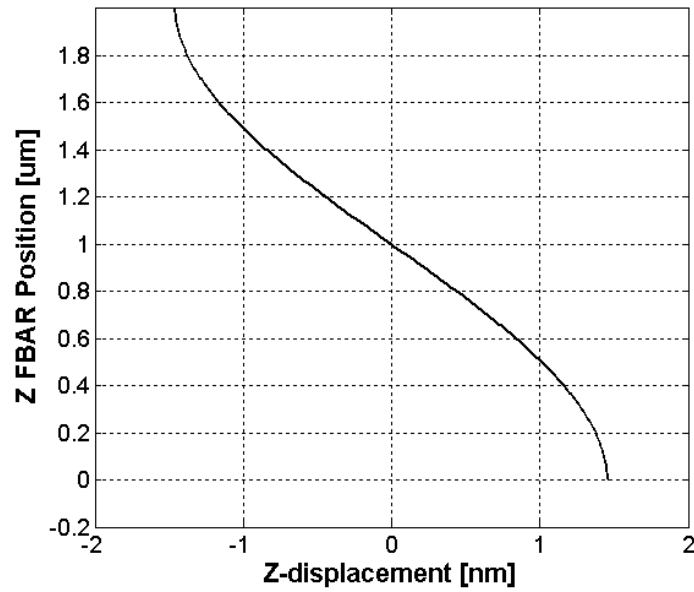


Figure 2.5: Resonator mode shape at the mechanical resonance.

As shown in Figure 2.6, near resonance the resonator can be modeled by a fixed capacitor in parallel with a motional impedance  $Z_m$  that models the electromechanical behavior:

$$Y = j\omega C_o + \frac{1}{Z_m} \quad \text{Eq. 2.47}$$

where, for an unloaded resonator  $Z_m = Z_{m_o}$  :

$$Z_{m_o} = \frac{1}{j\omega C_o} \left[ \frac{1}{\frac{2\bar{k}_t^2}{k_{AIN}d_{AIN}} \tan\left(\frac{k_{AIN}d_{AIN}}{2}\right)} - 1 \right] \quad \text{Eq. 2.48}$$

There is an important distinction between the currents flowing through the two branches of Figure 2.6. A displacement current flows through  $C_o$ . In contrast, the piezoelectric current in the motional branch originates from bound (paired) charge induced by strained atomic dipoles.

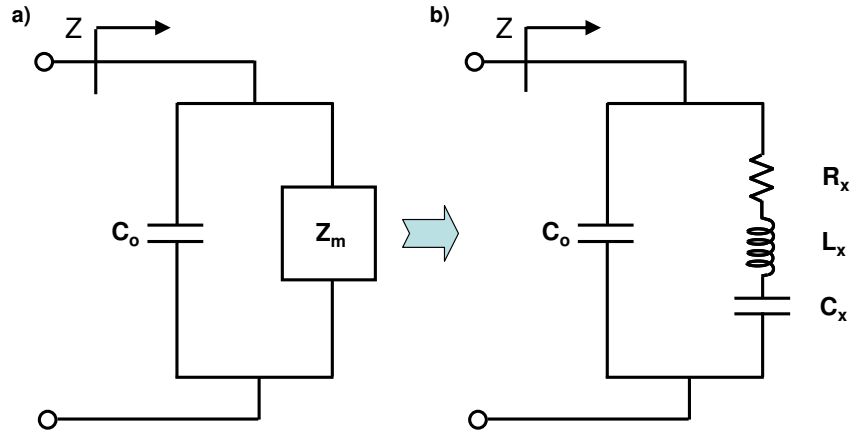


*Figure 2.6: Near resonance the impedance of the unloaded resonator consists of a static capacitor in parallel with an impedance  $Z_m$  that models the piezoelectric, motional behavior of the device; (b) The motional impedance of the resonator  $Z_m$  can be approximated by a series LCR circuit.*

By expanding  $k_{AIN}d_{AIN}$  for  $\omega$  in the vicinity of the series resonance  $\omega_s$  as<sup>5</sup>:

$$(k_{AIN}d_{AIN})^2 \cong \frac{(N\pi)^2 + 8k_t^2}{1 + \frac{j\omega\eta_{AIN}}{c_{33AIN}'}} \left(\frac{\omega}{\omega_s}\right)^2 = \frac{(N\pi)^2 + 8k_t^2}{1 + \frac{j}{Q_s}} \left(\frac{\omega}{\omega_s}\right)^2 \quad \text{Eq. 2.49}$$

We can express the motional impedance  $Z_m$  as:

$$Z_{m_o} = R_x + j\omega L_x + \frac{1}{j\omega C_x} \quad \text{Eq. 2.50}$$

where:

$$C_x = \frac{C_o 8k_t^2}{(N\pi)^2} \quad \text{Eq. 2.51}$$

$$R_x = \frac{(N\pi)^2 \eta_{AIN}}{8C_o c_{33AIN}' k_t^2} = \frac{\eta_{AIN}}{C_x c_{33AIN}'} = \frac{1}{C_x Q_s \omega_s} \quad \text{Eq. 2.52}$$

$$L_x = \frac{1}{C_o} \left[ \frac{1}{\omega^2} - \frac{1}{\omega_s^2} + \frac{(N\pi)^2}{8k_t^2 \omega_s^2} \right] \cong \frac{(N\pi)^2}{8C_o k_t^2 \omega_s^2} = \frac{1}{C_x \omega_s^2} \quad \text{Eq. 2.53}$$

The quality factor  $Q_s$  of the series resonance is then:

$$Q_s = \frac{\omega_s L_x}{R_x} = \frac{c_{33AIN}'}{\omega_s \eta_{AIN}} \quad \text{Eq. 2.54}$$

Figure 2.7 compares the admittance calculated from the lumped LCR approximation (Eq. 2.47) to that of the continuous model (Eq. 2.39). Good agreement is evident, though some discrepancy exists in the vicinity of the parallel resonance. The lumped elements of the intrinsic AlN layer are calculated to be  $C_x = 33.5$  fF,  $R_x = 0.073 \Omega$ ,  $L_x = 110.7$  nH, and  $C_o = 0.723$  pF.

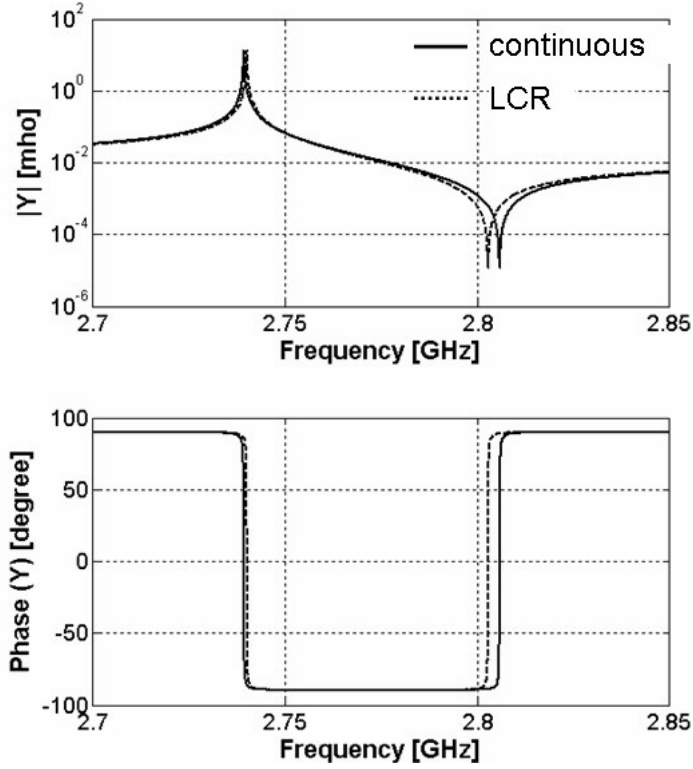


Figure 2.7: Admittance as derived from the continuous (Eq. 2.39, solid line) and lumped LCR (Eq. 2.47, dotted line) expressions.

### 2.1.2 Acoustically Thick Bottom FBAR Electrode

For ease of microfabrication, the FBARs employed a bottom Pt electrode, which, to minimize electrical loading, had a thickness of several hundred nanometers. Since the acoustic impedance of Pt is comparable to that of AlN, the electrode significantly alters the FBAR admittance. This Section quantifies the effect of an acoustically thick bottom electrode on the FBAR admittance. The effect of the top Al electrode is omitted, as this electrode is thinner (the resistivity of Al is five times smaller than that of platinum) and Al has a significantly lower acoustic impedance than AlN.

By solving the system of equations formed by the AlN and Pt layers (Eq. 2.20, Eq. 2.22, Eq. 2.23, Eq. 2.24, Eq. 2.25, and Eq. 2.28 with  $d_{Al} = 0$ ), the motional branch of the resonator impedance reduces to:

$$Z_m = \frac{1}{j\omega C_o} \left[ \frac{1 + \frac{Z_{Pt} \tan k_{Pt} d_{Pt}}{Z_{AlN} \tan k_{AlN} d_{AlN}}}{\frac{\bar{k}_t^2}{k_{AlN} d_{AlN}} \left( 2 \tan \left( \frac{k_{AlN} d_{AlN}}{2} \right) + \frac{Z_{Pt} \tan k_{Pt} d_{Pt}}{Z_{AlN}} \right)} - 1 \right] \quad \text{Eq. 2.55}$$

This expression can be partitioned into two terms:

$$Z_m = Z_{m_o} + Z_{m_{Pt}} \quad \text{Eq. 2.56}$$

The first term,  $Z_{m_o}$ , is the unloaded resonator impedance in Eq. 2.48. The second term models the effect of the bottom Pt electrode,  $Z_{m_{Pt}}$ :

$$Z_{m_{Pt}} = \frac{jk_{AlN} d_{AlN} Z_{Pt} \tan k_{Pt} d_{Pt}}{4Z_{AlN} \omega C_o \bar{k}_t^2} \frac{1}{1 + \frac{Z_{Pt} \tan k_{Pt} d_{Pt}}{2Z_{AlN} \tan \left( \frac{k_{AlN} d_{AlN}}{2} \right)}} \quad \text{Eq. 2.57}$$

Figure 2.8 compares the admittance for the unloaded FBAR to that of the FBAR with a 340 nm thick bottom electrode ( $\eta_{Pt} \sim 0.15 \text{ kg / s}\cdot\text{m}$ ,  $\rho_{Pt} = 21090 \text{ kg / m}^3$ ,  $c_{33Pt} = 320 \text{ GPa}$ ). The Pt electrode, with a comparable acoustic impedance ( $Z_{Pt} = 82.2 \times 10^6 \text{ kg}\cdot\text{m / s}$ ,  $Z_{AlN} = 36.5 \times 10^6 \text{ kg}\cdot\text{m / s}$ ) and high viscosity ( $\eta_{Pt} \sim 0.15 \text{ kg / s}\cdot\text{m}$ ,  $\eta_{AlN} \sim 0.001 \text{ kg / s}\cdot\text{m}$ ) as compared to AlN, alters the FBAR admittance by increasing the loss and lowering the resonant frequency.



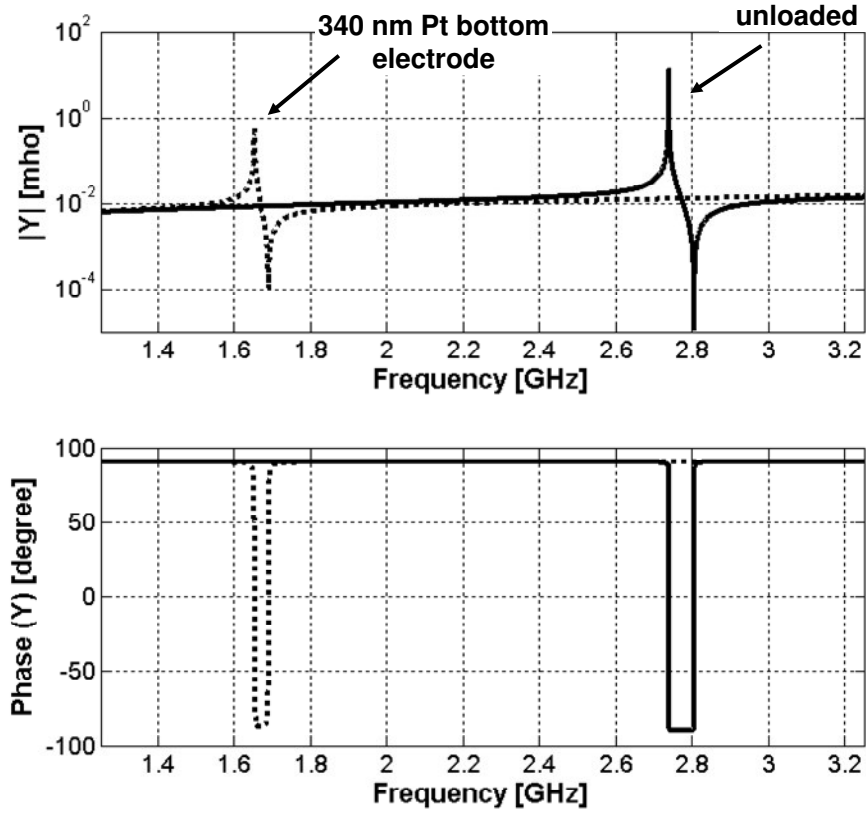


Figure 2.8: Admittance for an unloaded FBAR (solid line) and an FBAR loaded with a 340 nm thick bottom electrode (dotted line). The Pt electrode, with a similar acoustic impedance ( $Z_{Pt} = 82.2 \times 10^6 \text{ kg}\cdot\text{m/s}$ ,  $Z_{AlN} = 36.5 \times 10^6 \text{ kg}\cdot\text{m/s}$ ) and high viscosity ( $\eta_{Pt} \sim 0.15 \text{ kg/s}\cdot\text{m}$ ,  $\eta_{AlN} \sim 0.001 \text{ kg/s}\cdot\text{m}$ ) as compared to AlN, alters the FBAR admittance by increasing the loss and reducing the resonant frequency.

If  $Z_{Pt} \tan k_{Pt} d_{Pt} \ll Z_{AlN} \tan\left(\frac{k_{AlN} d_{AlN}}{2}\right)$ , implying physically that the

distributed acoustic impedance of the Pt is small relative to that of the AlN, the contribution from the Pt electrode to the impedance reduces to<sup>6</sup>:

$$Z_{m_{Pt}} = \frac{N\pi}{4\omega C_o \bar{k}_t^2} \left( \frac{jZ_{Pt} \tan k_{Pt} d_{Pt}}{Z_{AlN}} \right) \quad \text{Eq. 2.58}$$

For small  $k_{Pt} d_{Pt}$ , the impedance contribution can be simplified even further:

$$Z_{m_{Pt}} \cong j\omega \frac{(N\pi)\rho_{Pt}d_{Pt}}{4\omega_s C_o \bar{k}_t^2 \sqrt{\rho_{AlN} \bar{c}_{33AlN}}} \quad \text{Eq. 2.59}$$

Thus, ignoring loss, the added mass of the Pt electrode can be modeled by an extra inductor  $L_{Pt}$  in series with the original unloaded LCR:

$$L_{Pt} = \frac{2\omega_s \rho_{Pt} d_{Pt} L_x}{\pi \sqrt{\rho_{AlN} \bar{c}_{33AlN}}} \quad \text{Eq. 2.60}$$

Figure 2.9 compares the Pt-loaded FBAR admittance calculated using the LCR approximation Eq. 2.60 with the complete expression of Eq. 2.57. It is evident that for a thick electrode comprised of a high acoustic impedance material, the lumped inductor approximation introduces significant error.

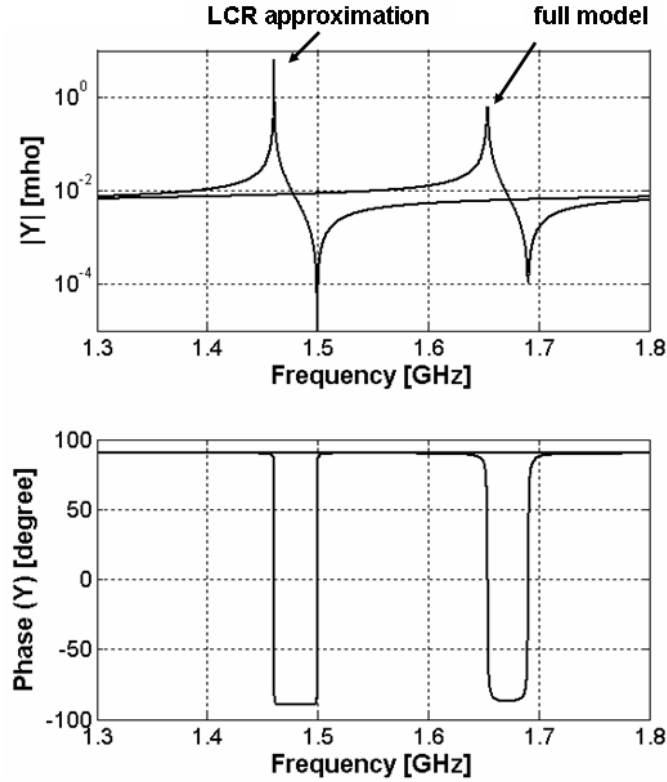


Figure 2.9: Comparison of the admittance of a 340 nm Pt-loaded FBAR calculated with the lumped LCR approximation (Eq. 2.60) to that calculated with the full expression (Eq. 2.57). Because of the distributed acoustic impedance of the Pt electrode, use of the linearized approximation introduces significant error.

By calculating the coefficients  $A$ ,  $B$ ,  $C$ , and  $D$  in MATLAB, one can plot the displacement in the 340 nm Pt loaded FBAR as in Figure 2.10. The peak FBAR amplitude,  $\sim 0.2$  nm, is fairly consistent with AFM measurements described in Chapter 3.

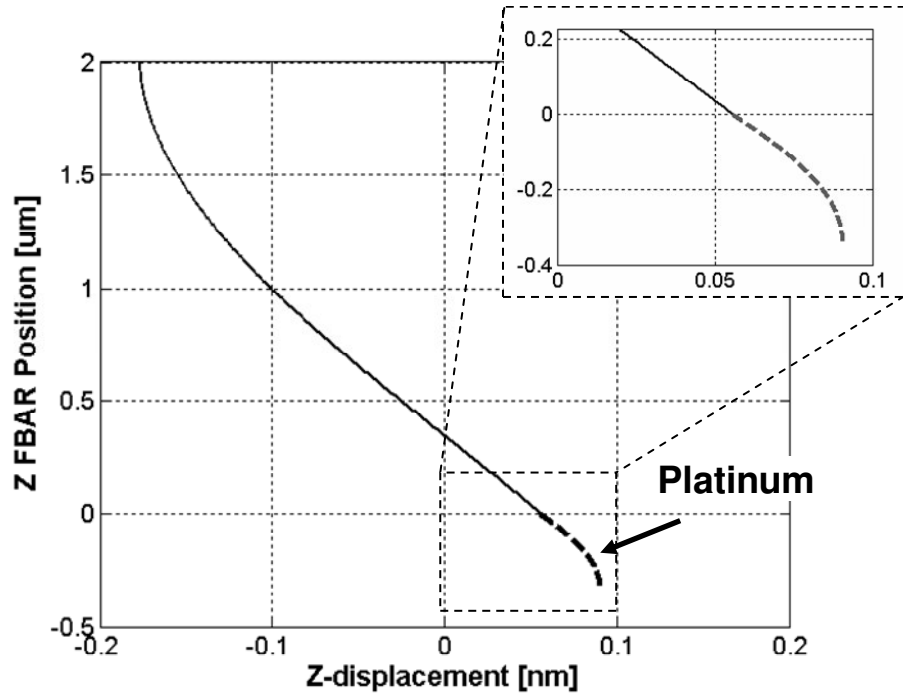


Figure 2.10: Resonator mode shape at the mechanical resonance of a 2  $\mu\text{m}$  thick AlN FBAR with a 340 nm Pt electrode at an input power of 0 dBm. Inset shows a close-up of the displacement in the Pt electrode. The AlN and Pt electrode displacements are given by the solid and dashed line, respectively.

## 2.2 FBAR Admittance Derived from Transmission-Line Mason Model

For multiple layers, the system of differential equations described in Section 2.1 becomes somewhat unwieldy and offers little intuition. This Section describes an acoustic transmission-line technique in which each layer of the FBAR is modeled by a network that is derived from the one-dimensional wave equation in the material<sup>1,7,8,9</sup>. Each FBAR layer is modeled by an ABCD matrix, and the admittance of the entire stack is determined from the multiplication of these

matrices. As one would expect, the admittance relationships derived from the transmission-line model reduce to those derived in the previous Section from the differential equations of motion.

As shown in Figure 2.11a, the transmission-line model of a layer is derived from reflected and incident stress and velocity waves subject to boundary conditions at the layer surface<sup>1</sup>.

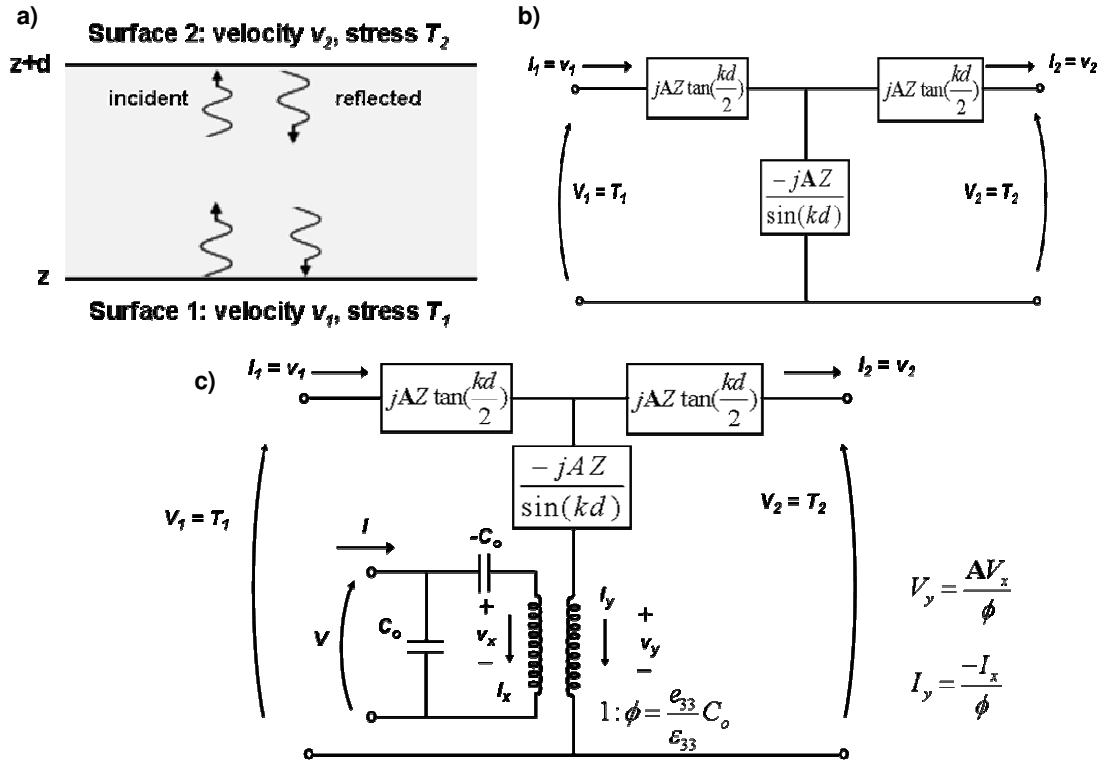


Figure 2.11: (a) The transmission-line model of each layer is derived from reflected and incident stress and velocity waves subject to boundary conditions at the top and bottom surfaces; (b) two-port transmission-line model for a non-piezoelectric layer; (c) three-port transmission line for a piezoelectric layer. In this analysis, acoustic variables for stress ( $T_1$  and  $T_2$ ) and velocity ( $v_1$  and  $v_2$ ) are replaced with acoustic voltages ( $V_1$  and  $V_2$ ) and currents ( $I_1$  and  $I_2$ ). The electrical port to the piezoelectric layer has a true electrical current  $I$  and voltage  $V$ .

The model for a non-piezoelectric layer (Figure 2.11b) is marked by two acoustic ports, where by convention the acoustic stress ( $T_1$  and  $T_2$ ) and velocity ( $v_1$  and  $v_2$ )

are represented by acoustic voltages ( $V_1$  and  $V_2$ ) and currents ( $I_1$  and  $I_2$ ). In the case of a piezoelectric layer (Figure 2.11c), the model consists of two acoustic ports and one electrical port with voltage  $V$  and current  $I$ .

The transformer, with a turns ratio  $\phi$ , converts between the electric and acoustic domains:

$$\phi = \frac{e_{33}}{\epsilon_{33}} C_o \quad \text{Eq. 2.61}$$

Figure 2.11 also states the relationship between acoustic and electrical voltages and currents across the transformer. In the models,  $\mathbf{A}$  is the resonator area,  $k$  is the wavenumber,  $d$  is the layer thickness,  $Z$  is the acoustic impedance (Eq. 2.17), and  $C_o$  is the static capacitance.

To analyze the FBAR of this work, we first seek an ABCD matrix for the AlN and Pt structure of Figure 2.12 that relates the acoustic variables  $V_o$  and  $I_o$  to the electric variables  $I$  and  $V$ :

$$\begin{bmatrix} V \\ I \end{bmatrix} = \begin{bmatrix} A_{AlN,Pt} & B_{AlN,Pt} \\ C_{AlN,Pt} & D_{AlN,Pt} \end{bmatrix} \begin{bmatrix} V_o \\ I_o \end{bmatrix} \quad \text{Eq. 2.62}$$

The matrix coefficients can be determined to be:

$$A_{Al,Pt} = \frac{1}{\phi(a + Z_{Pt})} \left[ (a + b + Z_{Pt})\mathbf{A} - \frac{\phi^2}{j\omega C_o} \right] \quad \text{Eq. 2.63}$$

$$B_{AlN,Pt} = \frac{1}{\phi(Z_{Pt} + a)} \left[ (Z_{Pt} + a)(a + b + ab)\mathbf{A} - \frac{\phi^2}{j\omega C_o} (2a + Z_{Pt}) \right] \quad \text{Eq. 2.64}$$

$$C_{AIN,Pt} = \frac{j\omega C_o A (a + b + Z_{Pt})}{\phi(a + Z_{Pt})} \quad \text{Eq. 2.65}$$

$$D_{AIN,Pt} = \frac{j\omega C_o A}{\phi(Z_{Pt} + a)} [(a + b)(Z_{Pt} + a) + ab] \quad \text{Eq. 2.66}$$

where:

$$a = jZ_{AIN} \tan\left(\frac{k_{AIN} d_{AIN}}{2}\right) \quad \text{Eq. 2.67}$$

$$b = \frac{-jZ_{AIN}}{\sin(k_{AIN} d_{AIN})} \quad \text{Eq. 2.68}$$

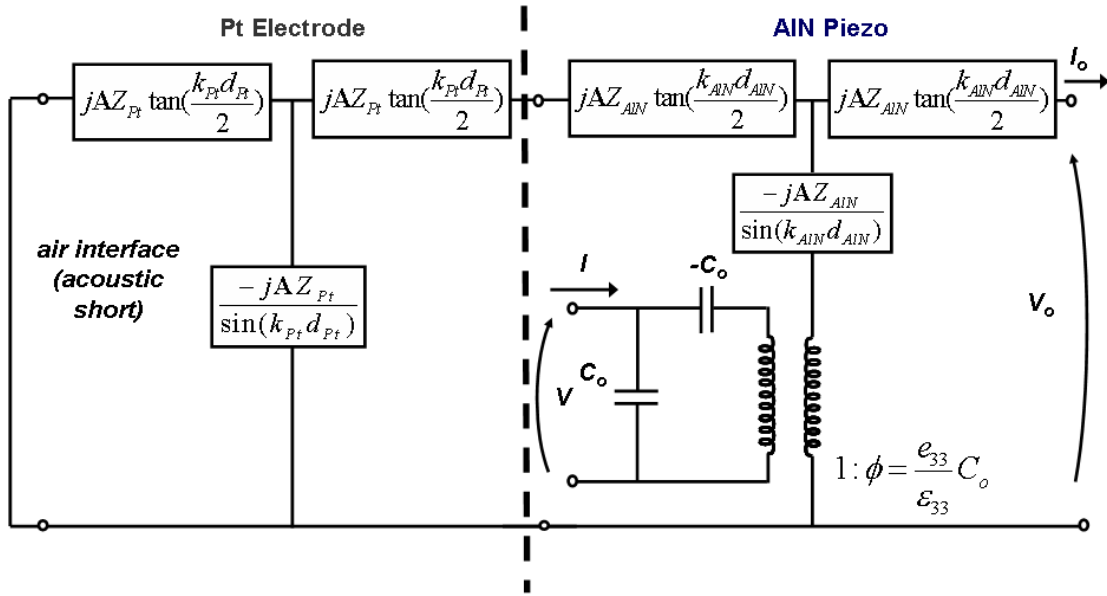


Figure 2.12: Transmission-line model of Pt and AlN layers. The acoustic short at the bottom Pt surface models the air interface (zero stress).

From Eq. 2.62, the electrical impedance at the input of the resonator is:

$$Z_{in} = \frac{V}{I} = \frac{A_{AIN,Pt} Z_o + B_{AIN,Pt}}{C_{AIN,Pt} Z_o + D_{AIN,Pt}} \quad \text{Eq. 2.69}$$

where:

$$Z_o = \frac{V_o}{I_o} \quad \text{Eq. 2.70}$$

As shown in Figure 2.13, the addition of the Al and PM film is modeled by the concatenation of the non-piezoelectric layers to the acoustic port ( $V_o$ ,  $I_o$ ) in Figure 2.12.

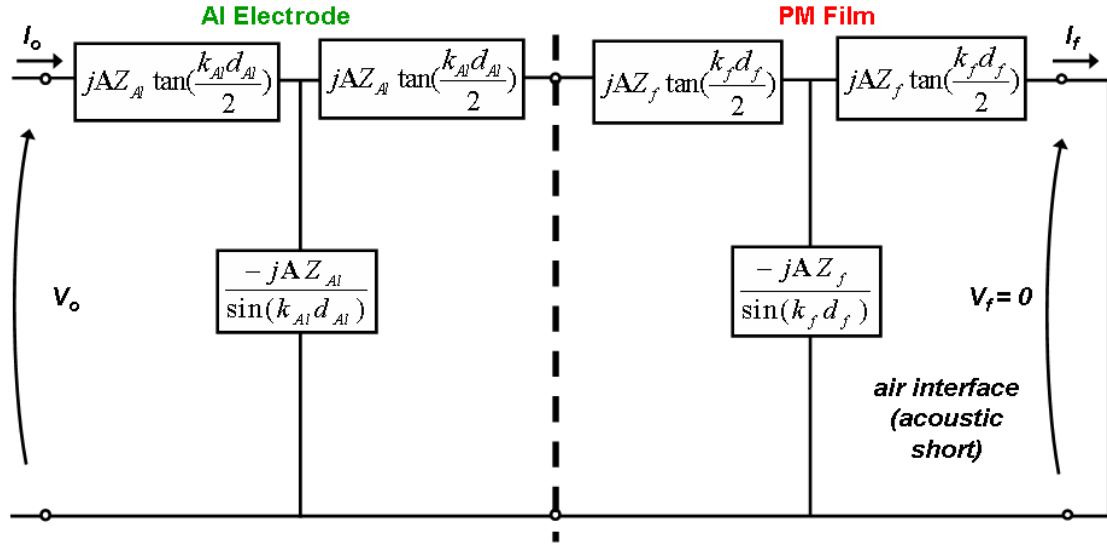


Figure 2.13: Acoustic transmission-line model for Al electrode and PM film.

We can express the acoustic voltage and current at the Al –AlN interface as the multiplication of the ABCD matrix for each layer:

$$\begin{bmatrix} V_o \\ I_o \end{bmatrix} = \begin{bmatrix} A_{Al} & B_{Al} \\ C_{Al} & D_{Al} \end{bmatrix} \begin{bmatrix} A_f & B_f \\ C_f & D_f \end{bmatrix} \begin{bmatrix} V_f \\ I_f \end{bmatrix} \quad \text{Eq. 2.71}$$

At the air-PM film interface,  $V_f = 0$  (zero stress), and the acoustic impedance  $Z_o$  seen looking into the bottom surface of the Al electrode reduces to:

$$Z_o = \frac{V_o}{I_o} = \frac{jZ_{Al} \tan(k_{Al}d_{Al}) + jZ_f \tan(k_f d_f)}{1 - \left(\frac{Z_f}{Z_{Al}}\right) \tan(k_{Al}d_{Al}) \tan(k_f d_f)} \quad \text{Eq. 2.72}$$

For an FBAR with no PM layer ( $d_f = 0$ ), the impedance reduces to  $Z_o = jZ_{Al} \tan(k_{Al}d_{Al})$ . If the Al is acoustically thin, this term reduces to  $j\omega\rho_{Al}d_{Al}$ .

For  $k_{Al}d_{Al} \rightarrow \frac{\pi}{2}$ , the acoustic impedance approaches to infinity asymptotically.

From Eq. 2.47, Eq. 2.69, and Eq. 2.72, the impedance  $Z_m$  of the motional branch of Figure 2.6 is obtained as:

$$Z_m = \frac{A_{AlN,Pt}Z_o + B_{AlN,Pt}}{D_{AlN,Pt} - j\omega C_o B_{AlN,Pt} + Z_o [C_{AlN,Pt} - j\omega C_o A_{AlN,Pt}]} \quad \text{Eq. 2.73}$$

For no Al or PM film ( $Z_o = 0$ ), Eq. 2.73 reduces to Eq. 2.57 as expected. The full FBAR model of Eq. 2.73 including Pt, Al, and PM layers, can now be expressed as the sum of three terms:  $Z_{m_o}$  (Eq. 2.48), which models the intrinsic AlN,  $Z_{m_{Pt}}$  (Eq. 2.57), which accounts for Pt electrode loading, and  $Z_{m_{Al,f}}$ , which accounts for the Al electrode and PM film:

$$Z_{m_{Al,f}} = Z_o \frac{A}{\phi^2} \left[ \frac{1-\xi}{1-2\xi} \right]^2 \quad \text{where } \xi = \frac{Z_{AlN} \tan\left(\frac{k_{AlN}d_{AlN}}{2}\right)}{Z_{Pt} \tan(k_{Pt}d_{Pt})} \quad \text{Eq. 2.74}$$

Using the ABCD transmission-line formulation, Figure 2.14 plots the magnitude and phase of the FBAR admittance subject to loading from Pt and Al (207 nm thick) electrodes and PM (200 nm thick), where  $\rho_{Al} = 2700 \text{ kg / m}^3$ ,  $c_{33Al} = 115 \text{ GPa}$ ,  $\eta_{Al} = 0.03 \text{ kg / s}\cdot\text{m}$ ,  $\rho_f = 800 \text{ kg / m}^3$ ,  $c_{33f} = 10 \text{ GPa}$ , and  $\eta_f = 0.1 \text{ kg / s}\cdot\text{m}$



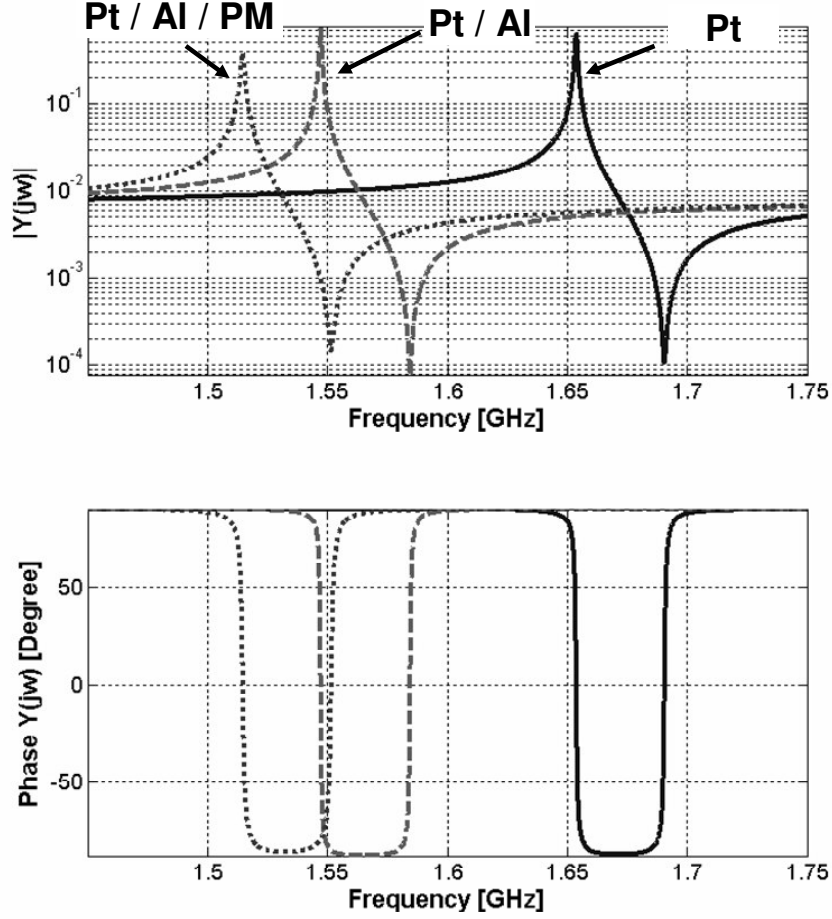


Figure 2.14: Magnitude and phase of admittance calculated from the ABCD transmission-line model of the FBAR. Solid lines corresponds to loading with 340 nm of Pt, the dashed lines loading with Pt and a 207 nm Al electrode, and the dotted lines Pt, Al, and 200 nm of PM.

## 2.3 FBAR Pierce Oscillator Analysis

### 2.3.1 Oscillator Loop Gain Analysis

The FBAR oscillator in the PM mass monitor employs the Pierce topology shown in Figure 2.15a. Transistor M1, DC biased by M3, provides gain to offset crystal and circuit losses. The PMOS load transistor M2 functions as a current source. The oscillator output is buffered with a chain of source followers to prevent loading and to drive off-chip.

The oscillation frequency and startup behavior may be analyzed by considering the loop gain  $T(s)$  of the circuit, given as the product of the forward  $a(s)$  and feedback  $f(s)$  transfer functions<sup>10</sup>:

$$T(s) = a(s)f(s) \quad \text{Eq. 2.75}$$

The characteristic equation  $1 - T(s) = 0$  gives the poles of the closed-loop system.

For oscillator startup, the requirements on loop gain are:

$$\text{Phase}\{T(s)\} = 0^\circ \quad |T(s)| \geq 1 \quad \text{Eq. 2.76}$$

As will be discussed, Eq. 2.76 is a necessary but not a sufficient condition for oscillation<sup>11</sup>. During startup, the circuit exhibits a pair of complex, right-half plane poles close to the imaginary axis with values:

$$s_{1,2} = \sigma \pm j\omega_r \quad \text{Eq. 2.77}$$

In the time domain, these poles give rise to an exponentially growing waveform approximated by:

$$V(t) \cong Ae^{\sigma t} \cos(\omega_r t) \quad \text{Eq. 2.78}$$

As the oscillator amplitude grows, the transistors exhibit non-linear large-signal behavior that limits the signal amplitude and causes the poles to relax to the imaginary axis with  $s = j\omega_r$  and:

$$\text{Phase}\{T(j\omega_r)\} = 0^\circ \quad |T(j\omega_r)| = 1 \quad \text{Eq. 2.79}$$

Figure 2.15b shows the small-signal model of the oscillator. Transistor M1 provides 180° of phase shift while the combination of  $C_1$  and  $C_2$  and the crystal give the additional 180° necessary to sustain oscillation.

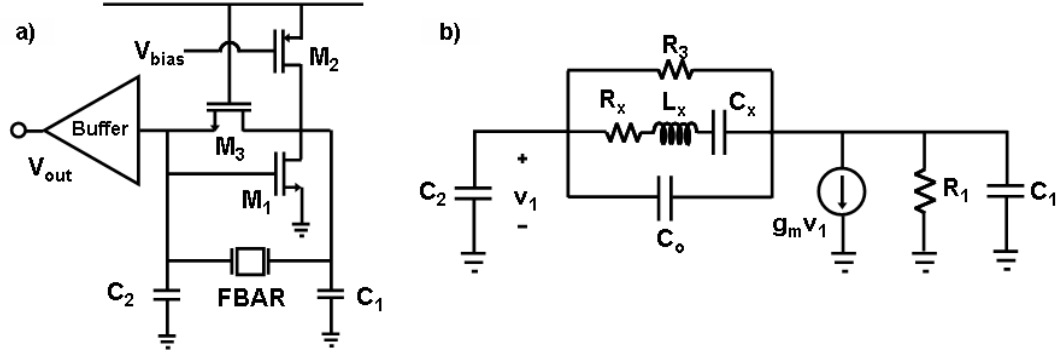


Figure 2.15: (a) FBAR Pierce oscillator; (b) small-signal oscillator model for startup analysis.

Capacitor  $C_2$  includes  $C_{gs}$  of M1, the buffer input capacitance, and other parasitics. Resistor  $R_1 = r_{o1} \parallel r_{o2}$ , and the capacitor  $C_1$  includes the drain capacitances of M1 and M2 and other parasitics. The crystal parameters  $R_x$ ,  $L_x$ , and  $C_x$  can be determined from experimental FBAR measurements or Eq. 2.51, Eq. 2.52, and Eq. 2.53.

The oscillator loop gain is determined by breaking the feedback at the drain of M1, injecting a test current  $i_{test}$ , and estimating the return current in the voltage-controlled current source ( $g_m v_1$ ). Applying this procedure:

$$T(s) = \frac{-g_m v_1}{i_{test}} = \frac{g_m R_1}{s^2 Z_x C_2 C_1 R_1 + s(C_1 R_1 + C_2 R_1 + Z_x C_2) + 1} \quad \text{Eq. 2.80}$$

where

$$Z_x = \frac{s^2 L_x C_x + s C_x R_x + 1}{s^3 L_x C_x C_o + s^2 \left( \frac{L_x C_x}{R_3} + C_o L_x C_x \right) + s \left( \frac{C_x R_x}{R_3} + C_x + C_o \right) + \frac{1}{R_3}} \quad \text{Eq. 2.81}$$

Figure 2.16 shows the magnitude and phase of the loop gain employing the lumped electrical elements for the unloaded FBAR.

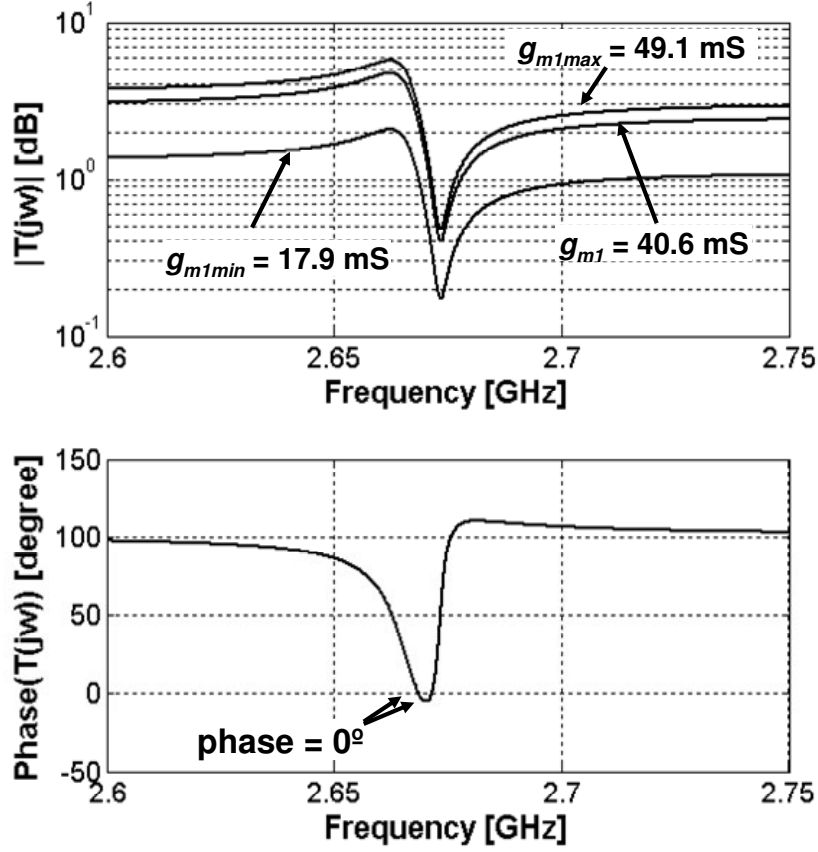


Figure 2.16: Loop gain and phase of a Pierce oscillator employing an unloaded FBAR for several values of  $g_{m1}$ . For  $g_{m1}$  below 17.9 mS and above 49.1 mS, the oscillator exhibits a damped transient response since the circuit poles lie in the left-half plane (see Figure 2.17).

In Figure 2.16, the circuit parameters were those typical of the implemented 0.25  $\mu\text{m}$  CMOS oscillator:  $C_2 = 680$  fF,  $C_1 = 99$  fF,  $g_{m1} = 40.6$  mS, and  $R_3 = 3.8$  k $\Omega$ . The simulation shows that the circuit loop gain satisfies Eq. 2.76 at a frequency of 2.671 GHz.

Figure 2.17 plots the root locus of the loop gain using  $g_{m1}$  as the feedback gain, and Figure 2.18 plots the Nyquist diagram. Recall that the Nyquist criterion for system instability requires  $T(s)$  to encircle the point (-1, 0) in a clockwise direction as  $s$  varies from  $-\infty$  to  $+\infty$ . The Figures indicate that there is a range of

loop gains ( $g_{m1}$ ) for which the circuit will oscillate. For  $g_{m1}$  larger than  $\sim 17.9$  mS, the circuit poles enter the right half-plane indicating oscillator startup. However, for  $g_{m1}$  larger than  $\sim 49.1$  mS, the poles leave the right half plane indicating a damped transient response. In terms of the magnitude and phase of  $Y(j\omega)$ , for large values of  $g_{m1}$  that lead to a damped transient response, as shown in Figure 2.16, the conditions in Eq. 2.76 are met at more than one frequency (the magnitude curve in Figure 2.16 shifts upward as  $g_{m1}$  is increased).

From Figure 2.17b, the oscillator resonant frequency is estimated to be 2.671 GHz. Figure 2.19 is a Spectre circuit simulation confirming the oscillator startup and resonant frequency. Determination of the oscillator frequency and startup behavior will prove useful for the analysis of the effect of PM loading on the FBAR.

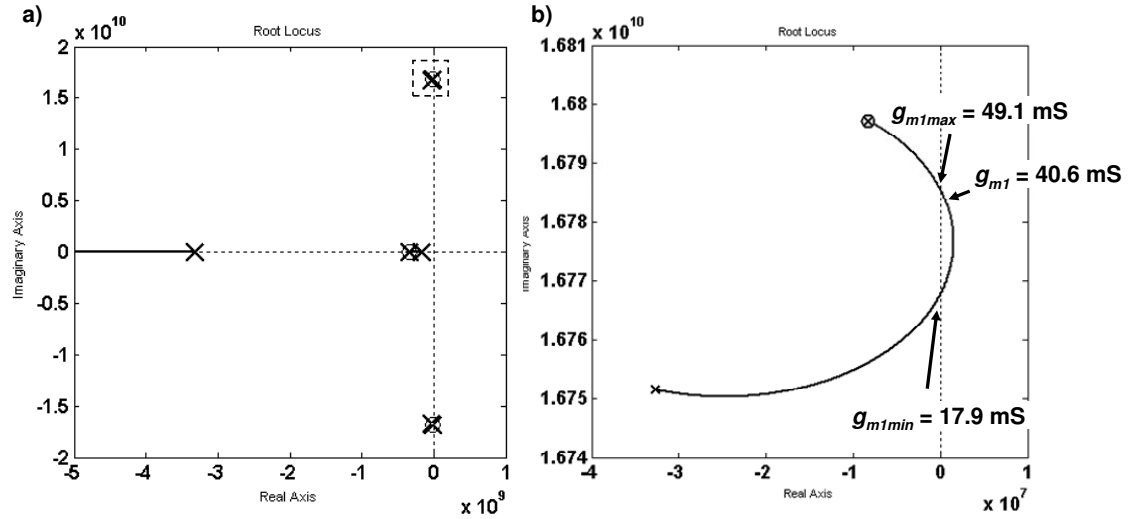


Figure 2.17: (a) Root-locus of loop gain parameterized with feedback gain  $g_{m1}$ ; (b) zoomed view of trajectory of right-half-plane pole in dotted box in part (a). With  $g_{m1} = 40.6$  mS, the oscillation frequency can be estimated from the plot as 2.671 GHz.

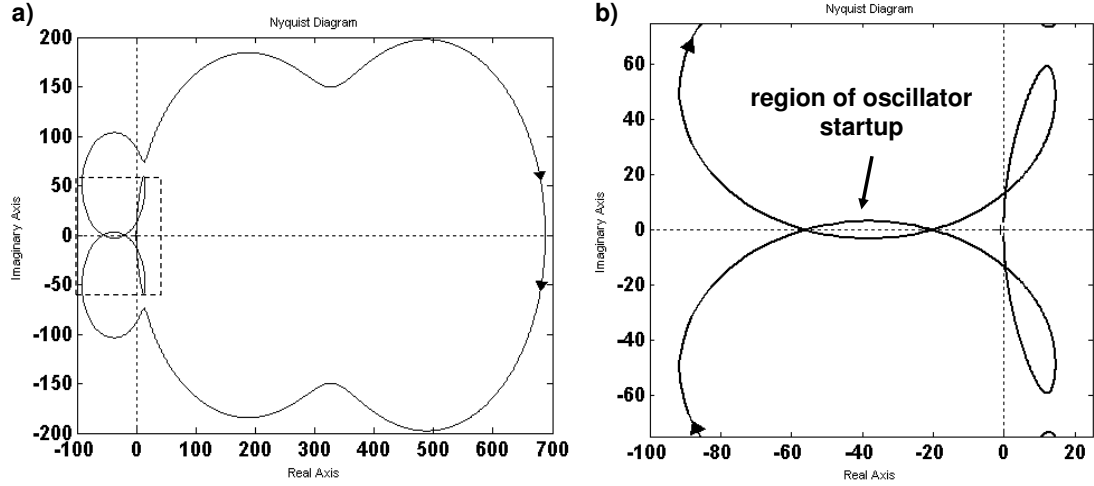


Figure 2.18: (a) Nyquist diagram; (b) zoomed region within dotted box of Figure (a). The region for oscillator startup is evident.

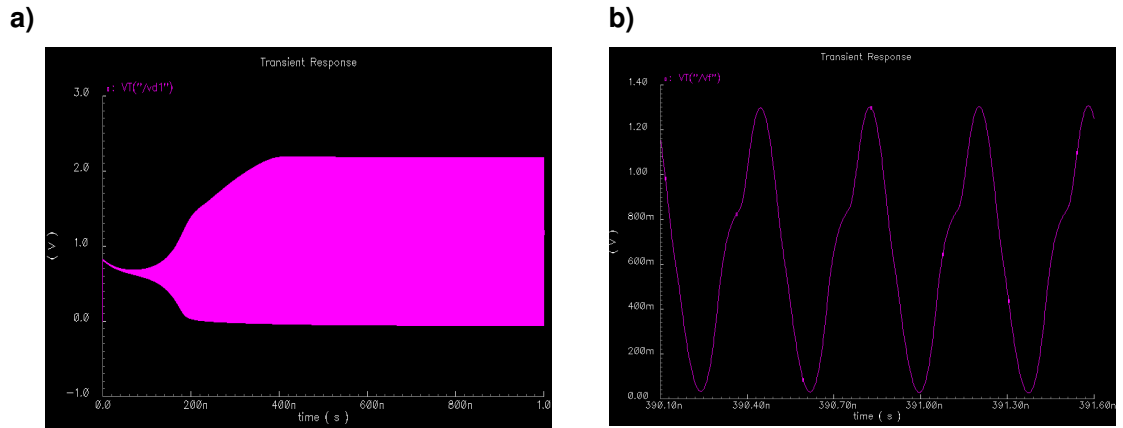


Figure 2.19: Spectre simulation of oscillator startup seen at drain of M1 with  $g_{m1} = 40.6 \text{ mS}$ ; (b) three periods of oscillation with frequency  $2.67 \text{ GHz}$ , as expected.

### 2.3.2 Negative-Resistance Oscillator Model

A second technique to model oscillator startup is the negative-resistance model<sup>11,12</sup>. As shown in Figure 2.20b, the oscillator circuit is separated into a one-port, frequency-determining passive circuit with the complex impedance  $Z_x(j\omega)$ , and a one-port active gain element with impedance  $Z_a(j\omega)$ :

$$Z_a(j\omega) = R_a(j\omega) + X_a(j\omega) \quad \text{Eq. 2.82}$$

$$Z_x(j\omega) = R_x(j\omega) + X_x(j\omega) \quad \text{Eq. 2.83}$$

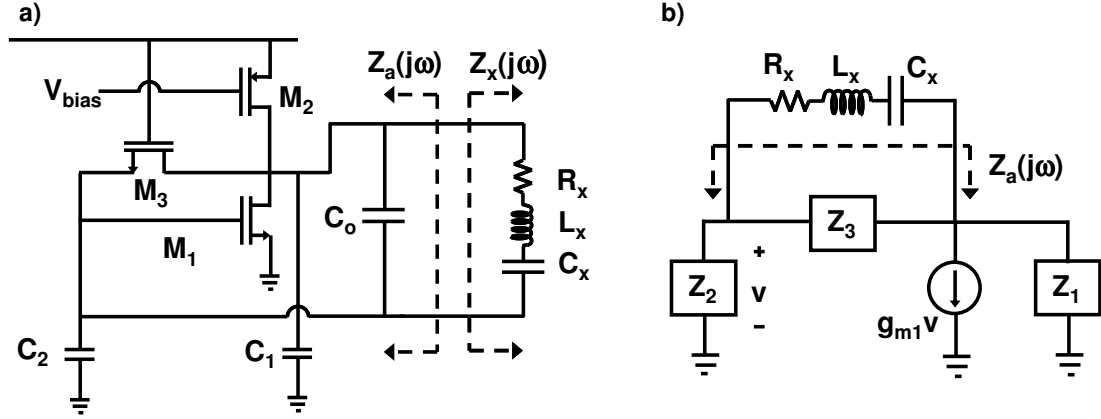


Figure 2.20: (a) Negative-resistance model where the oscillator is separated into a frequency-determining passive circuit with the complex impedance  $Z_x(j\omega)$  and an active gain element with impedance  $Z_a(j\omega)$ ; (b) generalized small-signal model for estimating amplifier negative impedance.

The current through  $Z_x(j\omega)$  is always nearly sinusoidal because of the high-Q series LCR. At steady-state oscillation, the relationship between  $Z_x(j\omega)$  and  $Z_a(j\omega)$  results in a characteristic equation that permits calculation of the resonant frequency  $\omega_r$ :

$$Z_x(j\omega_r) + Z_a(j\omega_r) = 0 \quad \text{Eq. 2.84}$$

It is useful to express the FBAR motional impedance branch in terms of the frequency pulling  $p$ :

$$Z_x \cong R_x + \frac{j2p}{\omega C_x} \quad \text{Eq. 2.85}$$

where  $p$  is defined as

$$p = \frac{\omega - \omega_s}{\omega_s} \quad \text{Eq. 2.86}$$

Considering the real and imaginary impedance components separately, oscillator startup requires:

$$-R_a(j\omega_r) > R_x \quad \text{Eq. 2.87}$$

$$-X_a(j\omega_r) = \frac{2p}{\omega C_x} \quad \text{Eq. 2.88}$$

The exponential time constant for oscillator startup is calculated as<sup>12</sup>:

$$\tau = -\frac{L_x}{R_x + R_a(j\omega_r)} \quad \text{Eq. 2.89}$$

From the generalized small-signal model in Figure 2.20b, the amplifier input impedance is calculated to be:

$$Z_a(j\omega) = \frac{Z_1 Z_3 + Z_2 Z_3 + g_{m1} Z_1 Z_2 Z_3}{Z_1 + Z_2 + Z_3 + g_{m1} Z_1 Z_2} \quad \text{Eq. 2.90}$$

Figure 2.21a plots a simulation of  $-Z_x(j\omega)$  and  $Z_a(j\omega)$ . In the plot of  $-Z_x(j\omega)$ , the frequency is swept from 2 to 3 GHz while in the plot of  $Z_a(j\omega)$ , a resonant frequency of  $\omega_r = 2.671$  GHz is assumed and  $g_{m1}$  is swept from  $-\infty$  to  $+\infty$ . In Figure 2.21b, a magnified view of the region of negative impedance, oscillator startup occurs for values of  $g_{m1}$  satisfying  $-R_a(j\omega) < R_x$ . The range of values of  $g_{m1}$  leading to oscillation agree with the loop gain analysis described earlier. The fastest startup transient corresponds to the maximum negative resistance and for low-power operation, the optimal bias point corresponds to  $g_{m1min}$ .



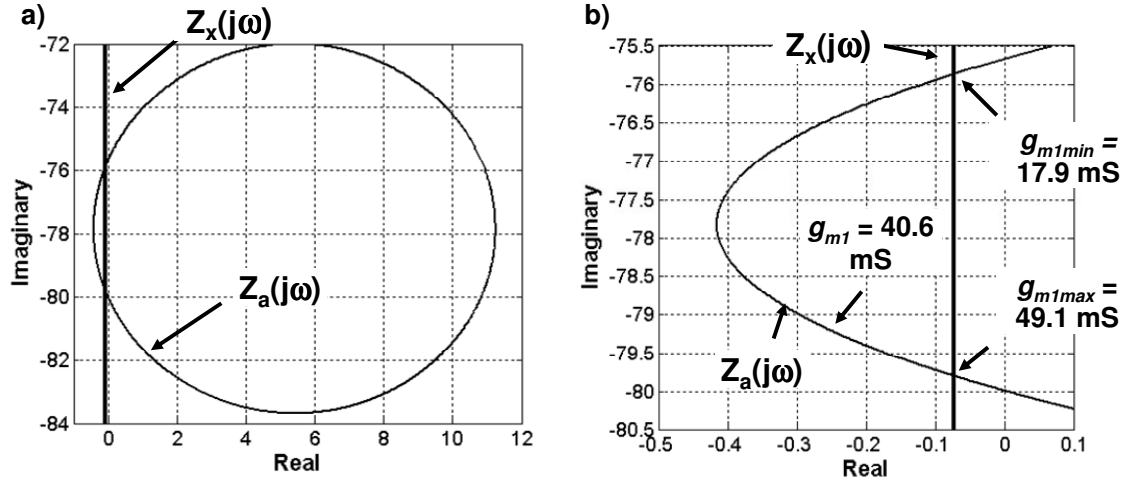


Figure 2.21: (a) Parametric plot of  $Z_a(j\omega)$  and  $-Z_x(j\omega)$ ; (b) magnified view of the region of negative  $Z_a(j\omega)$  where  $-R_a(j\omega) < R_x$ . In the plot of  $Z_x(j\omega)$ , the frequency is swept from 2 to 3 GHz, while in the plot of  $Z_a(j\omega)$  a resonant frequency of  $\omega_r = 2.671 \text{ GHz}$  is assumed and  $g_{m1}$  is swept from  $-\infty$  to  $+\infty$ .

## 2.4 Chapter 2 References

- <sup>1</sup> J.F. Rosenbaum, *Bulk Acoustic Wave Theory and Devices*, Boston: Artech House, 1988.
- <sup>2</sup> S.J. Martin, V.E. Granstaff, and G.C. Frye, "Characterization of a quartz crystal microbalance with simultaneous mass and liquid loading", *Anal.Chem.*, vol. 63, no. 20, pp. 2272-2281, 1991.
- <sup>3</sup> C.E. Reed, K.K. Kanazawa, and J.H. Kaufman, "Physical description of a viscoelastically loaded AT-cut quartz resonator", *J. Appl. Phys.*, vol. 68, no. 5, pp. 1993-2001, 1990.
- <sup>4</sup> E. Benes, "Improved quartz crystal microbalance technique", *J. Appl. Phys.*, vol. 56, no. 3, pp. 608-626, 1984.
- <sup>5</sup> S.J. Martin, V.E. Granstaff, and G.C. Frye, "Characterization of a quartz crystal microbalance with simultaneous mass and liquid loading", *Anal.Chem.*, vol. 63, no. 20, pp. 2272-2281, 1991.
- <sup>6</sup> S.J. Martin and G.C. Frye, "Polymer film characterization using quartz resonators", *Proc. Ultrasonics Symp.*, pp. 393 - 398, 1991.
- <sup>7</sup> V.E. Granstaff and S.J. Martin, "Characterization of a thickness-shear mode quartz resonator with multiple nonpiezoelectric layers", *J. Appl. Phys.*, vol. 75, no. 3, pp. 1319-1329, 1994.

- 
- <sup>8</sup> R.W. Cernosek, S.J. Martin, A.R. Hillman, and H.L. Bandey, "Comparison of lumped-element and transmission-line models for thickness-shear-mode quartz resonator sensors", *IEEE Trans. Ultrasonics, Ferroelectrics, and Frequency Control*, vol. 45, no. 5, pp. 1399-1407, 1998.
- <sup>9</sup> R. Krimholtz, D.A. Leedom, and G.L. Matthaei, "New equivalent circuits for elementary piezoelectric transducers", *Electronics Lett.*, vol. 6, no. 13, pp. 389-390, 1970.
- <sup>10</sup> M.A. Unkrich and R.G. Meyer, "Conditions for startup in crystal oscillators", *IEEE J. Solid-State Circ.*, vol. SC-17, no. 1, pp. 87-90, 1982.
- <sup>11</sup> N.M. Nguyen and R.G. Meyer, "Startup and frequency stability in high-frequency oscillators", *IEEE J. Solid-State Circ.*, vol. 27, no. 5, pp. 810-820, 1992.
- <sup>12</sup> E.A. Vittoz, M.G.R. Degrauwe, and S. Bitz, "High-performance crystal oscillator circuits: theory and application", *IEEE J. Solid-State Circ.*, vol. 23, no. 3, pp. 774-783, 1988.

### **3 Fabrication and Characterization of MEMS PM Components**

This chapter describes the fabrication and characterization of three key elements of the MEMS PM monitor – the FBARs, the Pierce oscillator, and the thermal precipitator. First, after a brief review of their fabrication processes, the measured and theoretical admittances of the ZnO and AlN FBARs are compared. Optical interferometer images of the mode shape of a ZnO FBAR are subsequently presented, followed by the description of a novel atomic force microscope (AFM) resonator imaging technique. Calibration of the FBAR mass sensitivity is summarized and several prototype MEMS PM FBAR oscillators are analyzed. The chapter concludes with a description of the quartz-polysilicon heater.

#### **3.1 FBAR Microfabrication**

##### **3.1.1 ZnO FBAR Process Flow**

During the initial stages of the MEMS PM project, a ZnO FBAR was employed in a number of experiments. The bulk-micromachined device consisted of a ZnO film sandwiched between a Au / Cr bottom electrode and a top Al electrode. Figure 3.1 shows a top view and cross-section of the FBAR at an intermediate microfabrication step and upon completion.

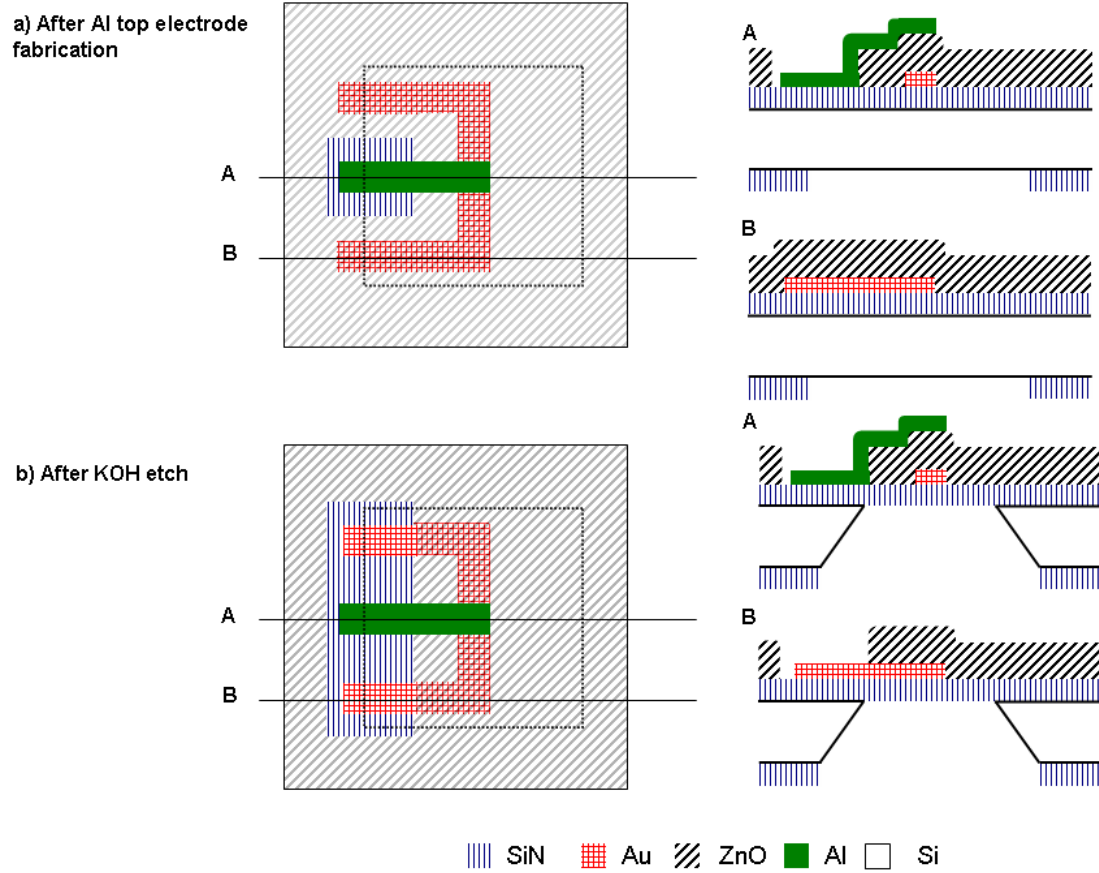


Figure 3.1: Top view and cross-section of ZnO FBAR (a) after deposition and patterning of top Al electrode; (b) after KOH etch of Si substrate.

The ZnO FBAR process flow consisted of the steps outlined below, all of which were performed in the UC Berkeley Microfabrication Facility. All lithography was performed with the KS-aligner using contact printing.

- 1) **Silicon Nitride Membrane Definition:** LPCVD (tylan 18 furnace) 500 nm of low-stress silicon nitride (SiN) on double-polished Si wafers and pattern backside photoresist mask. Plasma etch ( $\text{SF}_6$ , technics-c) backside windows into the SiN for the bulk-Si KOH etch.

- 2) **Gold Ground Electrode Deposition and Patterning:** Evaporate chrome seed layer and 300 nm of Au (v-401 evaporator). Pattern i-line photoresist etch mask and etch Au/Cr with standard chrome and gold wet etchants.
- 3) **Piezoelectric ZnO Layer Deposition and Patterning:** RF-Magnetron sputter 1.2  $\mu\text{m}$  of ZnO (MRC-8600), pattern I-line photoresist mask and wet etch ZnO in  $\text{H}_3\text{PO}_4 : \text{CH}_3\text{COOH} : \text{H}_2\text{O}$  in a 25 ml : 25 ml : 1000 mL ratio (etches  $\sim 1 \mu\text{m}$  per minute). The purpose of this ZnO etch is to expose a SiN region for the signal bond pad and eliminate the step height between signal and ground lines.
- 4) **Aluminum Electrode Definition (Figure 3.1a):** Sputter 300 nm of aluminum (cpa sputterer), pattern g-line photoresist (i-line developer attacks Al), and etch aluminum with  $\text{KFeCN}_6 : \text{KOH} : \text{H}_2\text{O}$  in a 50 g : 5 g : 500 mL ratio. The etch time is less than one minute and the solution does not attack ZnO.
- 5) **Second ZnO Etch:** Pattern g-line photoresist mask, etch ZnO in  $\text{H}_3\text{PO}_4 : \text{CH}_3\text{COOH} : \text{H}_2\text{O}$  in a 25 ml : 25 ml : 1000 mL ratio to expose ground Au electrodes. The solution does not attack Au.
- 6) **KOH Membrane Release (Figure 3.1b):** Heat wafer to 150  $^\circ\text{C}$ , melt and smooth a 5 mm thick layer of Crystal Bond wax onto the front side of the wafer. Attach glass cover to wax, wrap edges with Teflon tape and secure in KOH-etch jig by hand-tightening PVC bolts. Etch in KOH for 7-8 hours to release membranes. To prevent the accumulation of bubbles on the wafer surface, ensure that the jig lies flat on the bottom of the tank with etched side facing up. Dissolve wax in acetone.

Figure 3.2 shows SEMs of two-port ZnO FBARs with (a) a circular and (b) pentagonal shaped electrodes. The active region of each FBAR coincides with the overlap of the Al and Au electrodes. During sputter deposition of the ZnO, an unexpected reaction with the underlying Au occurred, introducing significant undesired resistance in series with the FBAR. The interconnect parasitics precluded use of the ZnO FBAR as the feedback element of an oscillator. As described below, because of the availability of a robust AlN FBAR process and commercial grade deposition tool, the ZnO FBAR efforts ceased after several initial experiments.

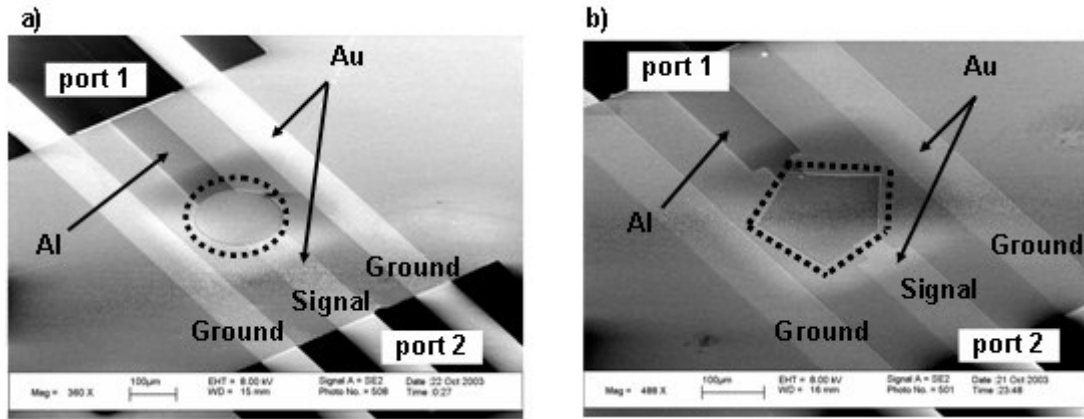


*Figure 3.2: (a) SEM of two-port circular FBAR; (b) SEM of two-port pentagonal FBAR. The active FBAR area coincides with the overlap of the Au and Al electrodes. In both SEMs, the active FBAR area is outlined with the dotted black line.*

### 3.1.2 AlN FBAR Process Flow

During the early stages of this project, the UC Berkeley Microfabrication Facility acquired a state-of-the-art reactive-ion AlN sputtering tool from Advanced Modular Sputtering Inc. (Goleta, CA). For purposes of producing an acoustic mass sensor, AlN offered several advantages over ZnO:

- AlN is more chemically inert than ZnO and is thus less susceptible to environmental contaminants;
- the temperature coefficient of frequency of an AlN FBAR is -25 ppm/ °C as compared to -48 ppm/ °C for a ZnO device, resulting in a more stable frequency baseline; and,
- a robust manufacturing process for AlN resonators had been develop in the UC Berkeley Microfabrication Facility which could be readily adapted for fabrication of FBAR mass sensors.

The adopted AlN FBAR process was based on a process flow developed by Gianluca Piazza<sup>1</sup>. The five-mask process consisted of the steps outlined below, where all lithographic steps were performed in the Gcaws2 wafer stepper. Figure 3.3 shows the top view and cross-section of an AlN FBAR.

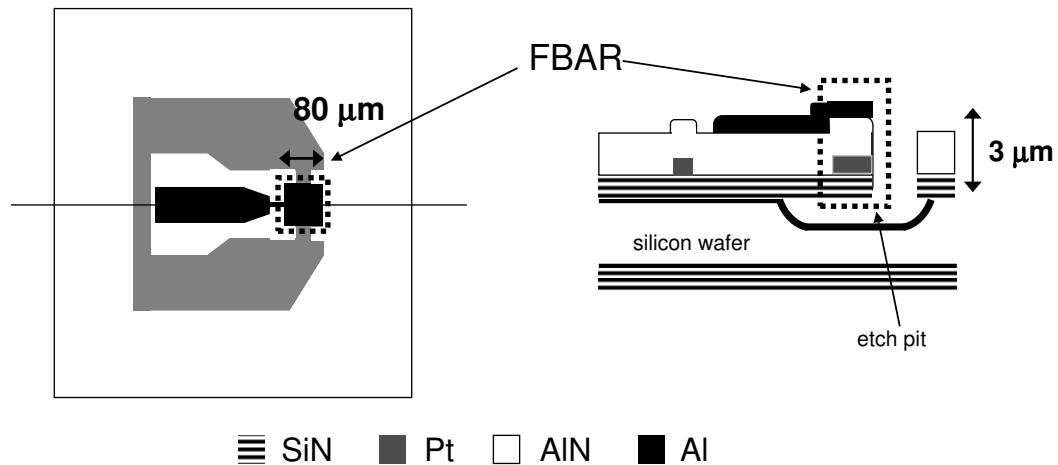


*Figure 3.3: Top-view and cross section of FBAR geometry and material stack. The active FBAR area is located where the Al and Pt electrodes overlap.*

- 1) **Silicon Nitride Dielectric:** LPCVD (tylan 18 furnace) 800 nm of low-stress silicon nitride on high-resistivity Si wafer. The deposition rate is ~ 39 nm / minute for recipe STDLSN.
- 2) **Bottom Pt Electrode:** Using lift-off with 8-10  $\mu\text{m}$  thick g-line photoresist (deposited as several layers), sputter 300 nm of Pt (randex sputterer, 115 sccm Ar at 100 W). Soak wafer upside down in acetone overnight and release in ultrasonic bath. To reduce the resistance, in some designs the Pt interconnect leading up the active FBAR area was thickened to 700 nm with an additional Pt liftoff deposition. In order to prevent acoustic loading, no additional Pt was added to the active FBAR area.
- 3) **AlN Deposition:** Reactive sputter 2  $\mu\text{m}$  of AlN in AMS sputtering tool.
- 4) **Al Top Electrode:** Sputter 200 nm of Al for top electrode and 20-30 nm of niobium (gartek sputterer). Pattern 1.3  $\mu\text{m}$  g-line photoresist mask (harden in oven at 120 °C for six hours) and plasma etch Al / Nb (lam3 etcher, etch rate ~ 600 nm / min, include 5 – 10 second overetch). Strip resist in O<sub>2</sub> plasma (technics-c etcher).
- 5) **Bottom Electrode Vias:** Using a hard-baked (120 °C at 1 hour) 2  $\mu\text{m}$  photoresist mask, etch vias to the ground Pt electrode with hot phosphoric acid (sink7). At a bath temperature of 160 °C, 2  $\mu\text{m}$  of AlN is etched in about 60 seconds.
- 6) **SiO<sub>2</sub> Etch Mask:** Deposit 1.5  $\mu\text{m}$  of SiO<sub>2</sub> at 400 °C (tylan 12 furnace) for hard AlN etch mask.



- 7) **AlN Structure Definition:** Pattern 2  $\mu\text{m}$  thick PR mask that defines the in-plane AlN structure (hardbake resist at 120 °C for 6 hours). Plasma etch  $\text{SiO}_2$  (lam2 etcher, standard  $\text{SiO}_2$  monitor recipe, etch rate of  $\sim 500 \text{ nm} / \text{min}$ , include 20 second overetch), and dry etch AlN by modifying standard Al etch recipe (lam3 etcher, set  $\text{Cl}_2$  flow to 60 sccm and  $\text{N}_2$  flow to zero, skip airlock process, include 1 to 2 minute overetch, AlN etch rate is  $\sim 150 \text{ nm} / \text{min}$ ). Etch silicon nitride and remove residual oxide (lam2 etcher,  $\text{SiO}_2$  monitor recipe, silicon nitride etch rate  $\sim 500 \text{ nm} / \text{min}$ , include 10 to 20 second overetch).
- 8) **Dicing and Release:** Dice wafers in Disco SAW and dry-release in  $\text{XeF}_2$  to remove underlying Si and remove the silicon nitride (xetch etcher, 45 – 60 cycles is typical).

Figure 3.4 shows SEMs of two, one-port AlN FBAR designs. The active FBAR region coincides with the overlap of the Pt and Al electrodes. The AlN FBARs with thick Pt electrodes typically had a fundamental resonance of  $\sim 1.6$  GHz and the best designs exhibited series quality factors ( $Q_s$ ) of over 2000 with motional resistances ( $R_x$ ) less than  $2\ \Omega$ .

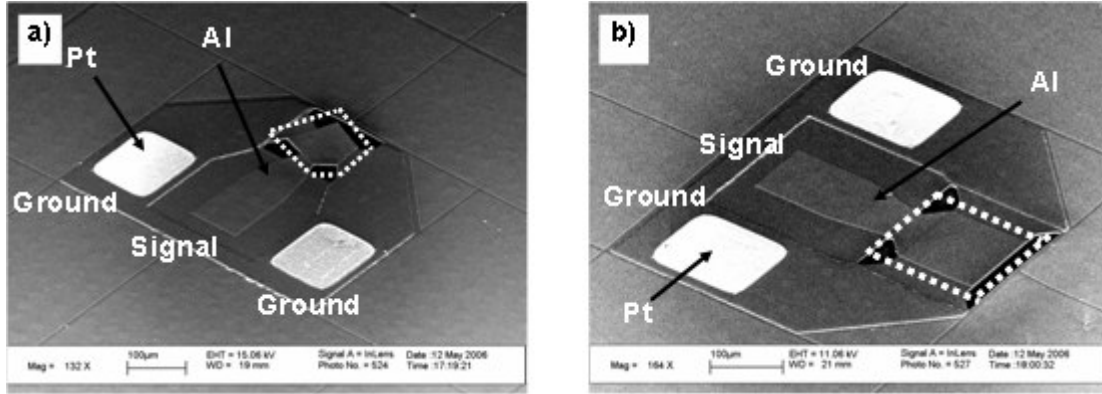


Figure 3.4: (a) SEM of pentagonal AlN FBAR; (b) SEM of square AlN FBAR. The active FBAR coincides with the overlap of the Pt and Al electrodes. In both SEMs, the active FBAR area is outlined with the dotted white line.

## 3.2 FBAR Electrical Characterization

### 3.2.1 ZnO FBAR Impedance

This section compares the simulated (ABCD matrix formulation) and measured impedances of a  $300\ \mu\text{m}$  wide square ZnO FBAR whose CAD layout is given in Figure 3.5a. As shown in the resonator model of Figure 3.5b, the resonator interconnect was found to introduce significant inductive, capacitive, and resistive parasitics to the device electrical response. The resistance originated during deposition from the reaction between the sputtered ZnO and the Au bottom electrode. The capacitance arose from the use of low-resistivity silicon wafers and the inductance from the coplanar nature of the signal and ground lines. The

parasitic lumped element values were fit numerically to the measured resonator admittance.

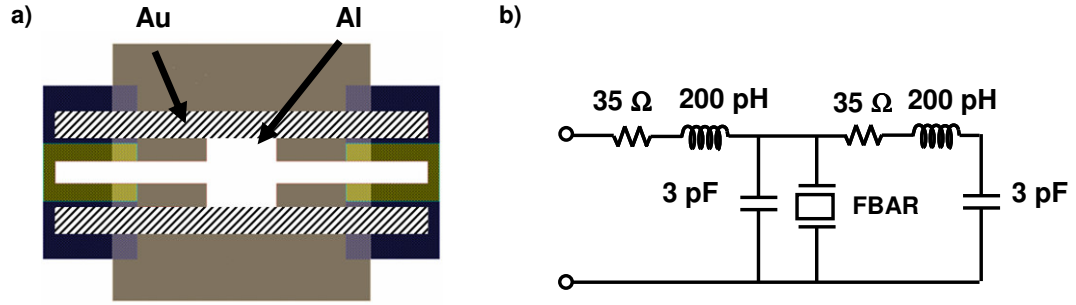


Figure 3.5: (a) Cadence layout of square one-port FBAR 300  $\mu\text{m}$  on a side; (b) electrical model of interconnect to account for electrode resistance from the ZnO-Au reaction, parasitic capacitance from the low-resistivity substrate, and lead inductance from the coplanar signal and ground lines.

Figure 3.6 compares the magnitude and phase of the measured and simulated (ABCD matrix formulation) impedances of the 300  $\mu\text{m}$  wide square FBAR. The simulated impedance includes the parasitic elements shown in Figure 3.5b. The phase offset error between the measured and theoretical value is believed to arise from the lumped approximation for the electrode interconnect.

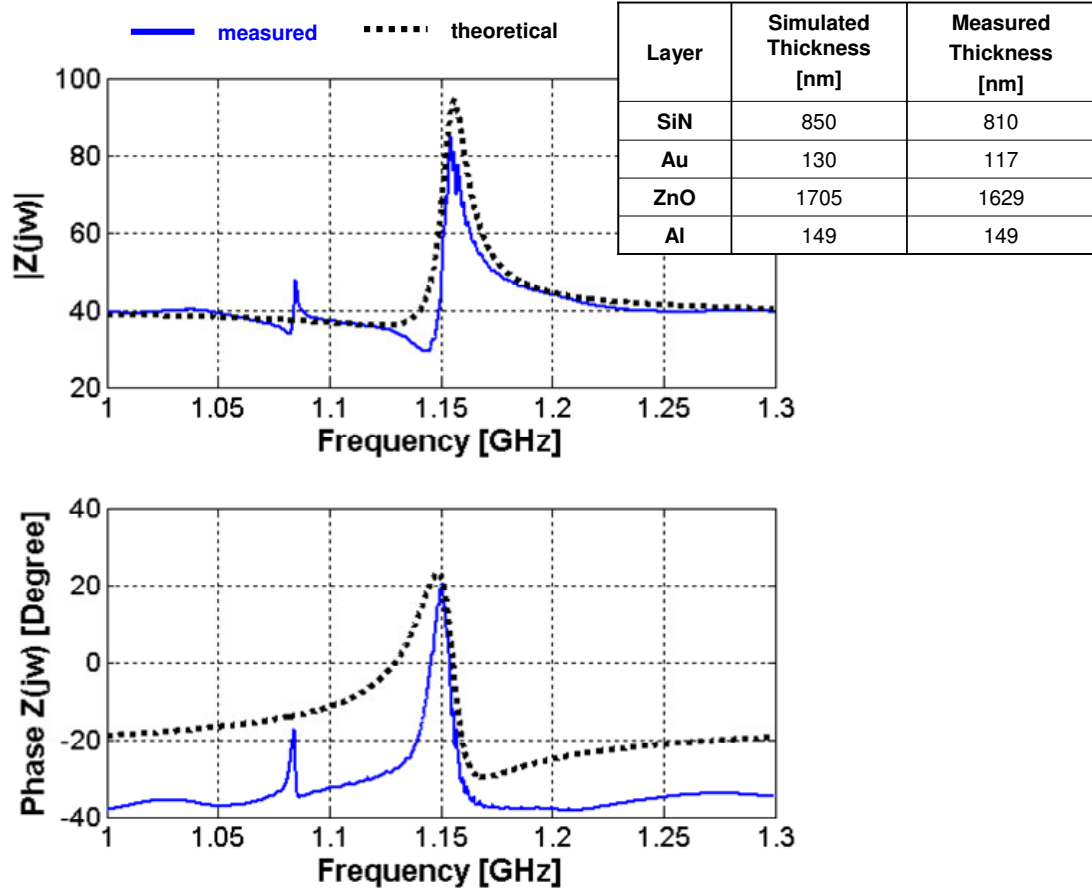


Figure 3.6: Magnitude and phase of measured and simulated (ABCD matrix formulation) impedances of square ZnO FBAR 300  $\mu\text{m}$  on a side. The simulated impedance includes the parasitic elements shown in Figure 3.5b. Inset shows the measured and simulated layer thicknesses.

### 3.2.2 AlN FBAR Impedance

Figure 3.7 compares the simulated (ABCD matrix formulation) and measured impedances of the first and second harmonics for the 100  $\mu\text{m}$  wide square FBAR shown in the inset of the figure. The measured series quality factor is 1010 and the motional resistance ( $R_x$ ) is 5.4  $\Omega$ .

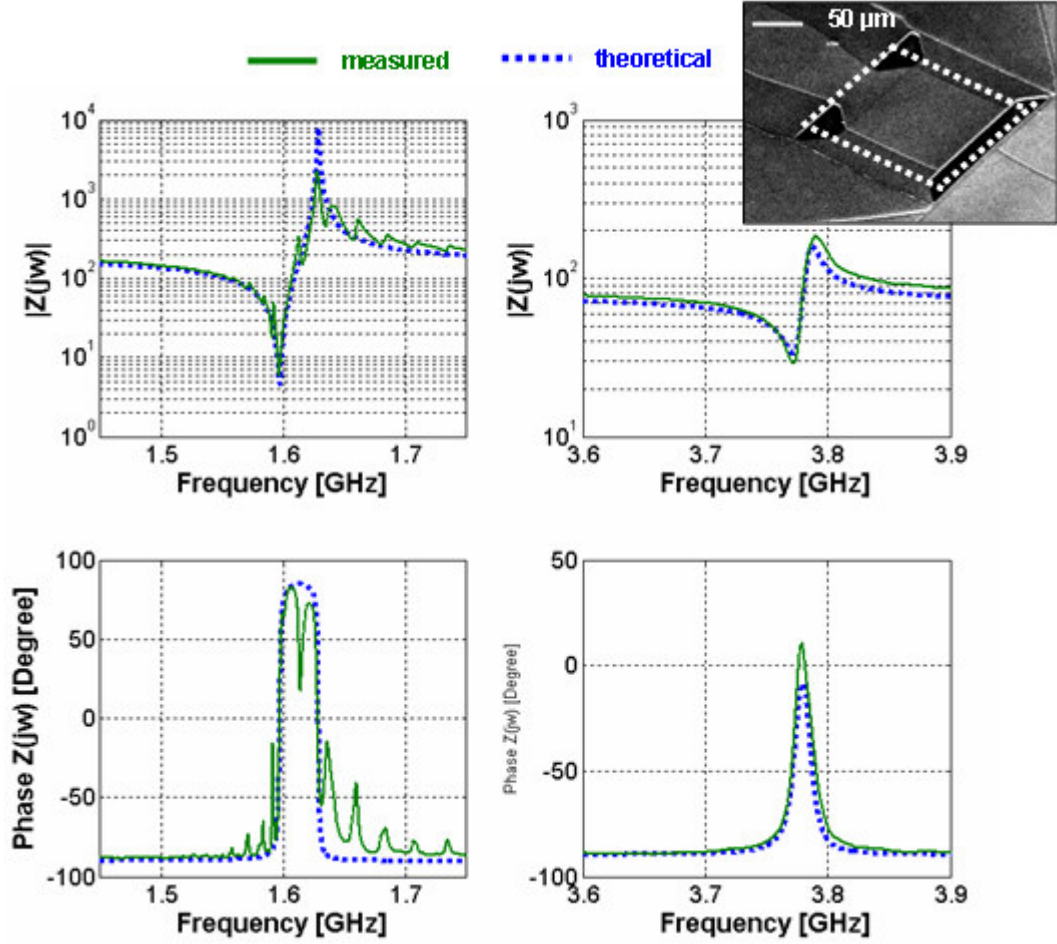


Figure 3.7: Magnitude and phase of the simulated (ABCD matrix formulation) and measured impedances of the 100  $\mu\text{m}$  wide square FBAR shown in the inset (the active FBAR area is outlined with the dotted white line). Responses are given for the fundamental and the second harmonic.

Figure 3.8 compares the simulated (ABCD matrix formulation) and measured impedances of the fundamental and second harmonics for the pentagonal FBAR shown in the figure inset. The measured series quality factor is 924 and the motional resistance ( $R_x$ ) is 3.7  $\Omega$ .

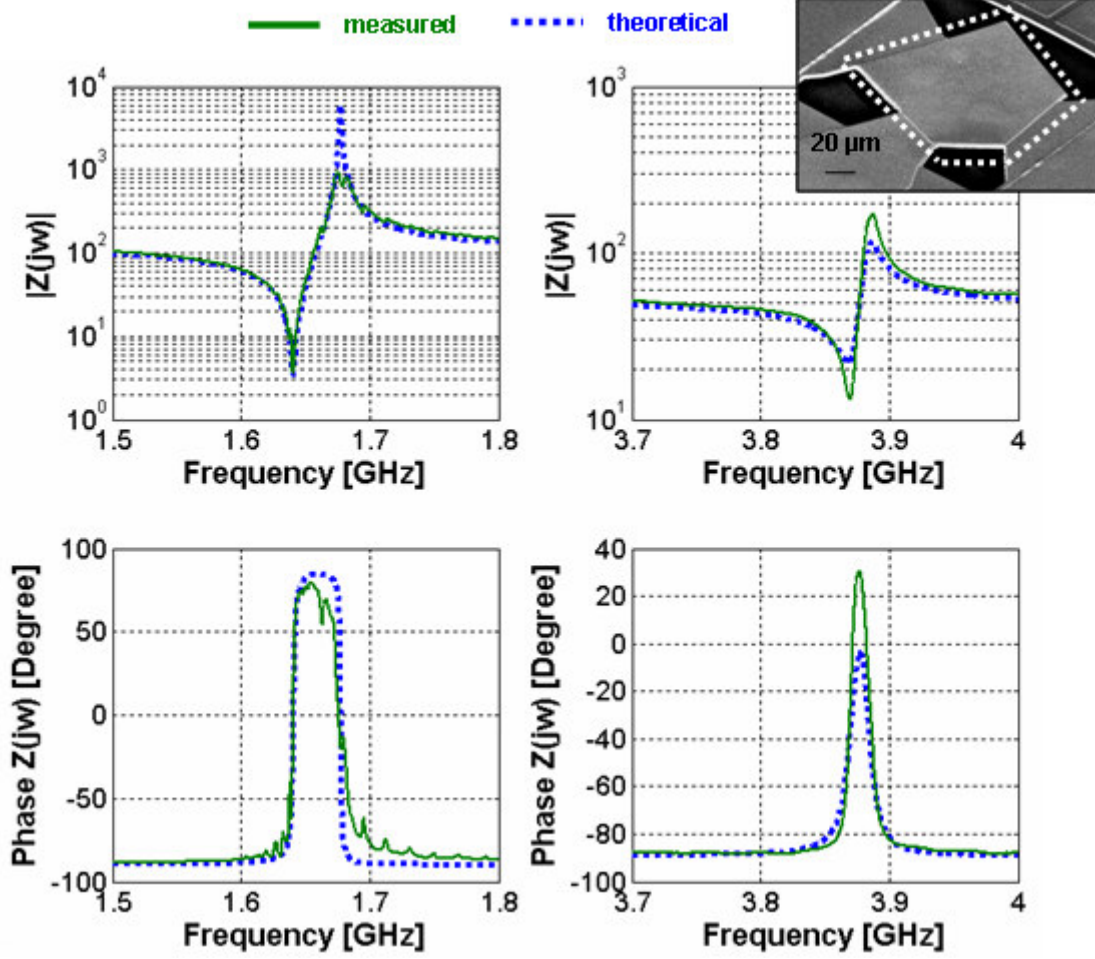


Figure 3.8: Magnitude and phase of the simulated (ABCD matrix formulation) and measured impedances of the pentagonal FBAR shown in the inset (the active FBAR area is outlined with the dotted white line). Responses are given for the first and second harmonics.

Good agreement is evident between the measured and ABCD matrix simulated results, though the square FBAR exhibits a number of parasitic resonances and the measured impedance of the parallel resonance is lower than the simulated value. The parasitic resonances arise from standing Lamb waves and, as widely reported in the literature<sup>2</sup>, can be reduced by eliminating in-plane parallel FBAR edges. The error in the vicinity of the parallel resonance is attributed to dielectric and substrate losses omitted from the resonator model. Table 3.1 shows

good agreement between the measured and simulated thicknesses of each FBAR layer.

Table 3.2 contains the numerically extracted lumped element values for the two FBAR topologies, and Figure 3.9 compares the magnitude and phase of the measured impedances and those calculated from the lumped LCR model. Recall that the lumped LCR elements can not be directly extracted from the layer thicknesses because of the acoustically thick Pt electrode.

*Table 3.1: Comparison of measured and simulated FBAR layer thicknesses.*

Layer	Square 100 $\mu\text{m}$ Wide FBAR		Pentagonal FBAR	
	Measured Thickness [ $\mu\text{m}$ ]	Simulated Thickness [ $\mu\text{m}$ ]	Measured Thickness [ $\mu\text{m}$ ]	Simulated Thickness [ $\mu\text{m}$ ]
<b>Pt</b>	0.36	0.34	0.36	0.34
<b>AlN</b>	1.75	1.91	1.75	1.84
<b>Al</b>	0.23	0.21	0.23	0.21

*Table 3.2: FBAR lumped element models numerically extracted from measured impedances.*

	Square 100 $\mu\text{m}$ Wide FBAR	Pentagonal FBAR
$R_x$ [ $\Omega$ ]	6.0	3.6
$L_x$ [nH]	432.0	257.9
$C_x$ [fF]	23.1	36.5
$C_o$ [pF]	0.54	0.79

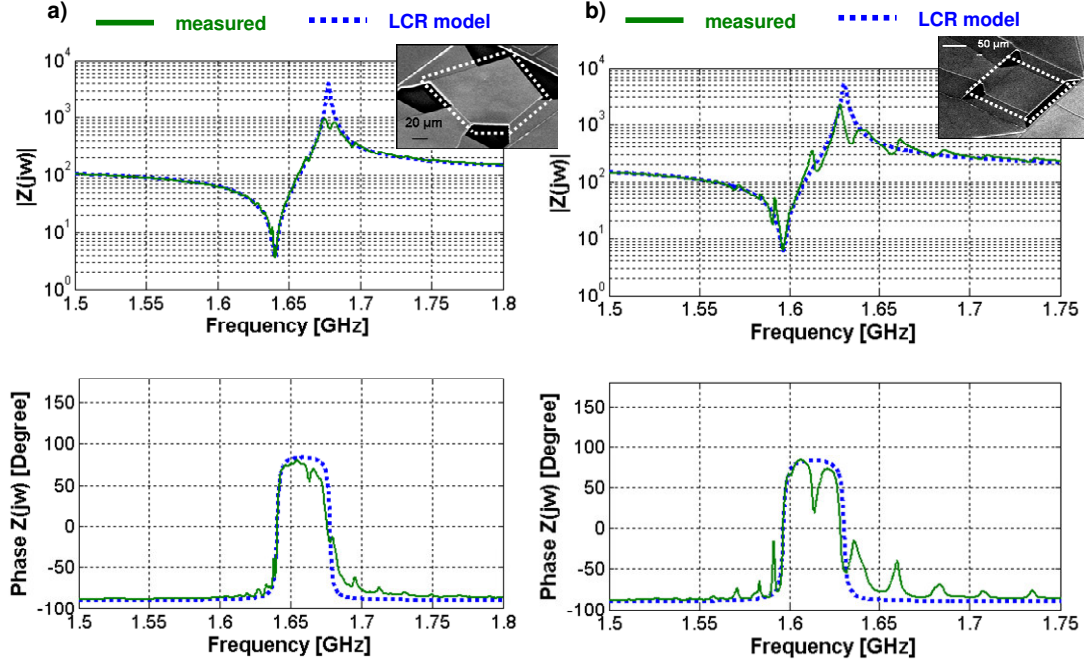


Figure 3.9: (a) Magnitude and phase of pentagonal FBAR impedance as measured and as calculated using the fitted lumped LCR elements of Table 3.2; (b) Magnitude and phase of 100  $\mu\text{m}$  wide square FBAR impedance as measured and as calculated using the fitted lumped LCR elements of Table 3.2.

### 3.3 Calibration of ZnO FBAR Mass Sensitivity with Al Loading

The mass sensitivity of a pentagonal ZnO FBAR was estimated by evaporating a measured amount of Al onto the top electrode and monitoring the corresponding resonant frequency. Figure 3.10 plots the frequency shift as a function of the added Al thickness. Each data point represents the average of two FBARs. Two reference FBARs (no added Al) were measured after each deposition to normalize for factors such as temperature and probe station setup. Good agreement is evident between the theoretical ABCD matrix formulation and the measured data points. Though appearing linear, the ABCD matrix formulation plot has a very small positive curvature.



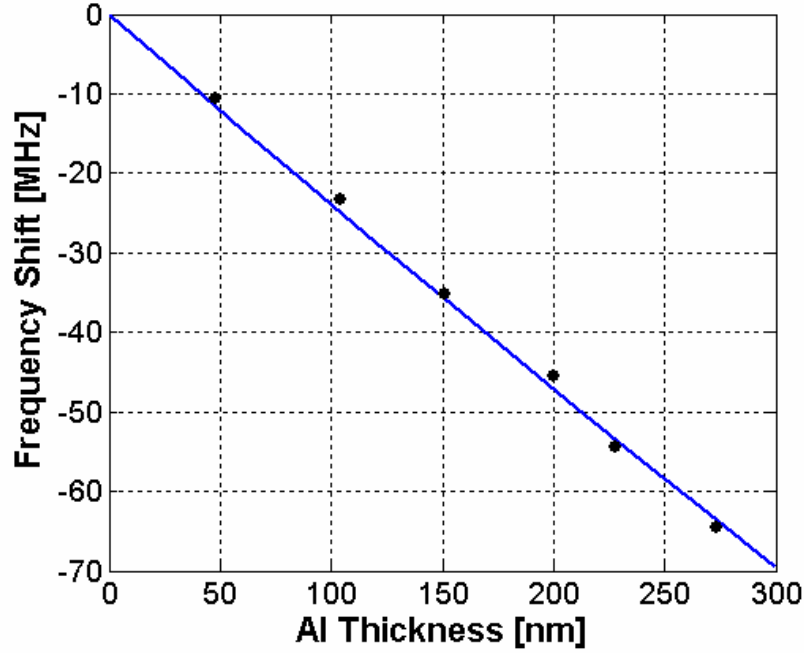


Figure 3.10: Measured (dots) and theoretical (ABCD matrix formulation - solid line) frequency shift of pentagonal ZnO FBAR as a function of added Al electrode thickness. The active FBAR area was  $\sim 24390 \mu\text{m}^2$ .

For the FBAR of Figure 3.10, the observed slope of  $-0.234 \text{ MHz / nm}$  corresponds to a frequency shift of  $-3.56 \text{ kHz / pg}$  for a uniformly distributed added mass. One can relate the added mass per unit area ( $\Delta m'$ ) to the fractional change in frequency  $\frac{\Delta f}{f_o}$  with the Sauerbrey equation:

$$\frac{\Delta f}{f} = \frac{\Delta m'}{m'} = -S_m \Delta m' \quad \text{Eq. 3.1}$$

The initial FBAR series resonant frequency was  $1.164 \text{ GHz}$ , which, with the data of Figure 3.10, gives a value for the mass sensitivity  $S_m$  of  $745 \text{ cm}^2 / \text{g}$ . From the ZnO layer thicknesses and densities, one calculates the FBAR mass sensitivity  $S_m$  to be  $694 \text{ cm}^2 / \text{g}$ .

### 3.4 ZnO FBAR Imaging with Optical Interferometry

Xuchun (“Bert”) Liu imaged the ZnO FBAR using his scanning laser Michelson interferometer setup<sup>3,4,5</sup>. As shown in Figure 3.11, the laser beam, a linearly polarized TEM<sub>00</sub>-mode 25 mW HeNe laser ( $\lambda = 632.8$  nm), is expanded, collimated, and spatially filtered by a Galilean telescope and a pinhole. The measurement beam is focused with a lens onto the top electrode of the resonator. The beam spot size, about 1  $\mu\text{m}$  in diameter, sets the lateral resolution of the image. To scan the sample underneath the focusing lens, the resonator is secured to a three-axis stage that has a displacement step size of 50 nm. In order to maintain peak interferometer sensitivity, a feedback signal modulates the position of the reference mirror.

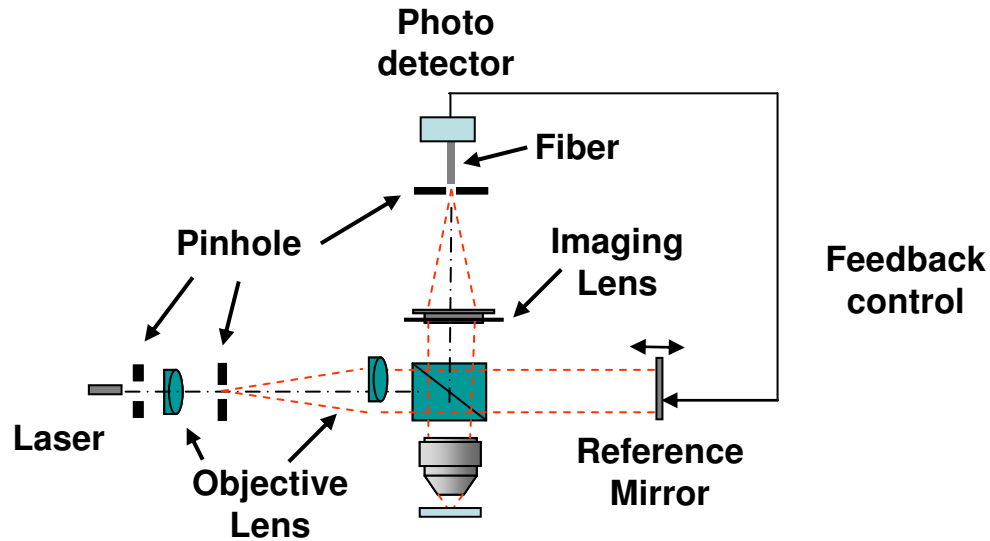


Figure 3.11: Scanning laser interferometer with feedback control<sup>3</sup>.

Figure 3.12a is an SEM of the ZnO FBAR under test, and Figure 3.12b shows the S11 reflection coefficient of the device operating with an input power of +10 dBm. The series resonant frequency is 1.077 GHz and the measured peak

amplitude was about 5 nm. Figure 3.13 shows eight frames of the FBAR mode shape at 1.077 GHz. The frame number is designated by index “ $i$ ”, where a full period of motion consisted of thirty frames, and the corresponding resonator phase equals  $2\pi i / 30$ . Since the ZnO film is present over the entire membrane except in the vicinity of the GSG (ground-signal-ground) pads, the FBAR edges are rigidly clamped.

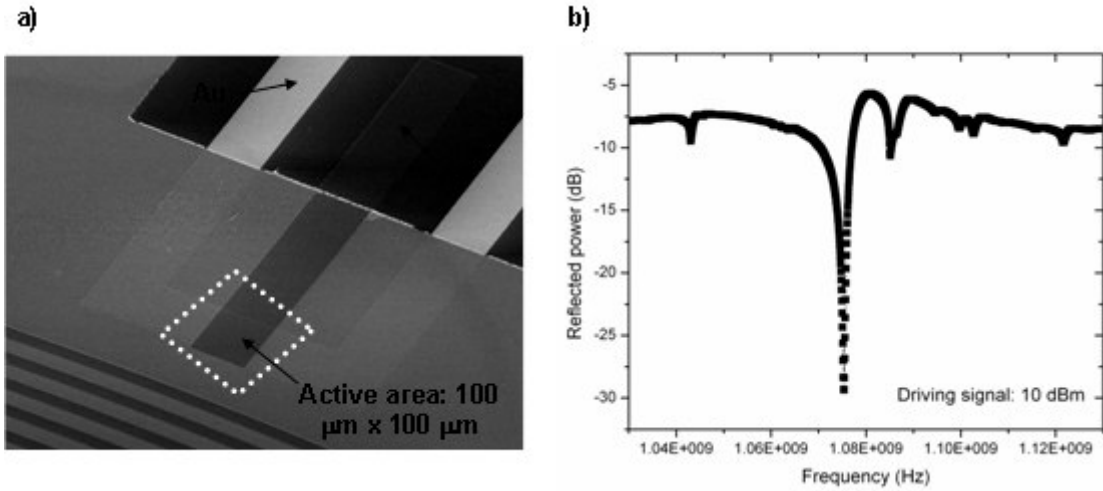
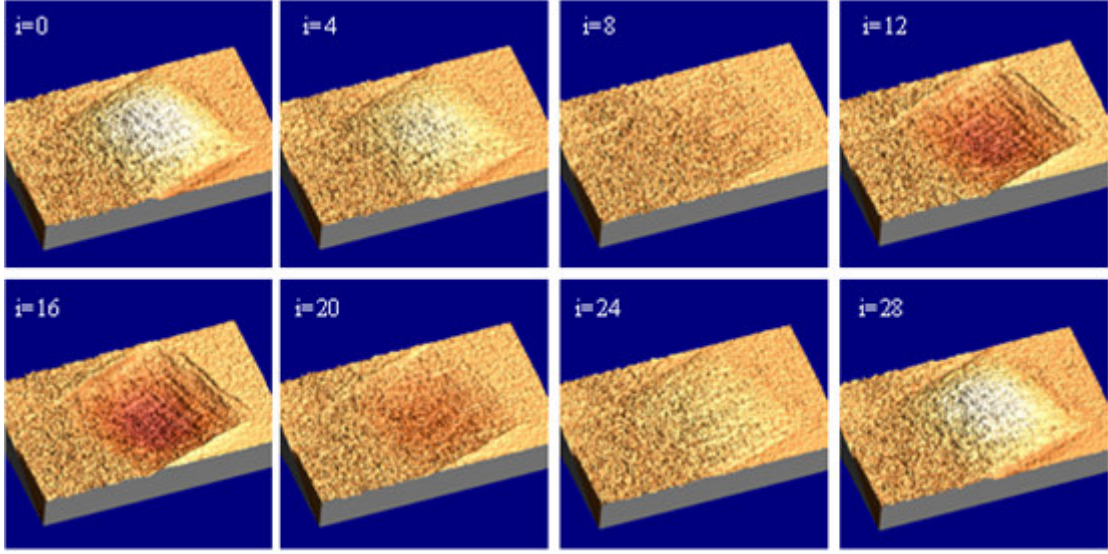
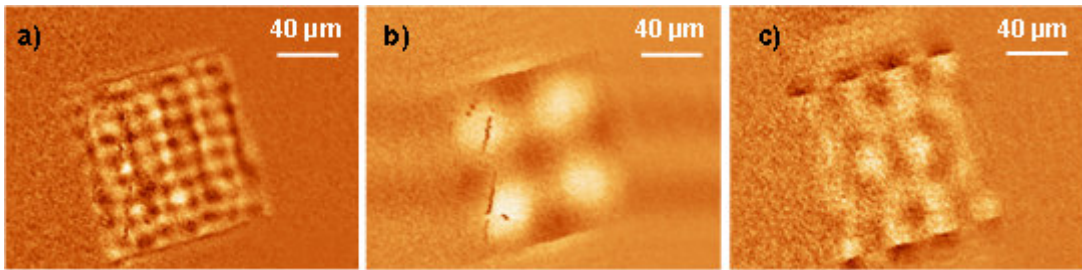


Figure 3.12: (a) SEM of 100 μm wide square ZnO FBAR where the dotted trapezoid depicts the field of view in subsequent interferometer images; (b) FBAR reflection coefficient at +10 dBm input power.



*Figure 3.13: ZnO mode shapes at 1.077 GHz. The frame number is designated by index “i”, where a full period of motion consists of thirty frames, and the corresponding resonator phase equals  $2\pi i / 30$ .*

Figure 3.14 shows images of the FBAR mode shapes at drive frequencies 983 MHz, 1.094 MHz, and 1.133 GHz. As the frequency is swept through the FBAR resonances, the standing lateral Lamb modes exhibit a wavelength from 4  $\mu\text{m}$  to 50  $\mu\text{m}$ . These parasitic modes lower the FBAR quality factor but can be reduced by eliminating in-plane parallel boundaries.



*Figure 3.14: ZnO FBAR mode shape at (a) 983 MHz, (b) 1.094 GHz, and (c) 1.133 GHz.*

### 3.5 AlN FBAR Mode-Shape Imaging with Novel Tapping-Mode Atomic Force Microscopy

The atomic force microscope (AFM) can produce images of high-frequency resonators with sub-nm vertical resolution and nm lateral resolution. In the conventional “contact-mode” or “scanning-mode” AFM configuration, depicted in Figure 3.15, the AFM cantilever tip is dragged across the resonator surface at a constant force.

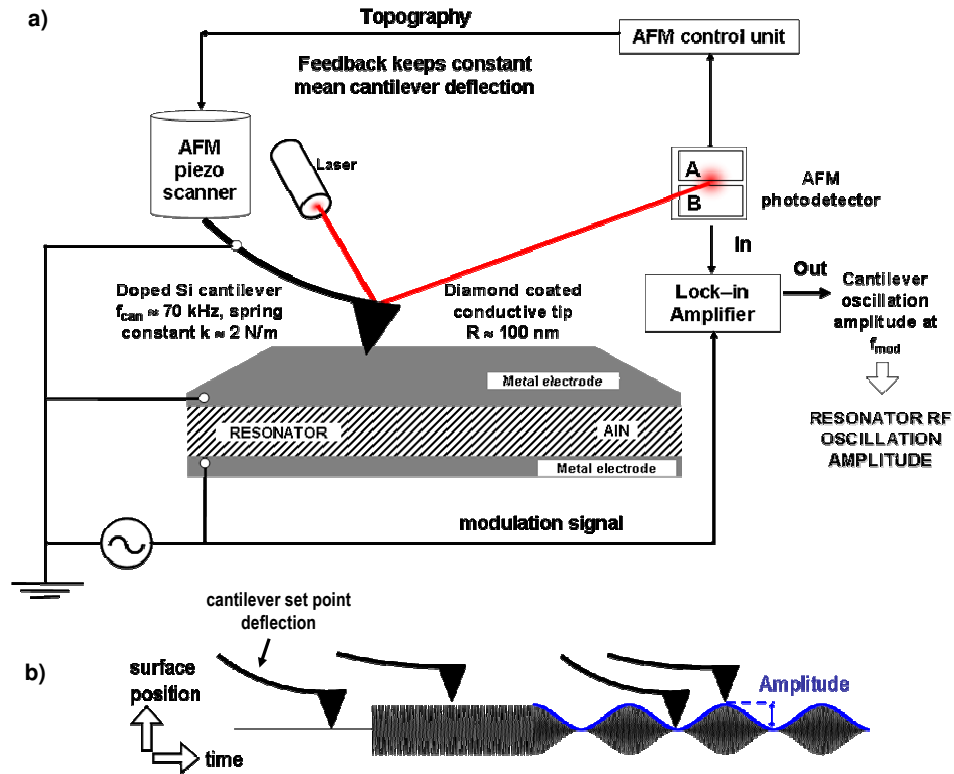
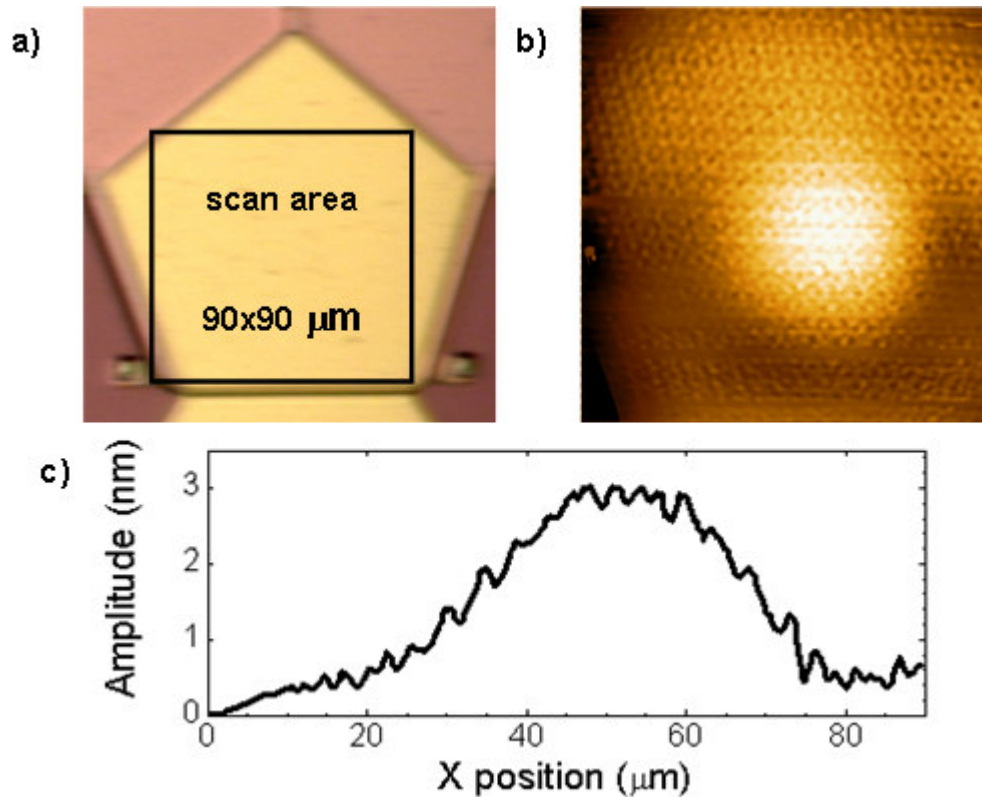


Figure 3.15: (a) Schematic of contact-mode AFM resonator imaging setup; (b) amplitude-modulated FBAR profile showing contact-mode cantilever scanning. (Figure courtesy of Alvaro San Paulo)

Variations in surface topology are compensated by a feedback loop controlling the vertical position of the cantilever (and thus the force it exerts on the sample). Since the cantilever, whose resonant frequency is  $\sim 70$  kHz, cannot follow

the GHz FBAR motion, the FBAR input drive signal is amplitude modulated at a frequency below the cantilever resonant frequency. Resonator amplitude is extracted by locking into the frequency of the amplitude modulation.

Figure 3.16b shows a  $90\text{ }\mu\text{m} \times 90\text{ }\mu\text{m}$  AFM scan of an Agilent AlN FBAR (optical micrograph in Figure 3.16a) at the series resonant frequency, 1.898 GHz. Figure 3.16c plots the resonator amplitude across the middle of the device. Lateral modes superimposed on the primary mode shape are evident, but their amplitude is suppressed because of the non-parallel FBAR edges. The ability to accurately image the FBAR mode shape illustrates the power of the AFM technique.



*Figure 3.16: (a) Optical micrograph of Agilent AlN FBAR (series resonant frequency is 1.898 GHz); (b) AFM tapping mode image of  $90\text{ }\mu\text{m} \times 90\text{ }\mu\text{m}$  scan at resonant frequency; (c) plot of FBAR amplitude across the middle of the FBAR. (Figure courtesy of Alvaro San Paulo)*

There are several drawbacks associated with the use of this scanning-mode AFM imaging technique.

- The scan time is long - for example, the image acquisition time for the 90  $\mu\text{m}$  x 90  $\mu\text{m}$  plot in Figure 3.16b was one hour.
- As shown in Figure 3.17a, for modulation frequencies between 10 Hz and 50 kHz), thermal expansion effects (membrane bowing) distort the resonator RF mode shape and measured amplitude<sup>6</sup>. In the Figure, due to the first-order nature of the thermal effects, the amplitude starts to roll off with frequency at 10 dB / decade at the pole frequency of  $\sim 300$  Hz. Above  $\sim 10$  kHz, the amplitude of the thermally induced bowing falls below that of the RF thickness-extensional FBAR mode. The peak in the vicinity of  $\sim 70$  kHz is the cantilever's mechanical resonance (it is possible there is also gain peaking due to low phase margin in the surface-topology feedback loop). As a direct consequence, only the range of frequencies between  $\sim 10 - 50$  kHz, where the cantilever frequency response is flat, has been found to be useful for resonator imaging.
- As shown in Figure 3.17b, since the force of the cantilever damps the resonator, the measured mode shape is a function of the cantilever force (the force is proportional to the cantilever curvature due to its vertical set point above the sample (see Figure 3.15)).

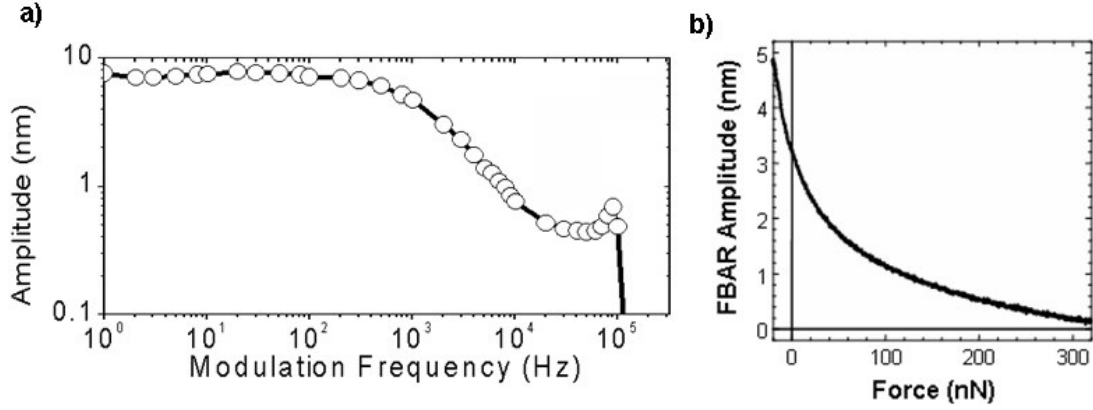


Figure 3.17: (a) Measured FBAR amplitude as a function of modulation frequency; (b) measured FBAR amplitude as a function of cantilever force (Figure courtesy of Alvaro San Paulo).

There is a second AFM imaging technique known as “tapping-mode” (TAFM), in which the cantilever is driven sinusoidally by the AFM piezoelectric scanner (“AFM piezo scanner” in Figure 3.15) at a frequency  $f_{tap}$ . The cantilever tip makes periodic contact with the sample surface, and the surface topography feedback-loop controls the amplitude of the cantilever tip and thus the tip’s interaction force with the sample. Previous efforts to AFM image an RF resonator in tapping-mode employed a resonator input drive that was amplitude modulated at the cantilever drive frequency  $f_{tap}$ . These efforts proved unsuccessful because the surface topography feedback-loop contaminated the RF amplitude measurements made at the same modulation frequency ( $f_{tap}$ ).

Working with Alvaro San Paulo, we developed a novel tapping-mode AFM technique that exploits the second eigenmode of the cantilever and circumvents the problem with conventional tapping-mode measurements made near the fundamental cantilever resonant frequency<sup>7</sup>. As shown Figure 3.18, the cantilever is driven at the



first cantilever resonant frequency while the FBAR is amplitude modulated at the second cantilever resonant frequency.

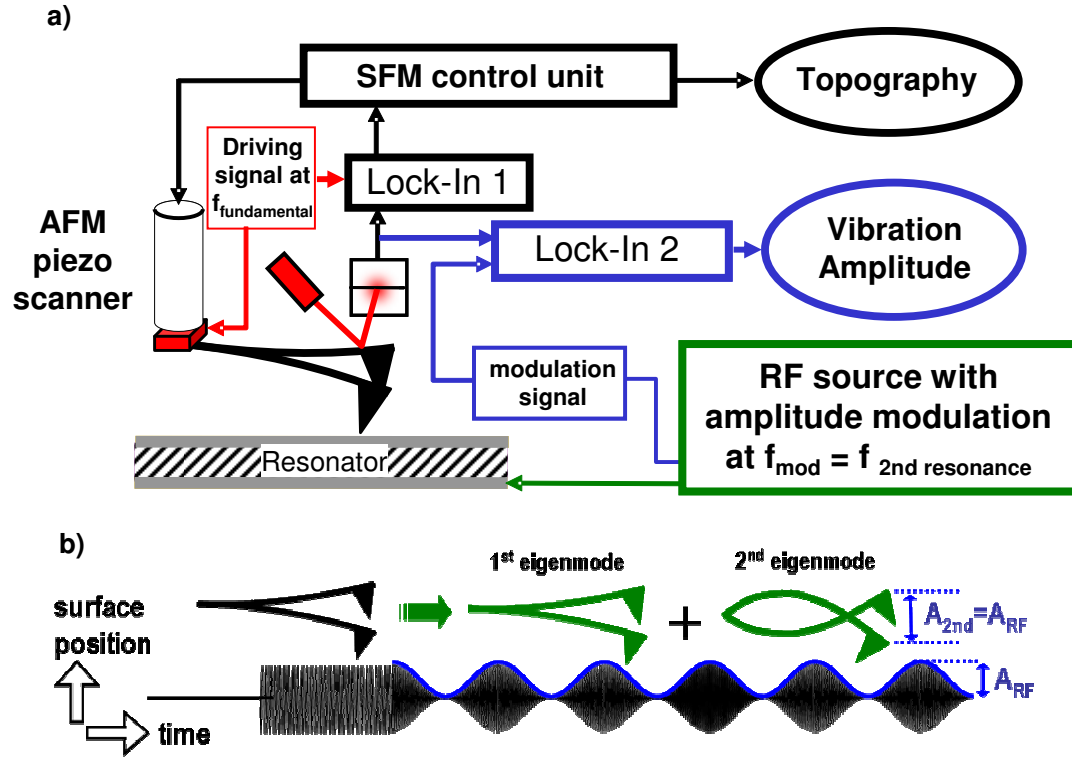
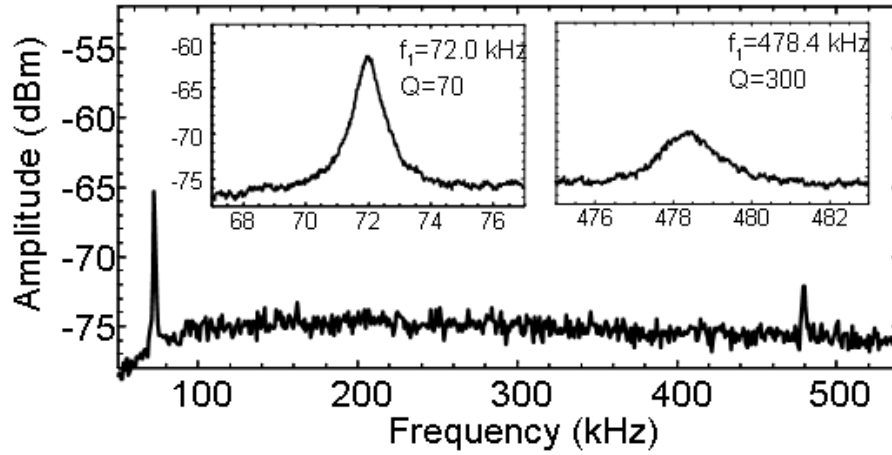


Figure 3.18: (a) Tapping-mode AFM imaging experimental set-up; (b) amplitude-modulated FBAR profile showing that the cantilever motion is now the superposition of the 1<sup>st</sup> and 2<sup>nd</sup> eigenmodes. The topography is extracted from the cantilever signal at the first resonant frequency and FBAR RF amplitude from the amplitude of the second resonant frequency.

Figure 3.19 shows the AFM cantilever output spectrum measured by connecting the photodetector output to a spectrum analyzer. For the measurement, the cantilever tip was in standby mode (suspended in air from the “AFM piezo scanner”), no input drive was applied to the “AFM piezo scanner”, and no sample was in the vicinity of the cantilever tip. The peaks, observed at a frequency of 72.0 kHz and 478.4 kHz, correspond to the fundamental and second resonant frequencies

of the cantilever. They are believed to be excited by a combination of thermal noise and ambient acoustic vibration (the AFM is housed on a vibration table).



*Figure 3.19: Cantilever output spectra measured by connecting the photodetector output to a spectrum analyzer. The insets show the first and second resonant modes at 72.0 kHz and 478.4 kHz respectively. No drive was applied to the cantilever which was in standby mode (resting in air with no sample nearby). The peaks are believed to be excited by a combination of thermal noise and ambient acoustic vibration coupled into the setup.*

Figure 3.20 depicts a conceptual model of how the tip-sample interaction affects the motion of the cantilever. In the trough the cantilever's sinusoidal oscillation, the tip is subject to a periodic force due to its interaction with the resonator. The forcing function is approximately sinusoidal in nature with a frequency equal to that of the resonator AM modulation frequency (set equal to the second resonant frequency of the cantilever).

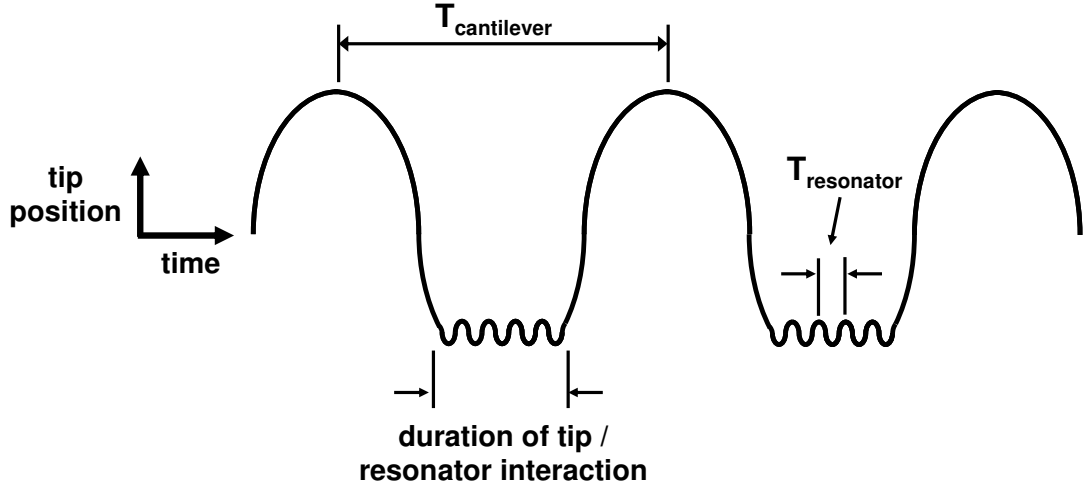
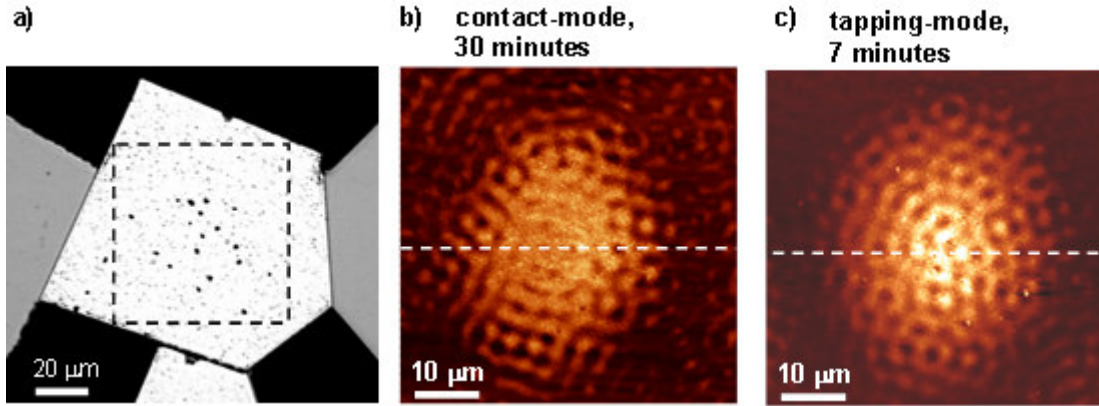


Figure 3.20: Conceptual model of tip-sample interaction.  $T_{\text{cantilever}}$  is the period of the cantilever drive frequency (set equal to the cantilever fundamental resonant frequency, 72.0 kHz) and  $T_{\text{resonator}}$  is the period of the FBAR drive frequency (set equal to the cantilever second resonant frequency, 478.4 kHz). The cantilever experiences a periodic forcing function due to its interaction with the sample.

A Fourier expansion of the periodic force on the tip shows that there is energy generated at both the fundamental and second resonances of the cantilever. A surface-topography feedback signal can now be measured by locking into the cantilever fundamental frequency. To measure the FBAR RF amplitude, a second lock-in amplifier is tuned to the AM modulation signal at the second cantilever resonance.

In comparison to contact-mode imaging, our TAFM technique offers a dramatic improvement in speed and in mode-shape resolution. Figure 3.21b and Figure 3.21c compare contact-mode and tapping-mode AFM images of the MEMS PM monitor pentagonal AlN FBAR shown in Figure 3.21a. Figure 3.22 compares the FBAR amplitude measured with contact-mode and tapping-mode along the dotted lines in Figure 3.21b and Figure 3.21c. The tapping-mode AFM technique was four times faster than the contact-mode technique, it provided higher resolution,

and caused less distortion of the FBAR mode shape. In these experiments, the speed of the tapping-mode scan was limited by the bandwidth of the factory-set surface-topography feedback control loop. If a control loop with a wider bandwidth were employed, even faster tapping-mode images would be possible with some trade-off in resolution.



*Figure 3.21: (a) Optical micrograph of pentagonal AlN FBAR; (b) FBAR mode-shape taken by contact-mode AFM scan in 30 minutes (the scan area is outlined); (c) FBAR mode-shape taken by tapping-mode AFM scan in 7 minutes. During imaging the FBAR was driven at its series resonance 1.595 GHz with 0 dBm input power.*

Figure 3.23a and Figure 3.23c compare the FBAR amplitude as a function of frequency measured in contact-mode and tapping-mode, respectively. Once again, the tapping-mode provides a much cleaner scan and the series resonance at 1.595 GHz is noticeably sharper. Figure 3.23b illustrates the effect of the cantilever damping force in contact-mode (deflection denotes the cantilever bending or deflection as it makes contact with sample (see Figure 3.15)). As shown in Figure 3.23d, the periodic cantilever contact with the FBAR surface in tapping-mode caused no measurable damping of the FBAR amplitude.

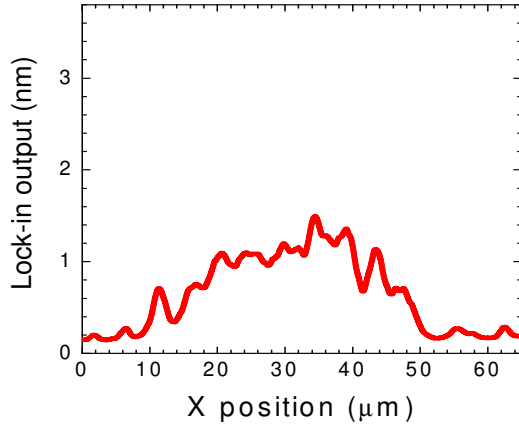
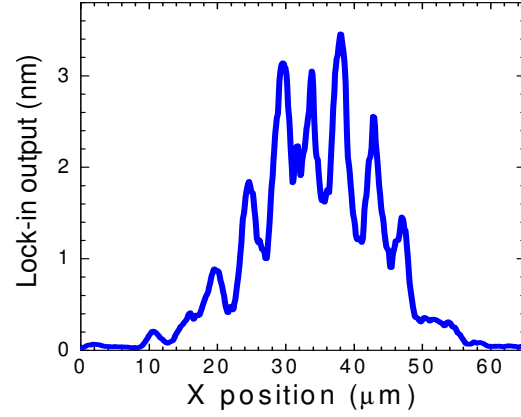
**a) contact-mode****b) tapping-mode**

Figure 3.22: (a) FBAR amplitude along the dotted line of Figure 3.21b; (b) FBAR amplitude along the dotted line of Figure 3.21c. It is evident that the tapping-mode output shows much better lateral resolution and does not damp the FBAR motion.

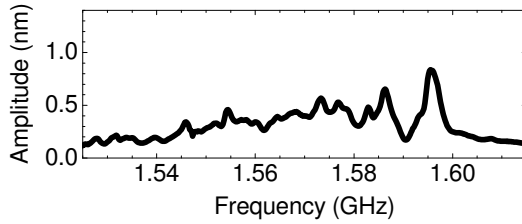
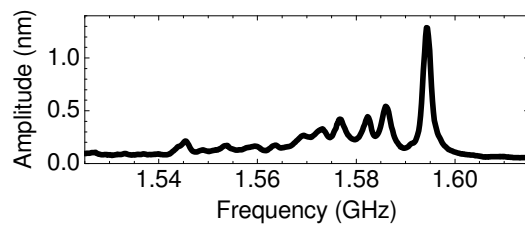
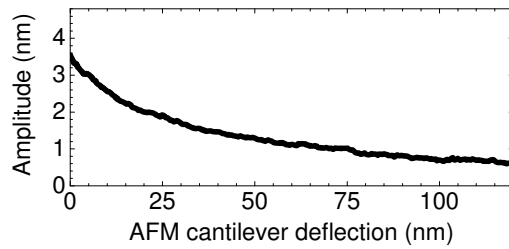
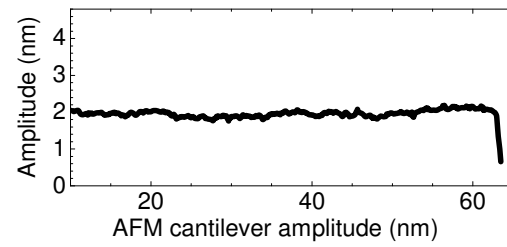
**a) contact-mode****c) tapping-mode****b)****d)**

Figure 3.23: (a) FBAR amplitude as a function of frequency measured with contact-mode; (b) FBAR amplitude as a function of contact-mode cantilever deflection; (c) FBAR amplitude as a function of frequency measured with tapping-mode; (d) FBAR amplitude as a function of tapping-mode cantilever amplitude.

### **3.6 FBAR Pierce Oscillator**

#### **3.6.1 MEMS PM FBAR Oscillator Performance**

The MEMS PM monitor incorporates a four-element Pierce FBAR oscillator array designed in a 0.25  $\mu\text{m}$  CMOS technology. This Section discusses the performance of a typical Pierce oscillator incorporating a 150  $\mu\text{m}$  wide square AlN FBAR whose SEM and reflection coefficient are given in Figure 3.24a and Figure 3.24b, respectively. The FBAR had an  $R_x$  of 2.56  $\Omega$ , a Q of 1635, and a series resonant frequency of 1.588 GHz.

To interface electrically the resonator and its circuit, the FBAR die and 2.4 mm by 2.4 mm CMOS chip were glued with cyanoacrylate to the PCB shown in the Orcad layouts of Figure 3.25. To interface with a preexisting aerosol sampler, the two-layer FR4 board (FR4 stands for “Flame Retardant 4” and is a widely used insulating material for making printed circuit boards) consists of three copies of the same circuit, each composed of decoupling capacitors and DC power and RF (SMA) connections. RF and DC power connections were made between the FBAR and the CMOS circuits and between the CMOS circuits and PCB with Al wirebonds. For ease of wirebonding, the PCB should be coated with a hard-gold finish, as wirebonding to the standard tin PCB pads is difficult. The board geometry was designed during the early stage of the project to interface with an existing LBNL aerosol sampler (discussed in detail in Chapter 4); therefore there are two sets of RF and supply CMOS bond pads.

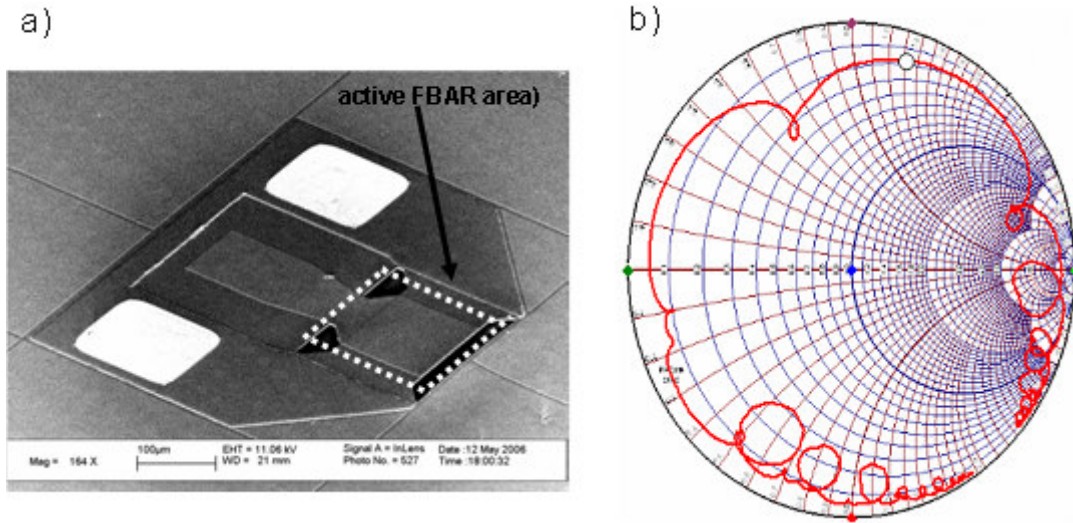


Figure 3.24: (a) SEM of 150  $\mu\text{m}$  wide square FBAR used in the Pierce oscillator (the active FBAR area is outlined by the dotted white line); (b) S11 of the FBAR. The FBAR had an  $R_x$  of  $2.56 \Omega$ , a  $Q$  of 1635, and a series resonant frequency equal to 1.588 GHz.

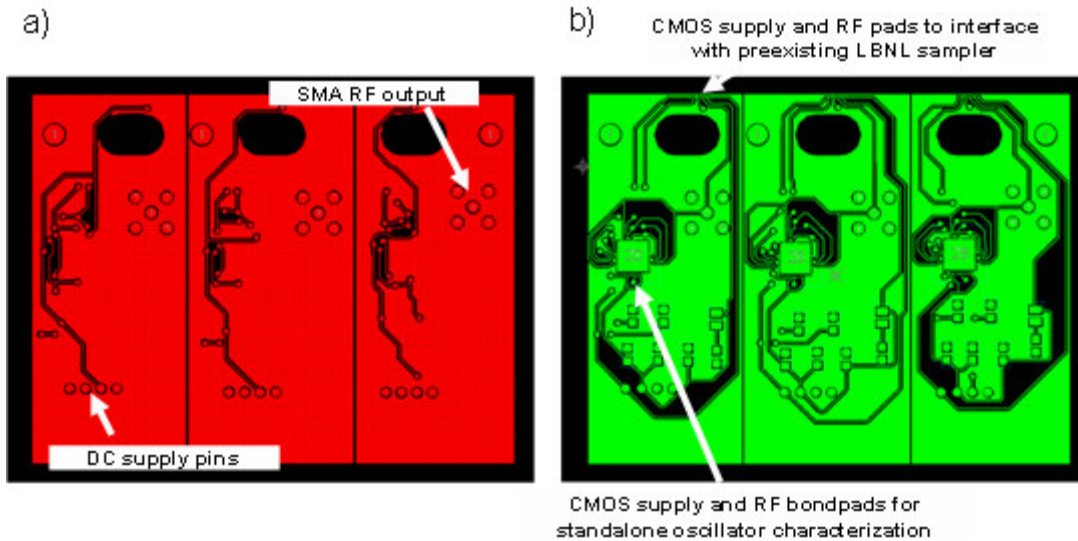
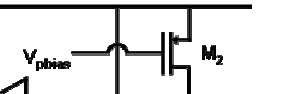


Figure 3.25: (a) Orcad layout of bottom PCB metal; (b) layout of top PCB metal. This board was designed to interface with a preexisting LBNL sampler and to alternatively operate as a stand-alone oscillator test fixture. Thus, the board contains two sets of RF and supply CMOS bondpads.

a) 


b) 

Figure 3.27a plots the output spectrum of the MEMS PM monitor FBAR oscillator centered at 1.5997 GHz with a 1 MHz bandwidth, and Figure 3.27b plots the oscillator output from 60 MHz to 13.15 GHz. The output power of the fundamental was -5.3 dBm and the first three oscillator harmonics were attenuated



42.5, 22.7, and 37 dB, respectively. The oscillator and buffer drew 2.4 mA and 21.7 mA from a 3 V supply, respectively. Figure 3.28 plots the oscillator phase noise which, at an offset of 10 kHz from the fundamental, has a value of -102 dBc / Hz.

Both oscillator designs were made early in the project, before high-quality AlN FBARs were fabricated, and were designed to oscillate with low-quality FBARs. With proper redesign, sub-mW power consumption should be readily attainable.

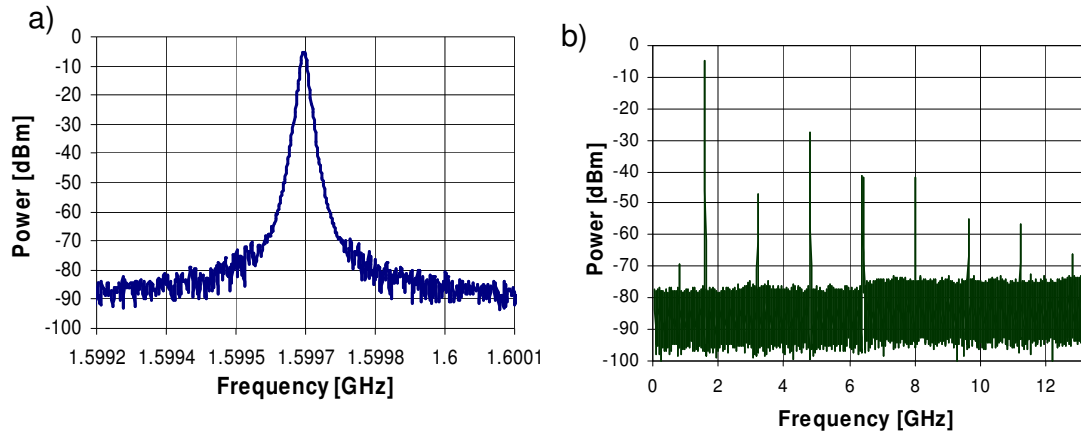


Figure 3.27: (a) FBAR Pierce oscillator output spectrum with fundamental mode at 1.5997 GHz and an output power of -5.3 dBm ; (b) oscillator harmonics (the source of the peak at ~700 MHz is unknown but is believed to be due to a parasitic oscillation at a lateral resonance of the square-shaped FBAR).

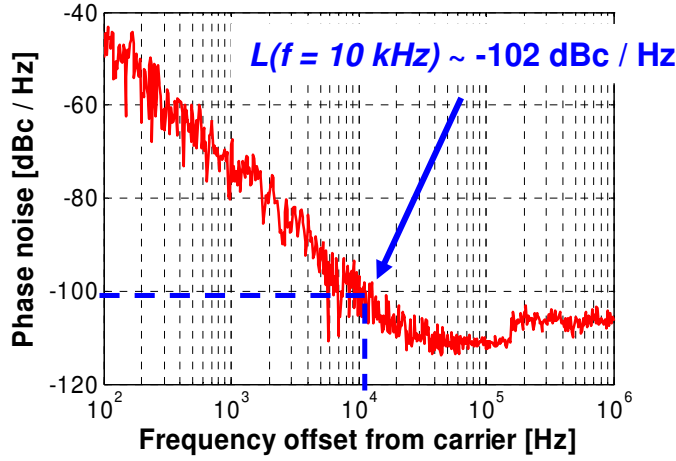


Figure 3.28: Oscillator phase noise, which at a frequency offset of 10 kHz, is -102 dBc / Hz.

### 3.6.2 Analysis of Oscillator Startup

One can study the dynamics of the oscillator startup with the loop-gain derivations of Chapter 2. A practical example of this analysis is now made for a 100  $\mu\text{m}$  x 100  $\mu\text{m}$  AlN FBAR whose impedance is plotted in Figure 3.29. As shown in the Figure inset, the lumped LCR model of this device includes a parasitic resistor  $R_p$  in series with FBAR capacitance  $C_o$ .  $R_p$  captures the effect of dielectric and substrate losses and improves the model of the resonator behavior in the vicinity of the parallel resonance. The numerically extracted lumped elements are  $R_x = 3.5 \Omega$ ,  $R_p = 8.5 \Omega$ ,  $C_x = 35.5 \text{ fF}$ ,  $L_x = 236.1 \mu\text{H}$ , and  $C_o = 0.75 \text{ pF}$ .

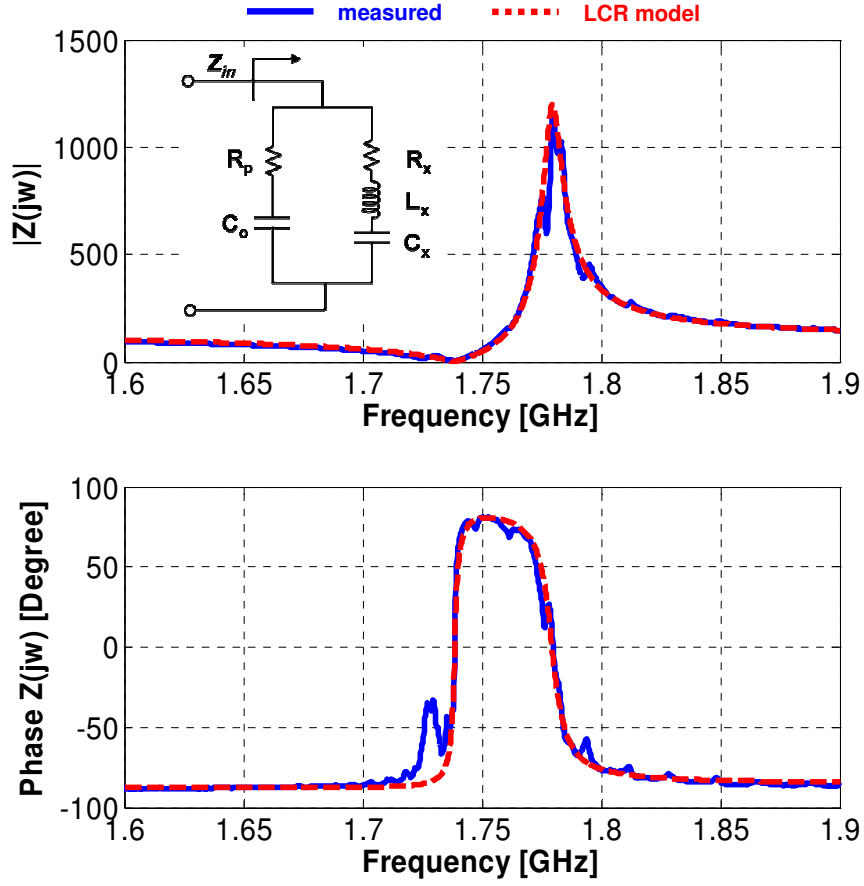


Figure 3.29: Magnitude and phase of impedance of  $100 \mu\text{m} \times 100 \mu\text{m}$  AlN FBAR used for exposition of oscillator startup analysis. Inset shows lumped LCR model that includes a resistor  $R_p$  in series with  $C_o$  to model dielectric and substrate losses.

At the series and parallel resonances, the impedances looking into the FBAR terminals are:

$$Z_{in}(f_s) \cong R_x = 3.5\Omega \quad \text{Eq. 3.2}$$

$$Z_{in}(f_p) \cong \frac{1}{\omega_p^2 C_o^2 (R_x + R_p)} = 1184\Omega \quad \text{Eq. 3.3}$$

Thus, in comparison to the series resonance, at the parallel resonance only a small amount of current flows into the FBAR terminals and the device can be

approximated as an open circuit. Employing the open-circuit approximation, the parallel resonance quality factor  $Q_p$  is:

$$Q_p = \frac{Q_s \frac{f_p}{f_s}}{1 + \frac{R_p}{R_x}} \quad \text{Eq. 3.4}$$

The FBAR was interfaced electrically to the first CMOS oscillator design with ~5 mm long bondwires. As shown in Figure 3.30, the small-signal oscillator model at startup, each 5 mm bondwire contributes ~ 2.5 nH of inductance ( $L_{par}$ ) in series with the FBAR. The oscillator was found to cut off at a transistor M2 gate bias ( $V_p$ ) of 1.83 V with an oscillation frequency of 1.7238 GHz ( $V_{dd} = 2.5$  V).

Figure 3.31 plots the simulated resistance  $R_I$  (equal to  $r_{oM1} \parallel r_{oM2}$ ) and  $g_{mI}$  (see Figure 3.30) as a function of the PMOS transistor M2 bias voltage. At  $V_p = 1.83$  V, it is seen that  $R_I$  and  $g_{mI}$  equal 3.3 k $\Omega$  and 7.1 mS, respectively. The impedance of the feedback bias transistor M3 was 6.2 k $\Omega$ . At  $V_p = 1.83$  V, capacitors  $C_1$  and  $C_2$  were 233 fF ( $C_{ds1} = 213$  fF and  $C_{ds2} = 20$  fF) and 792 fF ( $C_{gs1} = 792$  fF), respectively. To account for bond pads and metal interconnect, a parasitic capacitance of 125 fF was subsequently added to  $C_1$  and  $C_2$  in the simulation.

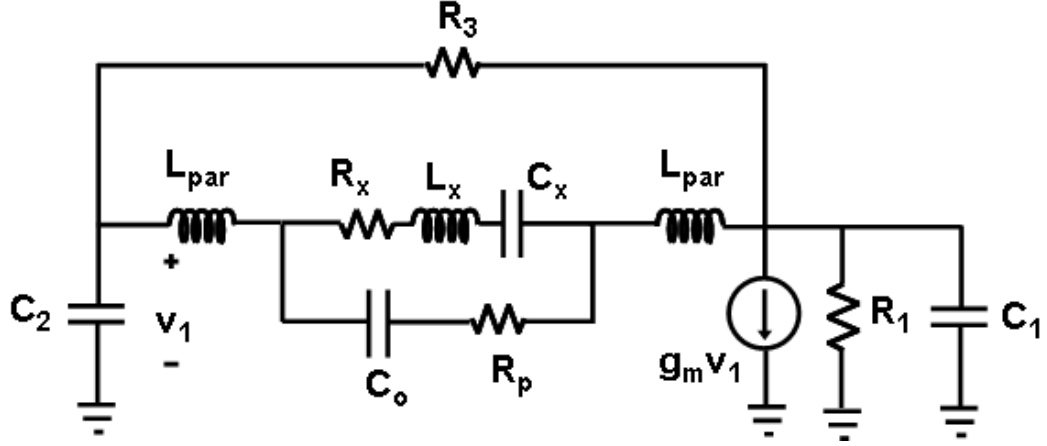


Figure 3.30: Refined small-signal oscillator model for startup analysis incorporating  $L_p = 2.5$  nH to model bondwire inductance and  $R_p$  to model resonator substrate and dielectric losses.

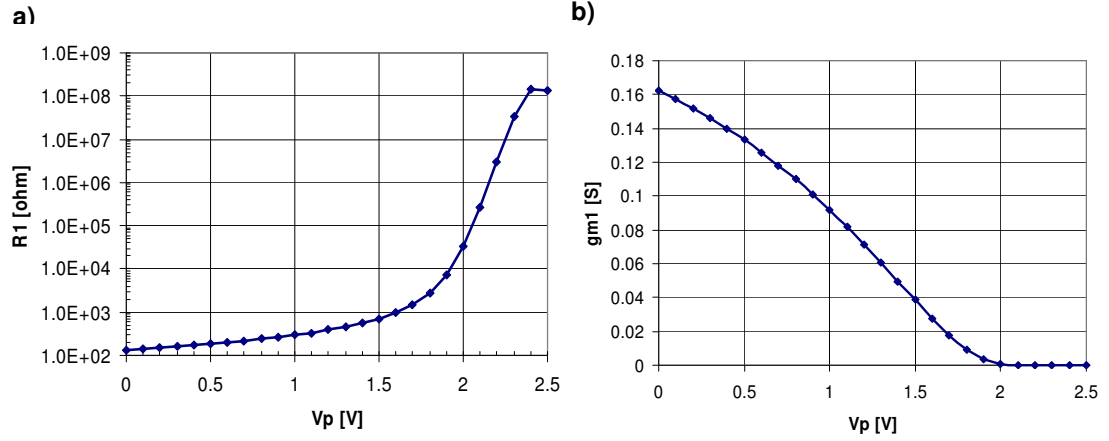


Figure 3.31: (a) Simulated resistance  $R1$  (see Figure 3.30,  $R1 = r_{oM1} \parallel r_{oM2}$ ) as a function of PMOS load transistor M2 bias voltage; (b) simulated  $g_{m1}$  as a function of PMOS transistor M2 bias voltage.

In order to incorporate the inductance ( $L_p$ ) and  $R_p$  into the oscillator loop-gain model, the feedback impedance (FBAR in parallel with bias transistor M3) from Eq. 2.81 is rederived as:

$$Z_s = \frac{s^4 2L_p L_x C_x C_o + s^3 C_o C_x [R_p L_x + 2L_p (R_x + R_p)] + s^2 [L_x C_x + C_o C_x R_p R_p + 2L_p (C_x + C_o)] + s(C_x R_x + C_o R_p + 2L_p) + 1}{s^4 2L_p L_x C_x C_o + s^3 C_o C_x [L_x (R_x + R_p) + 2L_p (R_x + R_p)] + s^2 [L_x C_x + C_o C_x (R_x R_p + R_p R_x + R_p R_p) + 2L_p (C_x + C_o)] + s[C_x R_x + C_o R_p + 2L_p + R_p (C_x + C_o)] + 1 + R_p} \quad \text{Eq. 3.5}$$

Figure 3.32 plots the root locus of the full oscillator circuit. The minimum transconductance  $g_{ml}$  for oscillation is 6.0 mS, which is close to the experimentally determined oscillator cutoff value of 7.1 mS. Interestingly, the bondwire inductance introduces a parasitic mode at ~ 5.15 GHz which has been observed experimentally. The Nyquist plot in Figure 3.33, parameterized for  $g_{ml}$ , confirms oscillator behavior for  $V_p = 1.83$  V.

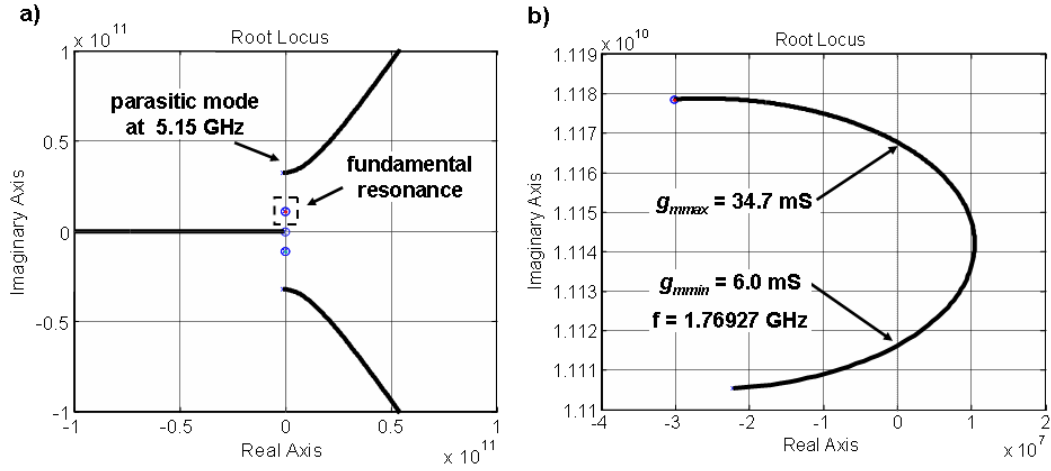


Figure 3.32: (a) Root locus of oscillator loop gain; (b) zoomed view of pole trajectory at fundamental resonance. The theoretically predicted minimum transconductance for oscillation is 6.0 mS, which is close to the experimentally measured value of 7.1 mS. The bondwire inductance introduces a parasitic mode at ~ 5.15 GHz which has been observed experimentally.

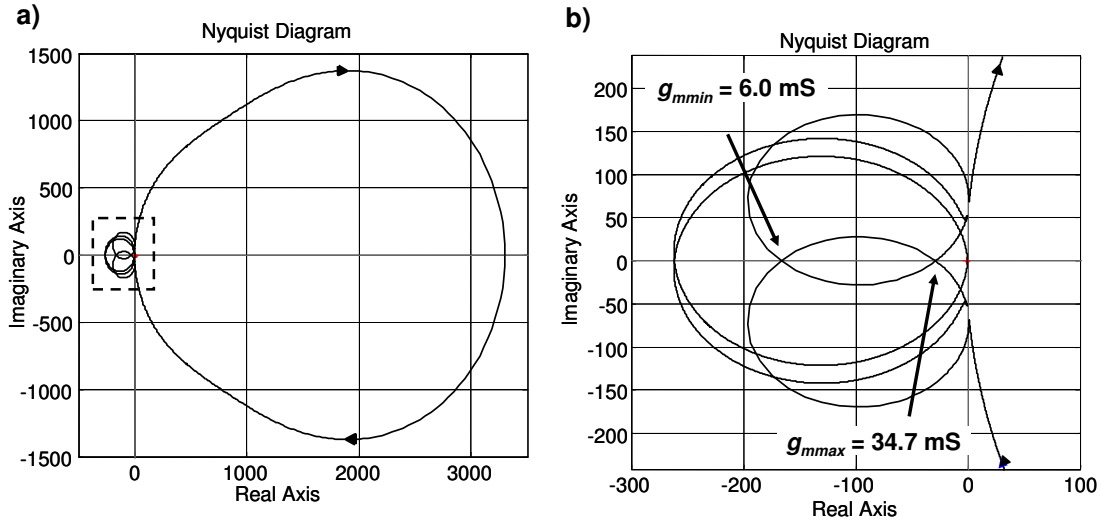


Figure 3.33: (a) Nyquist plot of oscillator loop gain parameterized for  $g_{m1}$ , confirming loop gain instability; (b) expanded view of trajectory outlined by the dotted box in figure (a).

### 3.6.3 Oscillator Temperature Dependence

The temperature dependence of the FBAR is due to the elastic modulus temperature coefficient of frequency (TCF) of the constituent films (aluminum nitride, platinum, and aluminum). The frequencies of two FBAR oscillators as a function of temperature are shown in Figure 3.34.

The TCF of the FBAR oscillator frequency is quite constant and typically lies in the range of -24 to -25 ppm per °C. The TCF is negative because the AlN film softens (elastic modulus decreases) with increasing temperature. It has been found that due to variations in FBAR film thicknesses, FBAR and CMOS chip mounting (adhesive), bondwires, etc., it is quite difficult to obtain two FBAR resonators with matched TCFs, even if the FBARs are on the same piece of silicon. Consequently, as described in Chapter 4, before collection of mass sensor data, the

TCF of each FBAR mass sensor must be measured by performing a simple baseline run over the operating temperature with no particles.

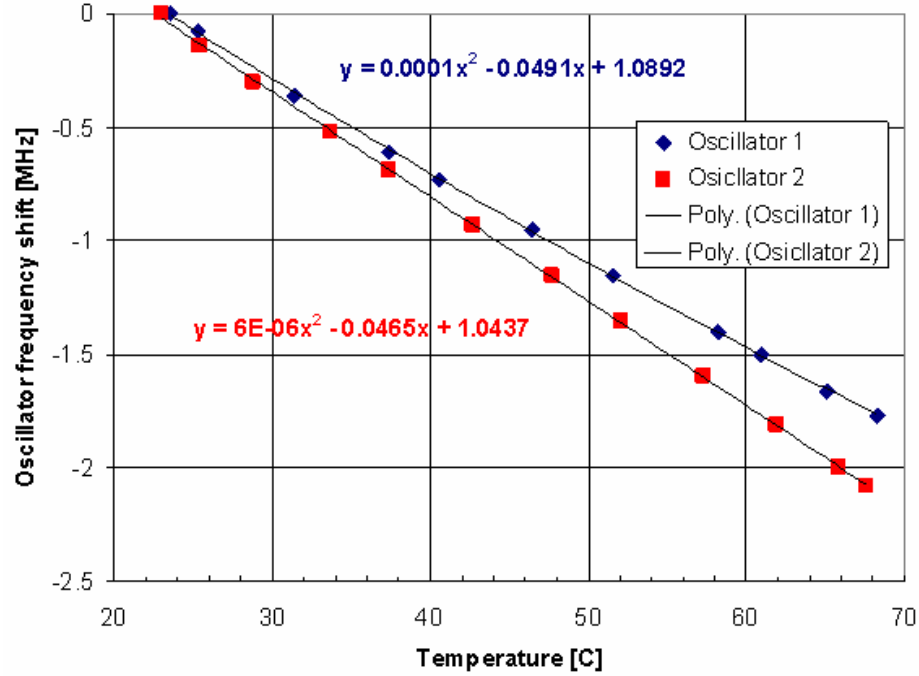


Figure 3.34: Frequency shift vs. temperature for two FBAR oscillators. The FBAR mass sensor temperature coefficient of frequency is highly linear and typically lies in the range of -24 to -25 ppm per °C. In the legend, “Poly” defines the second order line fit to the measured data.

### 3.7 Fabrication and Characterization of Thermal Precipitator

Figure 3.35a is a photograph of the quartz / polysilicon serpentine heater and power cable. Power is supplied through a connector attached to the chip with conductive epoxy. Figure 3.35b contains the Cadence layout of the heater with a magnified view of the four-element heater array. The heater traces for this design were 80  $\mu\text{m}$  wide. Figure 3.36 contains two SEMs revealing the details of the polysilicon serpentine filament. In separate experiments, the percentage of light



transmission through a 1  $\mu\text{m}$  thick polysilicon film on a 500  $\mu\text{m}$  thick quartz substrate was found to be 55% and 2% at 810 nm and 370 nm, respectively.

The heater fabrication was begun by depositing 2  $\mu\text{m}$  of doped polysilicon onto a quartz wafer. Quartz was chosen as the substrate material since it is transparent at the UV and IR PM monitor interrogation wavelengths. After lithographic definition of a thick PR mask, the polysilicon was dry etched in an  $\text{SF}_6$  plasma. For thermal isolation the quartz underlying the serpentine polysilicon filament was removed in a timed concentrated HF etch. The etch duration was about one hour, and undercut of the quartz can be seen Figure 3.36a. The polysilicon dopants were not activated with a high temperature anneal as it was found annealed films shattered during the HF etch.

Figure 3.37a shows the heater input power vs. temperature as characterized with a forward looking infrared (FLIR) camera. Figure 3.37b shows FLIR images of the heater array at  $T = 23, 37, 70$  and  $125^\circ\text{C}$ . For thermophoresis in the MEMS PM monitor, the target temperature of  $100^\circ\text{C}$  required a supply power of 52 mW.

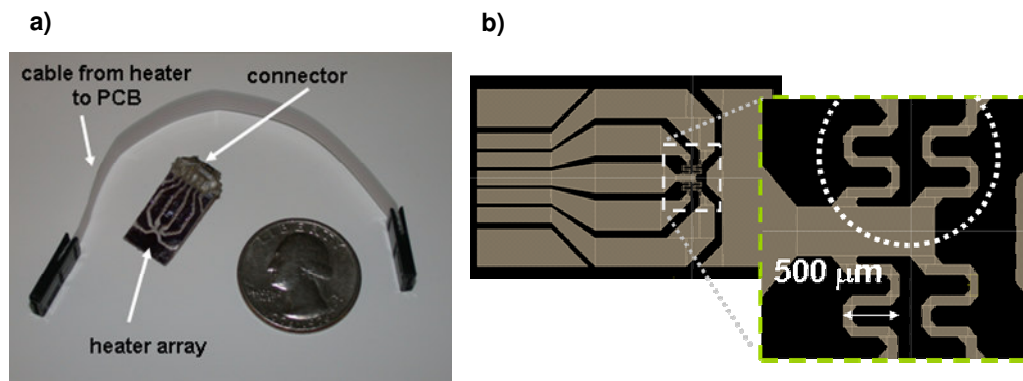


*Figure 3.35: (a) Photograph of quartz / polysilicon heater with connector attached with conductive epoxy and cable (U.S. quarter shown for scale); (b) Cadence layout of heater with magnified view of four-element heater array.*

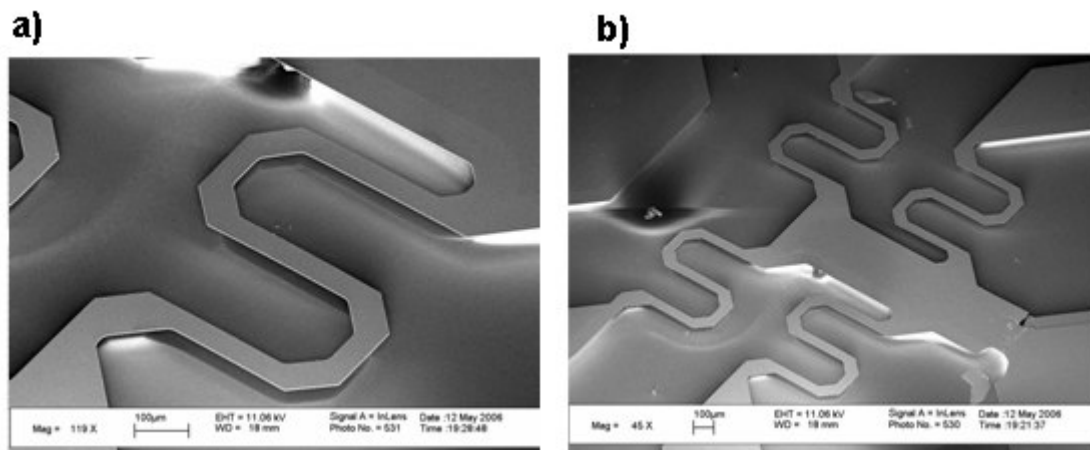


Figure 3.36: (a) SEM of individual heater filament; (b) SEM of four-element heater array.

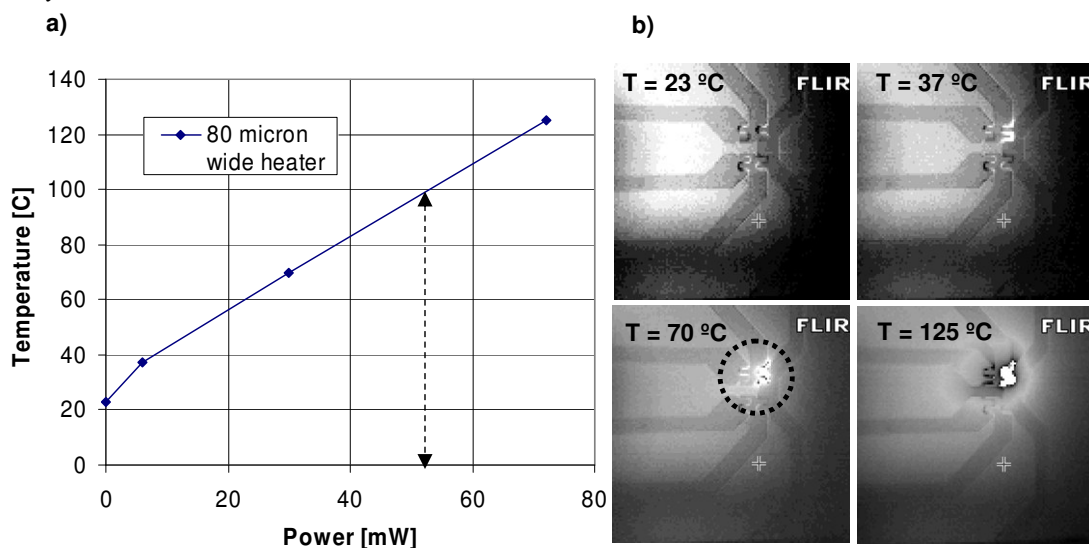
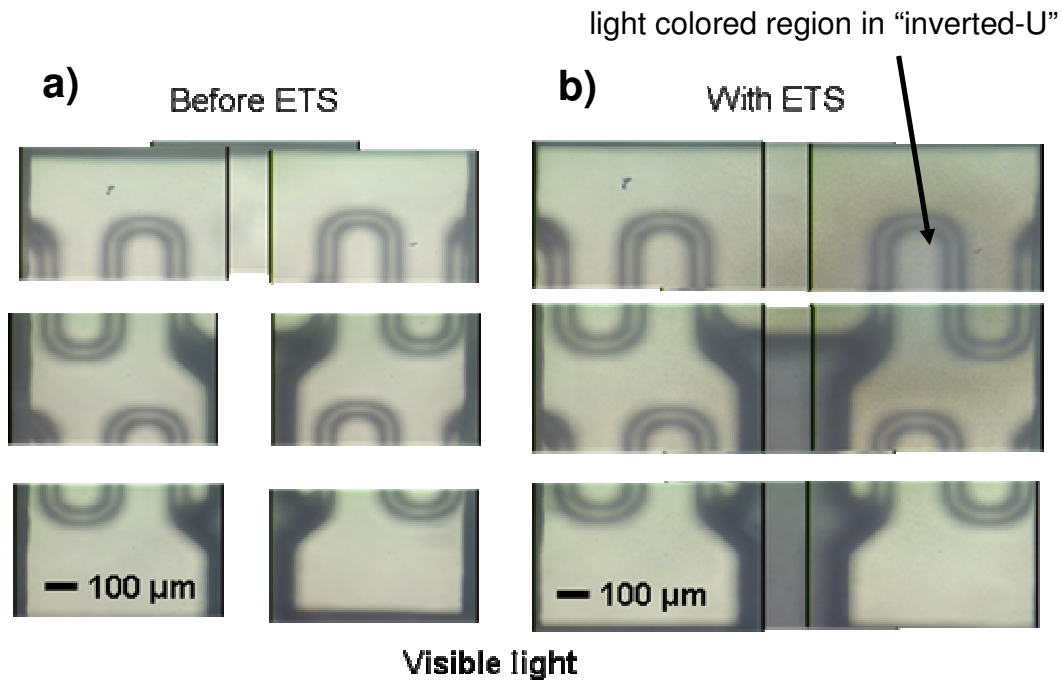


Figure 3.37: (a) Heater input power vs. temperature as characterized with forward looking infrared (FLIR) imaging; (b) FLIR images of heater array at  $T = 23, 37, 70$  and  $125$  °C. Power was applied to the top right heater and the dotted circle in the image corresponds to the dotted circle in Figure 3.36b. The thermophoretic force would be perpendicular to the page

To verify that the micro-fabricated thermophoretic heaters actually caused particulate deposition, the heater assembly was oriented  $500 \mu\text{m}$  above an evaporated Al film on a silicon chip and packaged in the MEMS PM housing. ETS was sampled through the flow channel at  $20 \text{ cm}^3 / \text{min}$  using a peristaltic pump.

Figure 3.38 shows visible light photographs of the aluminum surface as seen through the heater before (a) and after (b) exposure to ETS. The heater at the upper right was powered to reach 100 °C. (Note: Each composite figure is composed of a set of images taken with a visible-light microscope in which the chip size was larger than the microscope field of view. Thus, in order to obtain a high resolution image, the photo was segmented into a 9 x 9 array, each taken with a 5x objective illuminated with visible light. The black lines depict the boundaries of each photo.)



*Figure 3.38: Composite optical image of the polished aluminum surface as seen through the thermophoretic heaters, taken in visible light with a Reichert-Jung Polylite microscope. (a) Before exposure to ETS; (b) after exposure to ETS, with the upper right heater energized.*

The composite image on the right has a brown halo surrounding the inverted-U (central section) of the heater in the upper right corner. Though appearing lighter in the figure, optical inspection with a microscope indicated that

the most ETS deposition occurred in the central area between the arms of the inverted-U as expected. The color of the region is believed to be an optical artifact of the camera. The film texture within the inverted-U also differed from other regions, which might be explained by differences in temperature. When the deposit was viewed in UV light a similar pattern of deposition was observed. This result verified that the thermophoretic precipitator functioned properly.

### 3.8 Chapter 3 References

---

- <sup>1</sup> G. Piazza, "Piezoelectric aluminum nitride vibrating RF MEMS for radio front-end technology", Ph.D. Dissertation, University of California at Berkeley, Berkeley, CA, 2005.
- <sup>2</sup> R. Ruby, J. Larson, C. Feng, and S. Fazio, "The effect of perimeter geometry on FBAR resonator critical performance", *IEEE MTT-S Intl. Microwave Symp. Digest*, pp. 217-200, 2005.
- <sup>3</sup> X. Liu, A. San Paulo, M. Park, and J. Bokor, "Characterization of acoustic vibration modes at GHz frequencies in bulk acoustic wave resonators by combination of scanning laser interferometry and scanning acoustic force microscopy", *Proc. IEEE Intl. Conf. on MEMS*, pp. 175-178, 2005.
- <sup>4</sup> J.V. Knuutilla, P.T. Tikka, and M.M. Salomaa, "Scanning Michelson interferometer for imaging surface acoustic wave fields", *Optics Lett.*, vol. 25, no. 9, pp. 613-615, 2000.
- <sup>5</sup> D. Royer and E. Dieulesaint, "Optical detection of sub-angstrom transient mechanical displacements", *Proc. IEEE Ultrasonics Symp.*, pp. 527-530, 1986.
- <sup>6</sup> A. San Paulo, X. Kiu, and J. Bokor, "Scanning acoustic force microscopy characterization of thermal expansion effects on the electromechanical properties of film bulk acoustic resonators", *Appl. Phys. Lett.*, vol. 86, pp.
- <sup>7</sup> A. San Paulo, J.P. Black, R.M. White, and J. Bokor, "Tapping mode acoustic force microscopy for imaging thin-film bulk acoustic-wave resonators", to be submitted to *Appl. Phys. Lett.*

## 4 MEMS PM Calibration and Monitoring Experiments

This chapter summarizes experiments to calibrate the MEMS PM. Experiments during the development of the MEMS PM monitor took place in a room-sized environmental chamber at LBNL. The challenge aerosol was typically environmental tobacco smoke (ETS) in ambient air, although several experiments sampled diesel exhaust. The culmination of this work was a pilot-scale field test that took place in a single-family house in Berkeley over two ten-day periods in the early summer of 2006.

### 4.1 Experimental Preliminaries

#### 4.1.1 LBNL Environmental Chamber Test Setup

The 24.7 m<sup>3</sup> environmental chamber at LBNL had vinyl flooring and walls of painted gypsum board. Figure 4.1 shows two photographs of the chamber.

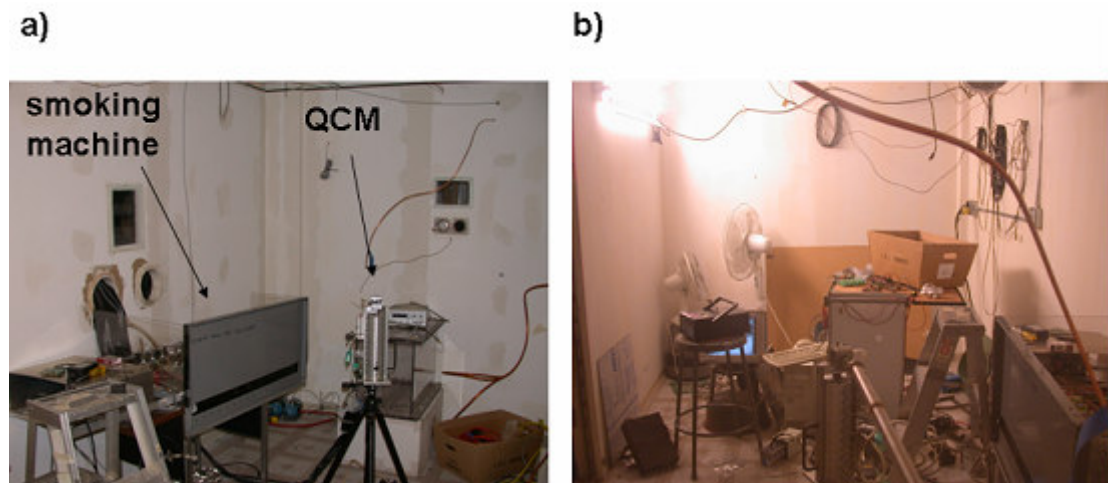


*Figure 4.1: Photos of the LBNL environmental chamber.*

The chamber was equipped with a ventilation system and sensors for real-time monitoring of pressure, temperature, and relative humidity (RH). More information about the chamber is found in <sup>1</sup>. The chamber also contained pumps and flow measurement devices (bubble meters and electronic flow meters).

The following suite of instruments was available for PM monitoring during the chamber experiments:

Instrument	Description
Quartz Crystal Microbalance (QCM) Impactor	The QCM impactor (California Measurements, Model PC-100) consists of 10 impaction stages with size cuts of 0.05, 0.1, 0.2, 0.4, 0.8, 1.6, 3.2 and 6.4 $\mu\text{m}$ for measurement of the PM mass size distribution ( $\mu\text{g}/\text{m}^3$ ). The instrument has customized measurement circuitry and LBNL-built control and data acquisition software. The QCM was operated at a flow rate of $\sim 240 \text{ cm}^3/\text{min}$ , and was typically programmed to start and continue sampling until a pre-selected frequency change was reached for the 0.2 $\mu\text{m}$ stage. The QCM was programmed to restart a new cycle if the pre-set mass loading had not been reached before 30 min.
Optical Particle Counter (OPC)	The OPC has 6 channels to measure the particle number size distribution ( $\# / \text{m}^3$ ), with size bins of 0.3, 0.5, 0.7, 1, 2 and 5 $\mu\text{m}$ (Met One, Model 237B). The PM mass concentration was calculated from these data by summing the product of the estimated average particle volumes in each size bin and the number in that bin. The total particle volume was based on estimated diameters of 0.358 $\mu\text{m}$ , 0.56 $\mu\text{m}$ , 0.81 $\mu\text{m}$ , 1.43 $\mu\text{m}$ , 3.16 $\mu\text{m}$ and 7 $\mu\text{m}$ for the 0.3, 0.5, 0.7, 1, 2 and 5 $\mu\text{m}$ bins, respectively. A particle density of $1 \text{ g}/\text{cm}^3$ was assumed. To estimate PM 2.5, volumes for the lower 5 bins

	were multiplied by the respective particle counts. This volume sum was multiplied by $1 \text{ g/cm}^3$ .
Aethelometer	The Aethalometer measures black carbon (BC) concentrations ( $\mu\text{g/m}^3$ ) from the attenuation of light at 880 nm, and BC-equivalent concentrations at 6 other wavelengths (Magee Scientific, Model AE-42). The instrument was customized at LBNL with LEDs at 370, 430, 470, 520, 590, 700 and 880 nm, and was operated with a flow rate of 2.4 L/min with one-minute reporting periods.
Filters	Filters were used for measurement of PM mass concentrations of ETS or diesel exhaust particles over short intervals (hours). Air was sampled at 30 L/min through Teflon-coated glass fiber filters 47 mm in diameter. The filters were equilibrated for 24 hr at 38% RH at 70-72 °C before being weighed on an electronic microbalance. This instrumentation produced the measurement defined as $\text{PM}_{\text{grav}}$ , whose units are $\mu\text{g/m}^3$ . PM mass collected by the filters was measured with a Microbalance ( $\pm 1 \mu\text{g}$ resolution, Cahn Automatic Electrobalance, Model 21).

The FBAR was biased by Hewlett Packard power supplies (typically  $V_{dd} = 3 \text{ V}$ ,  $V_n = 0.7 \text{ V}$ , and  $V_p = 1.2 \text{ V}$ ) connected to the MEMS PM PCB board through Molex connectors. The FBAR frequency was monitored with a spectrum analyzer (Hewlett-Packard Model 8562EC) connected with a USB / GPIB cable to a laptop running a customized Labview program. The oscillator center frequency and output power was measured every minute for periods of up to several weeks. The spectrum analyzer was configured with a span of 200 kHz around the center frequency and with a resolution bandwidth of 1 kHz, video bandwidth of 1 kHz, and



waveform averaging over 100 periods. For acoustic isolation, the FBAR resided on a vibration table suspended from the ceiling with elastic cables.

#### 4.1.2 Generation of Challenge Aerosols

ETS from a popular brand of cigarette was generated inside the environmental chamber by an LBNL-built, automated smoking machine (Figure 4.2a and Figure 4.2b) that could light, burn and extinguish up to 16 cigarettes, sequentially, one at a time, under computer control.

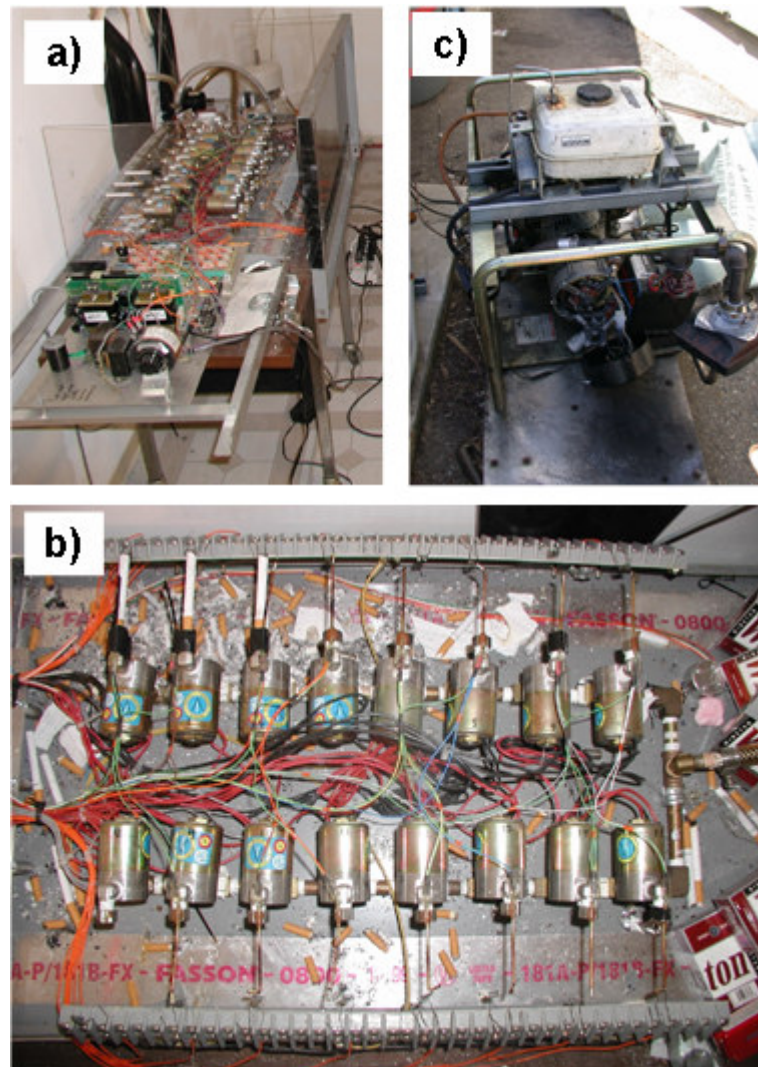


Figure 4.2: Photographs of (a),(b) smoking machine and (c) diesel generator.



The smoking machine was connected to a pump (A. D. Little, Inc.) that drew 35 cm<sup>3</sup> of mainstream smoke once a minute, using a puff profile that simulated human cigarette smoking. The mainstream smoke was ventilated outside the chamber.

The QCM and OPC were located in the chamber with the FBAR or the assembled MEMS PM monitor during most of the experiments in which ETS was the challenge aerosol. The chamber was closed and not ventilated until at least 15 hours after the cigarette smoking ceased. Previous work with ETS in an adjacent chamber<sup>2</sup> and in the same chamber<sup>3</sup> showed that the diameter of ETS particles ranges between 0.1 and 0.2  $\mu\text{m}$  immediately after emission, and showed that, as the ETS aged and deposited on the chamber surfaces, there was never appreciable particulate mass with diameters greater than 1  $\mu\text{m}$ . Similar size distributions were observed in this project. Our results also showed that, as expected for a sealed, unventilated chamber, infiltration of ambient PM into the chamber was very slow. Therefore, during the chamber experiments, a PM<sub>2.5</sub> size-selective inlet was not used for the MEMS PM monitor or filter sampling.

Several experiments used diesel exhaust as the challenge aerosol. Fresh diesel exhaust was admitted into the chamber through a dedicated 5-cm-diameter supply line that tapped a portion of the undiluted exhaust from a portable diesel-powered generator (Acme Motor 80X-300) situated outside the building. Figure 4.2b is a photograph of the generator. Here, a small blower drove the exhaust into the chamber while ambient air was supplied to the chamber through the ventilation system. The amount of dilution and extent of equilibration of the diesel PM were

not measured. During the diesel experiments, the QCM and OPC acquired particle size distributions and PM was collected on filters for gravimetric determination of PM concentration.

#### **4.1.3 MEMS PM FBAR Mass Sensor Packaging**

Views and schematics of the MEMS PM mass sensing module appear in Figure 4.3. In actual use, the monitor is oriented so that the airflow is directed vertically against the force of gravity. The bottom of the 500  $\mu\text{m}$  tall flow channel is formed by a piece of thin brass stock with a 2 x 2.4 mm aperture aligned above the FBAR array (Figure 4.3c). In the vicinity of the FBAR, the top of the flow channel is formed by the quartz / polysilicon heater chip, while elsewhere the lid is formed by two machined brass pieces. The channel sidewalls were defined by two spacers machined from brass stock.

As shown in Figure 4.4, an array of four mass-sensing FBARs are mounted with silicone on top of the CMOS oscillator chip, which in turn is glued to the PCB (Figure 4.5). The brass components are fastened to the PCB with 12 bolts and nuts. The quartz / polysilicon heater chip is aligned directly above the FBAR array and precipitates air-laden PM through the aperture onto the FBAR. Once assembled, all joints are sealed with a bead of silicone to form an airtight flow channel.

In the initial optical design of Figure 4.3e, IR and UV LED beams were designed to pass through the quartz heater and reflect off the PM-coated FBAR array. The reflected light would be captured by the photodetector at the top of the assembly. As will be described later, due to excessive light scattering, this initial module was discarded in favor of a design that situates the LEDs adjacent to the

FBARs, directly underneath the TP heater array. In this configuration, PM deposits directly onto the LED (or onto an optically transparent cover), and all radiated light is attenuated by the deposited PM.

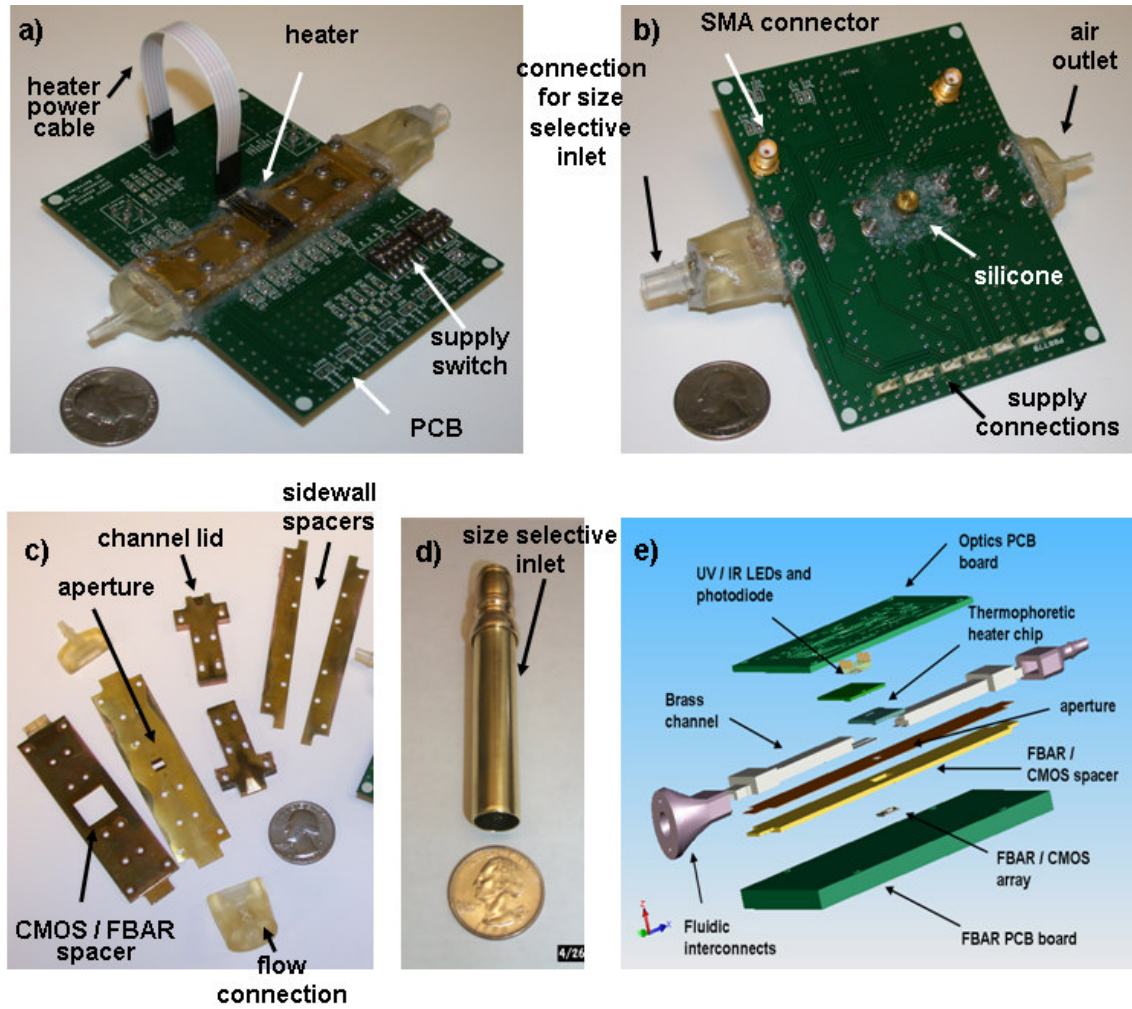


Figure 4.3: (a) Photograph of the top of the assembled MEMS PM mass sensor; (b) photograph of bottom of the assembled MEMS PM mass sensor; (c) photograph of disassembled brass components and plastic flow connectors; (d) photograph of size-selective inlet; (e) SolidWorks exploded view of MEMS PM sensor packaging and components.

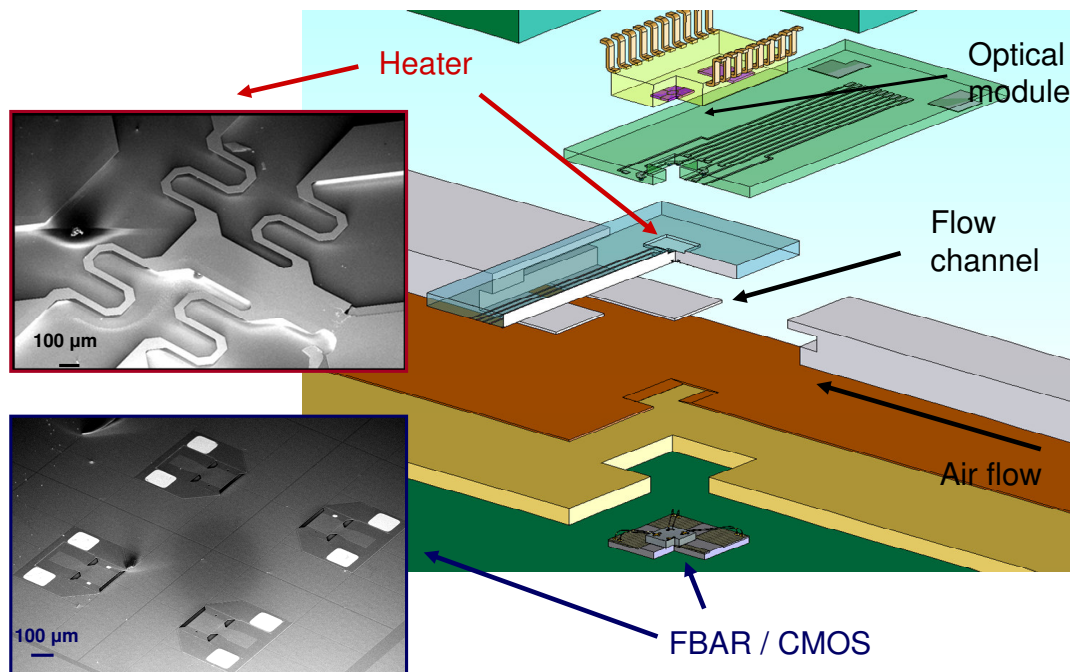


Figure 4.4: SolidWorks rendering depicting alignment and packaging of MEMS PM components, and SEMs of the four-element heater and FBAR arrays.

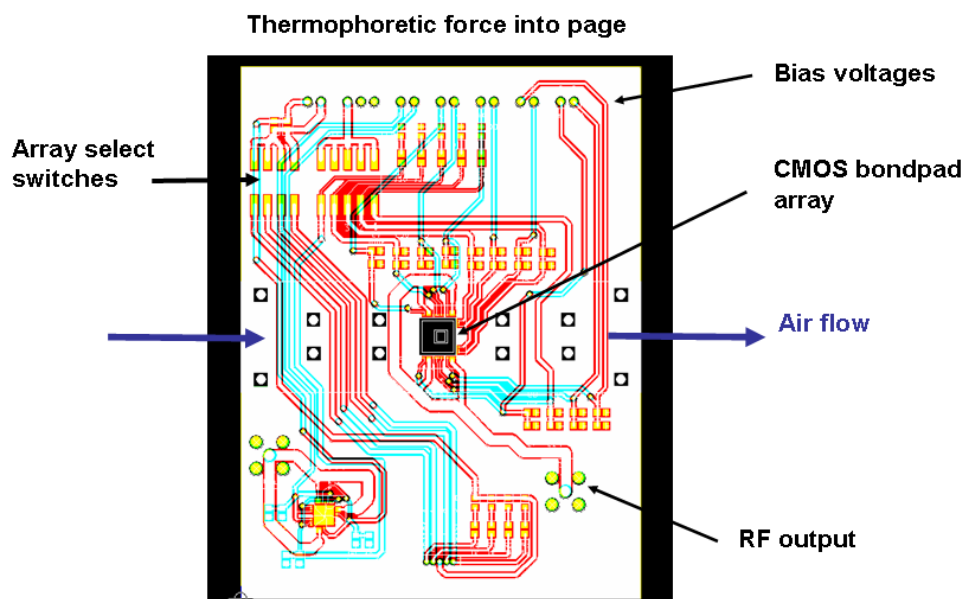
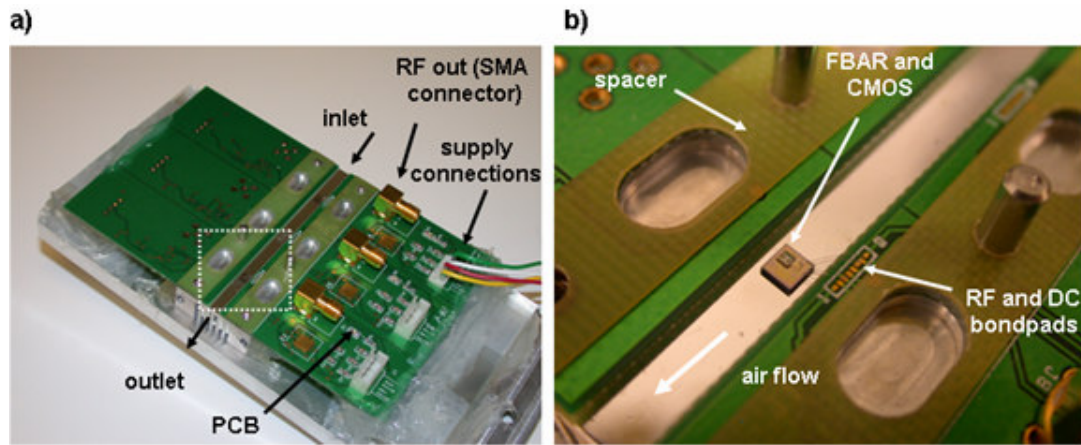


Figure 4.5: Orcad layout of MEMS PM PCB board. The thermophoretic force is into the page; air flow is directed in the plane of the page from left to right.

## 4.2 ETS Detection with MEMS PM Prototype

Early in the project, a proof of concept FBAR PM detection experiment was performed employing an Agilent 1.9 GHz FBAR and a preexisting LBNL sampler customized for interfacing with the FBAR. Figure 4.6 shows photographs of the sampler, which was originally employed for optical interrogation of aerosol deposits as part of the Tobacco Related Disease Research Program (TRDRP) at LBNL<sup>2</sup>.



*Figure 4.6: (a) Photograph of CMOS / FBAR integrated into preexisting LBNL sampler; (b) magnified photograph of dotted box in (a). The two PCBs and spacers define the flow channel sidewalls and a polished aluminum block forms the bottom surface of the channel. The Agilent FBAR and 2.4 mm x 2.4 mm CMOS were glued with cyanoacrylate the bottom of the channel. DC and RF connections were made through bondwires to the PCB. The channel lid with TP wires aligned over the FBARs is not shown.*

The Agilent FBAR was mounted on a 2.4 x 2.4 mm, 0.25  $\mu\text{m}$  process CMOS chip that was in turn glued (with cyanoacrylate) onto the polished aluminum holder built for the TRDRP ETS monitor<sup>4</sup>. A special printed circuit board, designed with cutouts to align with the TRDRP holder, and an extra spacer, to provide vertical clearance for the bondwires, defined the 1 mm tall flow channel sidewalls. The CMOS was electrically interfaced to bond pads at the edge of the PCB. A

polymer lid (not shown) with TP heater wires comprised the top of the flow channel. The fine TP wires (California Fine Wire Co., nickel alloy 120), 25  $\mu\text{m}$  in diameter, were wound around small posts protruding from the lid to form a coplanar resistive heater about 7 mm on a side. Three of these heaters were assembled along the length of the channel, forming three separate TP collection regions. After assembly, a voltage was applied across one of the three wire circuits to form a thermal gradient between the wire and the FBAR. ETS in air was drawn through the flow channel at a rate of 15  $\text{cm}^3/\text{min}$ .

Figure 4.7 shows the FBAR response plotted as the negative time derivative of resonant frequency (right axis) and inferred particle mass concentration from an OPC (left axis). In the experiment, six cigarettes were smoked over a two-day period: two on the afternoon of the first day, one in the morning of the second day, followed by three in the afternoon. Figure 4.7 shows that the OPC and FBAR agree qualitatively, but the FBAR data were quite noisy. The limit of detection for PM in ETS was about 75  $\mu\text{g}/\text{m}^3$  at the 15  $\text{cm}^3/\text{min}$  flow rate.

Experimental noise sources (e.g., vibrating supply wires) seen in this experiment were largely eliminated by mounting the device on a vibration table and filtering the mass sensor output data. As noted earlier, this experiment employed an AIN FBAR manufactured by Agilent, Inc.; all subsequent FBAR data were taken with AIN FBARs manufactured in the UC Berkeley Microfabrication Facility.

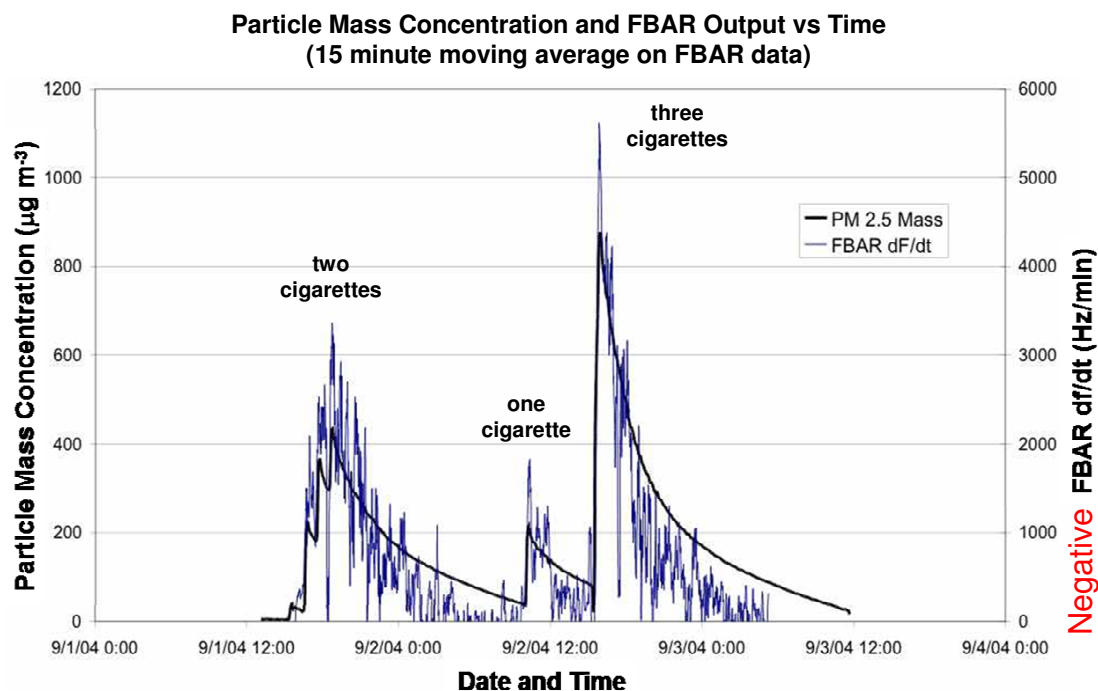


Figure 4.7: FBAR response to ETS produced by several cigarettes. The particle mass concentration was inferred from OPC data.

### 4.3 Calibration of the MEMS PM in the LBNL Environmental Chamber with ETS

A data processing routine was developed by Dr. Michael Apte to smooth the FBAR data and compensate for temperature-induced frequency shifts. Figure 4.8 illustrates the correction routine for FBAR mass sensor data collected during a chamber experiment with one cigarette. Data were post-processed using the R language ([www.r-project.org](http://www.r-project.org)). Figure 4.8a and Figure 4.8b plot the raw FBAR frequency and temperature data as a function of time. In the absence of particles (sampling pump off) and with the thermophoretic heater on, the FBAR temperature coefficient of frequency (57.8 kHz/°C in this example) was first estimated from the FBAR oscillator frequency shift due to ambient temperature fluctuations. FBAR frequency data were temperature adjusted (Figure 4.8c) by subtracting the



temperature-induced frequency component (temperature shift times the TCF). Finally, the derivative of the FBAR oscillator frequency with respect to time, calculated by dividing each measured frequency step by the measured time step, was calculated and filtered (Figure 4.8d) with a smoothing algorithm (R language Supersmooth algorithm with 10% span).

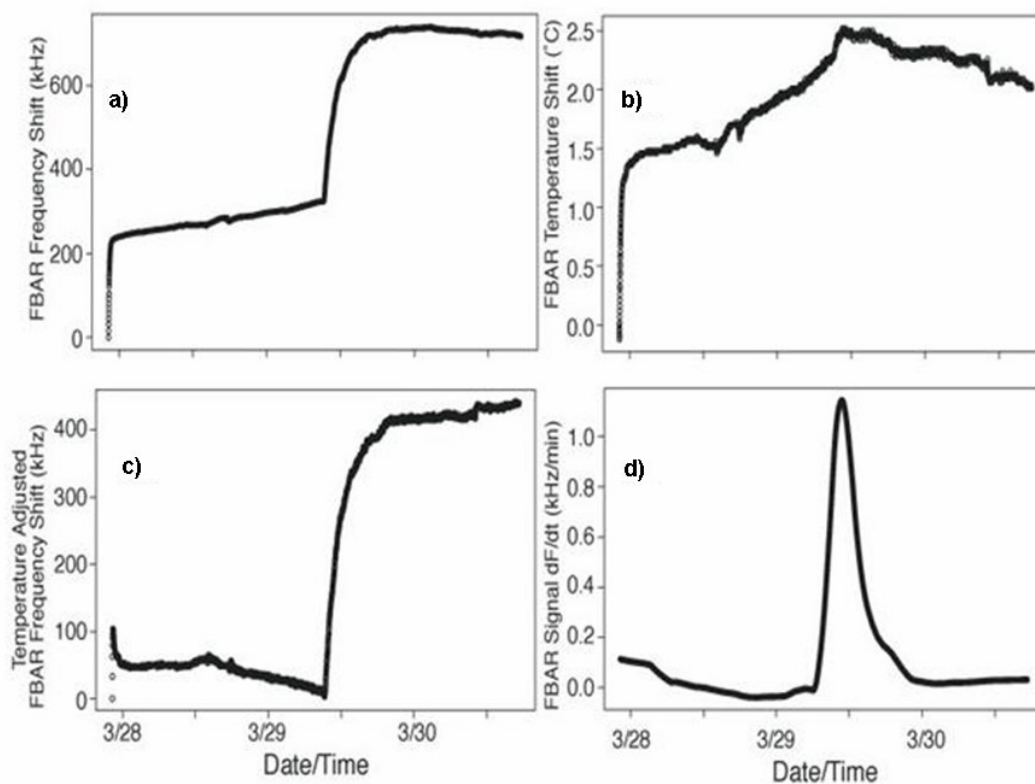


*Figure 4.8: Procedure for removing temperature-induced frequency shifts from the FBAR oscillator frequency and temperature data: (a) FBAR output frequency vs. date/time; (b) temperature shift vs. date/time measured with a thermocouple; (c) FBAR frequency shift after subtraction of the temperature-induced component; and (d) negative of time derivative of frequency after filtering with the R-language Supersmooth algorithm.*

Upon satisfactory reduction of FBAR noise sources and temperature normalization, tests were conducted with the QCM operating in an uncalibrated mode as a reference to determine whether the FBAR output was tracking the ETS



concentration profile. Uncalibrated QCM data taken during the experiment of Figure 4.8 is plotted in Figure 4.9. Since the QCM was operated in an uncalibrated mode, its concentration data are normalized and shown relative to the peak concentration. The air flow rate through the MEMS PM monitor was  $1.5 \text{ cm}^3/\text{min}$ . Good qualitative agreement is evident, though it remains unknown at this time whether the apparent time lag in the FBAR response with respect to the QCM is real or is an artifact. This experiment established that the FBAR response was proportional to a PM mass signal, but did not provide any calibration information for the MEMS PM monitor.

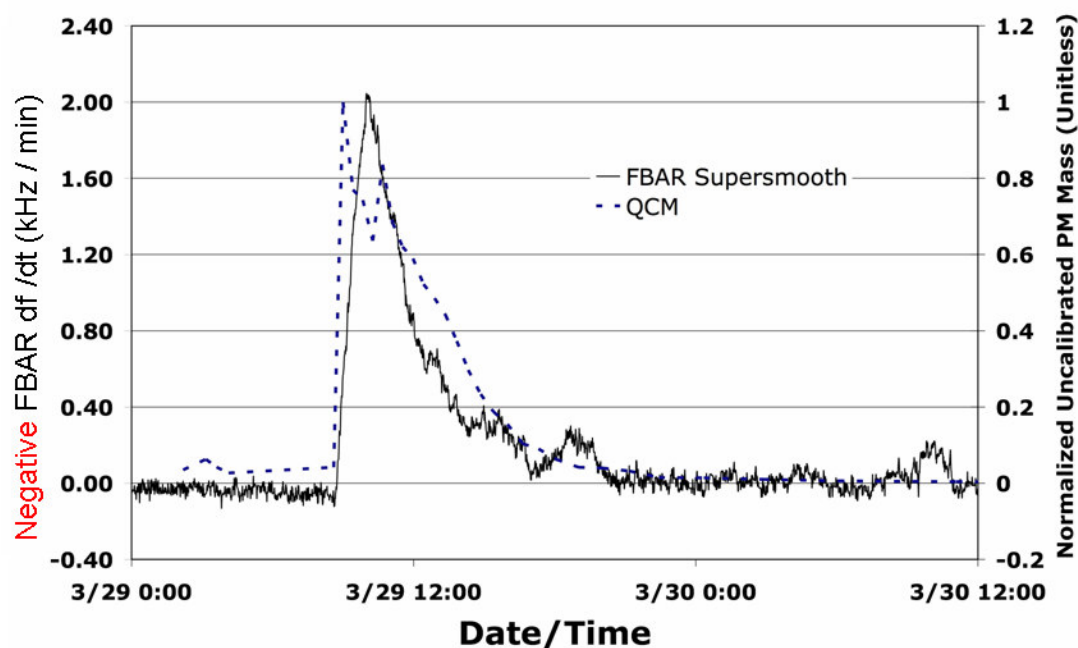


*Figure 4.9: Response of improved FBAR oscillator in the MEMS PM monitor, taken in March 2006, to ETS from one cigarette, along with normalized, uncalibrated QCM mass-sensor data. Time derivatives of sensor resonant frequencies are proportional to real-time concentrations.*

Figure 4.10 compares the response of the MEMS PM FBAR sensor to the QCM when exposed to PM from  $\frac{1}{4}$ ,  $\frac{1}{2}$  and 1 cigarette. Note that the peak QCM

data for one cigarette appears to report low relative to the  $\frac{1}{4}$  and  $\frac{1}{2}$  cigarette data. The reason for this is unknown, but it may simply be that the QCM instrument was beginning to saturate at that point in the experiment. Gravimetric calibration was used in subsequent experiments.

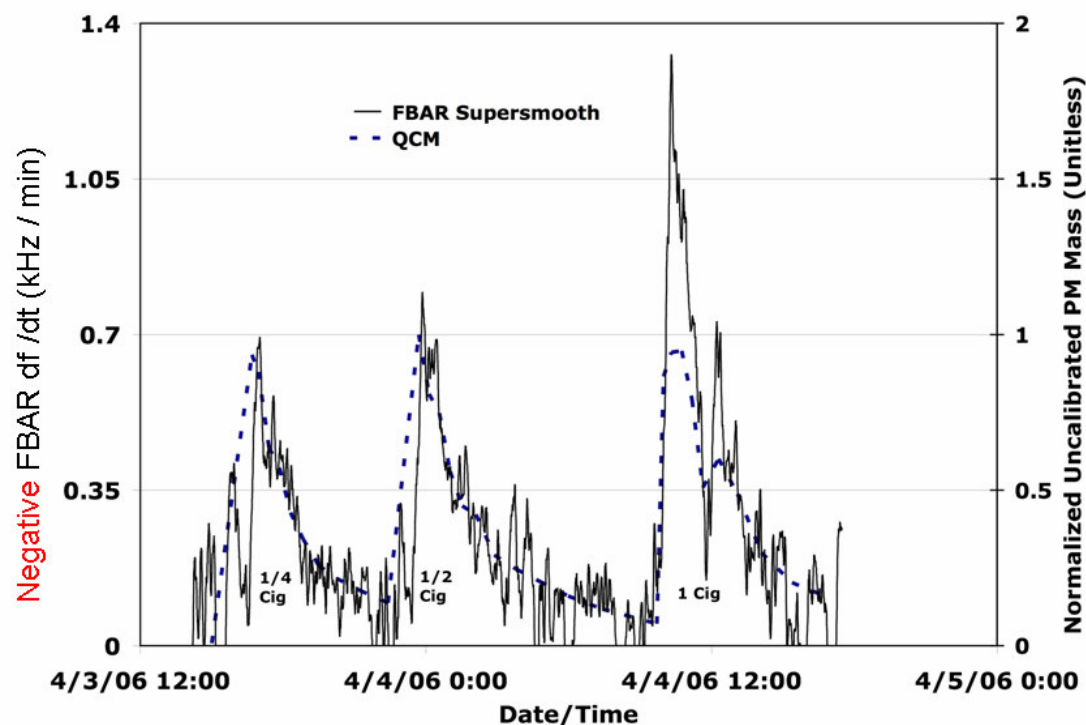


Figure 4.10: Response of the MEMS PM monitor to smoke from one-quarter, one-half and one cigarette, agreeing with profile from normalized, uncalibrated QCM mass-sensor data.

Once it had been established that the FBAR response was proportional to chamber PM concentration, a calibration response factor to convert from the time derivative of the FBAR frequency to PM concentration was measured experimentally. The MEMS PM monitor mass response was correlated with PM mass concentrations determined gravimetrically ( $PM_{grav}$ ) from sampling ETS over short intervals on two Teflon-coated fiberglass filters in series (Figure 4.11). The

method for  $PM_{grav}$  was adapted for sampling ETS and diesel exhaust in the LBNL environmental chamber from the Federal Reference Method (FRM)<sup>5</sup>. The adaptations to the method for use in this project were:

- 1) sampling over periods of several hours, rather than 24 hours;
- 2) not using a  $PM_{2.5}$  size-selective inlet because ETS does not generate particles as large as  $2.5\ \mu m$ , and the ambient PM contribution to the total PM in the chamber was negligible during the experimental work with ETS; and,
- 3) use of a second inline filter because the filter manufacturer's information indicated that 5% of particles with diameters of  $0.3\ \mu m$  and below penetrate, and the mass median diameter of ETS is  $\sim 0.2\ \mu m$ .

The resulting calibration of the MEMS PM monitor (Figure 4.12) showed that the temperature-compensated  $df/dt$  signal of the FBAR mass sensor, integrated over the same time period as the filters, was indeed proportional to  $PM_{grav}$  at least up to concentrations of  $400\ \mu g/m^3$ . The calibration factor based upon these data is  $400\ \mu g/m^3$  per kHz/min change in FBAR frequency.

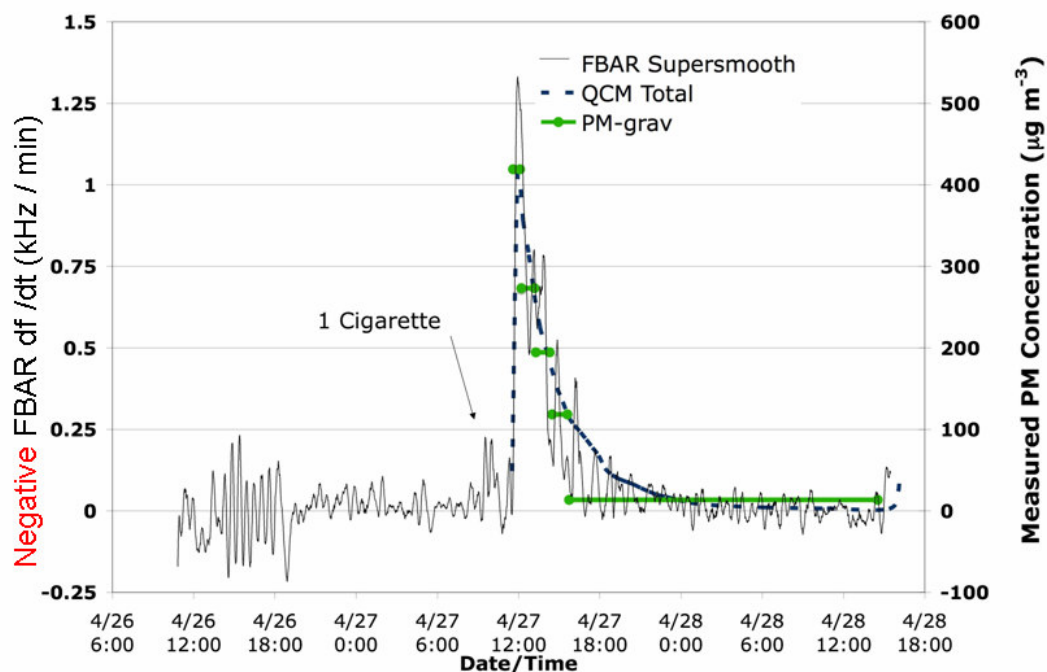


Figure 4.11: MEMS PM monitor response to ETS from one cigarette, along with PM concentrations from the calibrated QCM and weighed filters ( $PM_{\text{grav}}$ ).

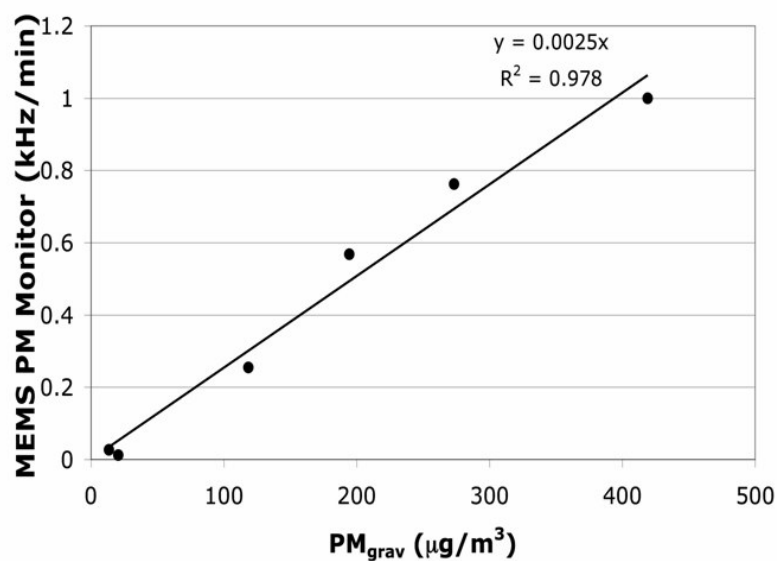


Figure 4.12: Calibration of MEMS PM monitor based on environmental chamber experiments. Relationship between the time derivative of the FBAR signal and  $PM_{\text{grav}}$  for the data shown in Figure 4.11.

#### 4.4 MEMS PM FBAR Sensor Response to Fresh Diesel PM

Figure 4.13 compares the response of the MEMS PM mass sensor to the OPC, the QCM, and  $PM_{grav}$  in response to fresh diesel exhaust PM. Generation of the diesel exhaust was described earlier in Section 4.1.2. The generator operated for 24 minutes, starting at 15:51 on 4/28/2006, and throughout the experiment the environmental chamber remained unventilated. The 3-hr average  $PM_{grav}$  concentration measured from filters immediately after introduction of the diesel was  $427 \mu g/m^3$ . Over the same period, the concentration of black (elemental) carbon measured by the Aethalometer ranged from 430 to  $120 \mu g/m^3$ . The 0.05 and 0.10  $\mu g$  stages of the QCM overloaded after its first measurement cycle, leading to underestimation of the mass concentration by the QCM.

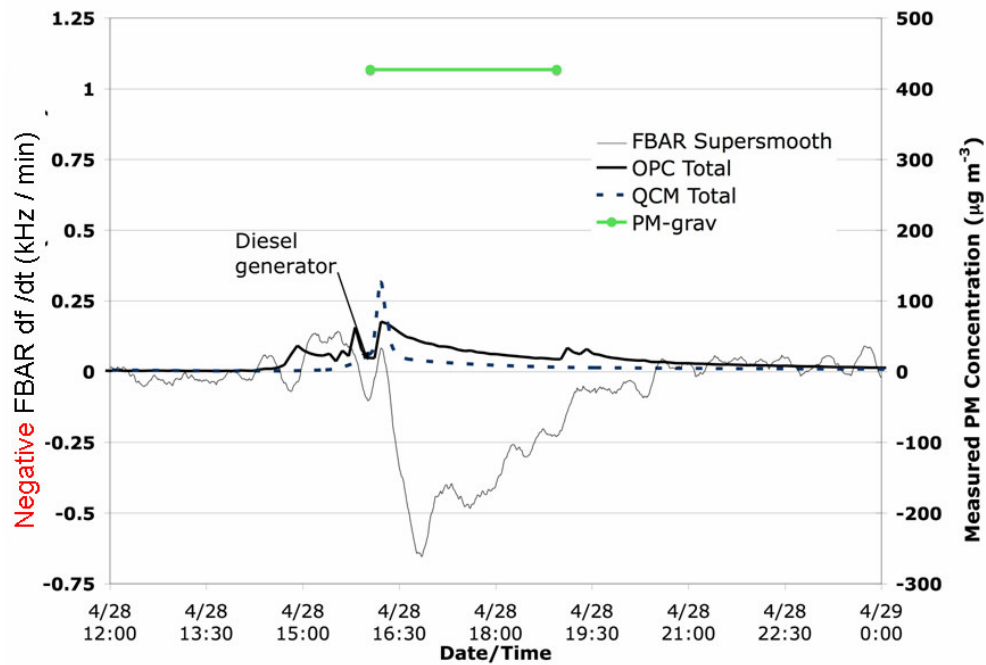


Figure 4.13: MEMS PM monitor response to fresh diesel exhaust in the environmental chamber, along with data from the OPC and QCM.

Figure 4.13 shows that in response to the diesel PM the MEMS PM monitor exhibited an anomalous response – the resonant frequency rose as the deposited mass increased. The total positive frequency shift was  $\sim 180$  kHz. The observed behavior can be explained by noting the conductive diesel PM film introduces a resistance in parallel with  $C_o$  of the FBAR. This effect may be modeled by the addition of  $R_d$  across the FBAR electrodes, as shown in Figure 4.14. The impedance of the feedback circuitry across M1 then becomes:

$$Z_x = R_3 \parallel \left[ 2sL_{par} + \frac{R_d \left[ s^3 C_o R_p L_x C_x + s^2 (L_x C_x + C_o C_x R_p R_p) + s (C_x R_x + C_o R_p) + 1 \right]}{s^3 L_x C_x C_o (R_d + R_p) + s^2 [L_x C_x + C_x R_x C_o (R_d + R_p) + C_x R_d C_o R_p] + s [C_o (R_d + R_p) + C_x R_3 + C_x R_x] + 1} \right] \quad \text{Eq. 4.1}$$

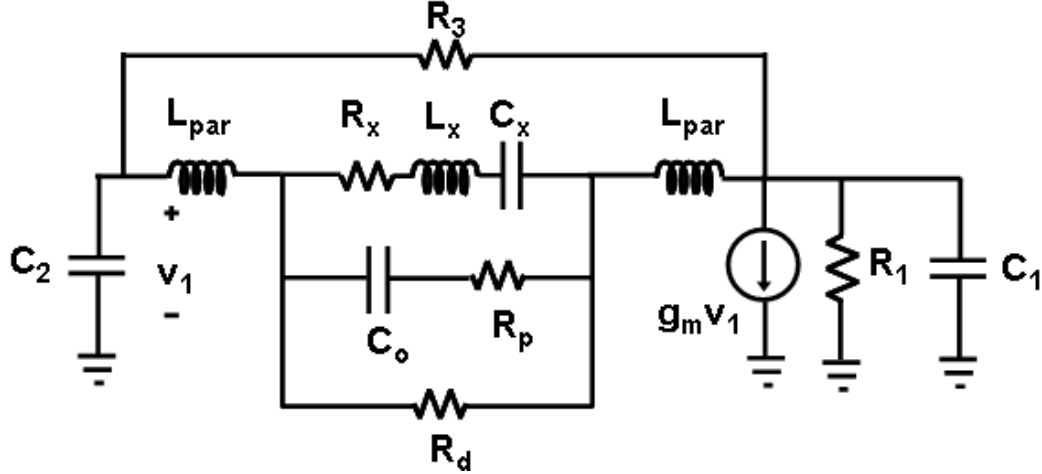


Figure 4.14: Small-signal oscillator model where  $R_d$  models the effect of the conductive diesel film deposited in the vicinity of the FBAR.

For the FBAR oscillator studied in Chapter 3.6.2 with  $V_{gp} = 1$  V, Figure 4.15a plots the change in oscillation frequency as a function of the diesel film resistance shorting the FBAR leads. Based on Figure 4.15a and the measured 180 kHz frequency shift, the estimated resistance of the diesel film,  $R_d$ , is 18 k $\Omega$ . Assuming a resistivity for the diesel film of 0.5  $\Omega\text{-cm}^6$  and, based on the FBAR bond-pad layout, an effective area of 200  $\mu\text{m} \times 400 \mu\text{m}$  for the diesel film resistor,

ones estimates the thickness of the diesel film to be 139 nm, which is physically reasonable.

Figure 4.15b plots the trajectory of one complex unstable pole as a function of the resistance of the diesel film. The oscillator cuts-off for  $R_d$  less than 2.7 k $\Omega$ , which corresponds to a diesel PM film thickness of 926 nm. For a given  $g_{m1}$ , the diesel exhaust particles reduce the oscillator output power and simultaneously increase of the oscillator frequency.

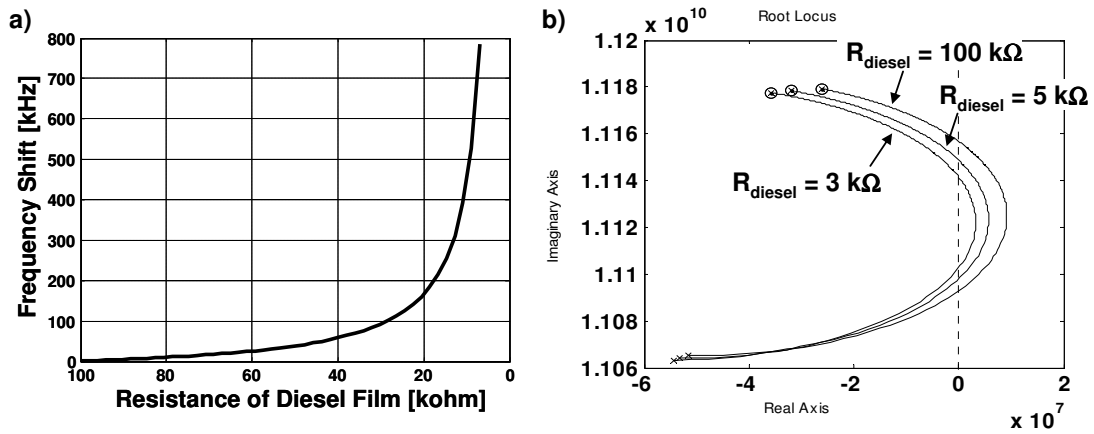


Figure 4.15: (a) Calculated shift of FBAR oscillator resonator frequency (positive) as a function of the resistance of the diesel PM film shorting the FBAR leads ( $R_d$ ); (b) trajectory of complex oscillator pole shown for three values of the diesel PM film resistance. For parasitic resistance less than 2.8 k $\Omega$ , oscillation ceases.

There are two ways to eliminate this problem: (1) shield the FBAR electrodes and bond wires from particles with a small drop of epoxy, or (2) use a bulk-micromachined fabrication process in which the active FBAR surface and the connecting electrodes are formed on opposite sides of a released membrane that supports the piezoelectric resonator. However, with proper sensor design, this anomalous response could be useful for detection of differences in concentration of conducting and non-conducting ultrafine aerosols and nanoparticles.

#### 4.5 Discrimination of PM Composition by Thermal Spectroscopy

The study of polymer dynamics with acoustic-wave devices is well documented in the literature<sup>7</sup>. This Section describes a preliminary study on the behavior of an AlN FBAR oscillator coated with thermally precipitated ETS as a function of temperature. The MEMS PM FBAR mass sensor was placed in an incubator and the oscillator output spectrum was monitored as the temperature was varied. Figure 4.16a shows the change in oscillator frequency as the temperature increased from 23 to 70 °C, where the temperature-induced FBAR frequency shift has been subtracted following the procedure of Figure 4.8. Beginning at 50 °C, the oscillator frequency increases and then decreases, due to what is believed to be the glass transition of ETS at temperature  $T_g$ . In the vicinity of a polymer's  $T_g$ , the bulk modulus and complex (bulk loss) modulus can decrease and increase, respectively, by several orders of magnitude<sup>8</sup>. Unfortunately, data on the elastic properties of thermally precipitated ETS was not available from the literature, but, based on its molecular composition, is believed to be similar to paraffin wax<sup>9</sup>.

As shown in Figure 4.16b, between 50 and 58 °C the quality of the oscillator output spectrum deteriorated (marked by peak broadening and frequency drift), suggesting an increase in the motional resistance of the coated FBAR. In fact, at some bias voltages, the oscillation ceased altogether. Above 58 °C, the oscillator spectrum restabilized but the output power dropped several dBm.



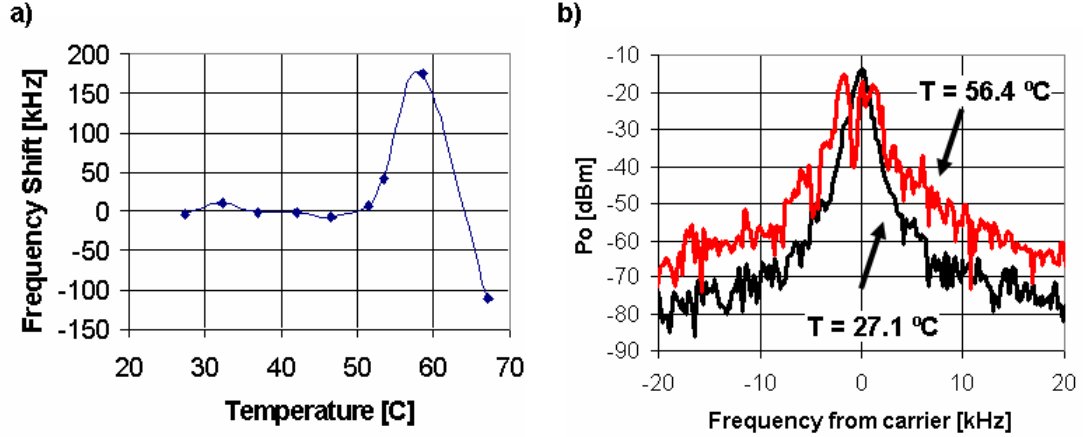


Figure 4.16: (a) FBAR oscillator frequency shift as a function of temperature; (b) oscillator output spectrum at 27.1 and 56.4 °C.

An analysis of ETS film dynamics subject to variable bulk modulus suggests several explanations of the resonator behavior observed between 50 and 60 °C. First, the hypothesized increase in the complex bulk loss modulus of the ETS film causes energy dissipation and directly increases the resonator motional resistance. Second, a decrease in the ETS bulk modulus would decrease the acoustic wavelength in the film. If the acoustic wavelength in the film is much larger than the film thickness, the added layer moves synchronously with the FBAR and the strain within the film is small. However, if the total acoustic phase shift in the film approaches  $\pi/2$  (a  $\pi/2$  phase shift corresponds to a film thickness of one-quarter wavelength), the film undergoes a resonance condition where the particle motion at the top of the film is 180° out of phase with the FBAR-film interface. Under this condition, there is significant elastic energy storage and loss within the film which increases in the resonator motional impedance. Figure 4.17 illustrates how, because of film resonance, an oscillatory frequency shift can be produced by sweeping the

bulk modulus of a 378 nm film on a 1.7 GHz FBAR ( $\rho_{film} = 0.8 \text{ g / cm}^3$ ). Due to time constraints, the dynamics of the ETS loaded FBAR were not explored further.

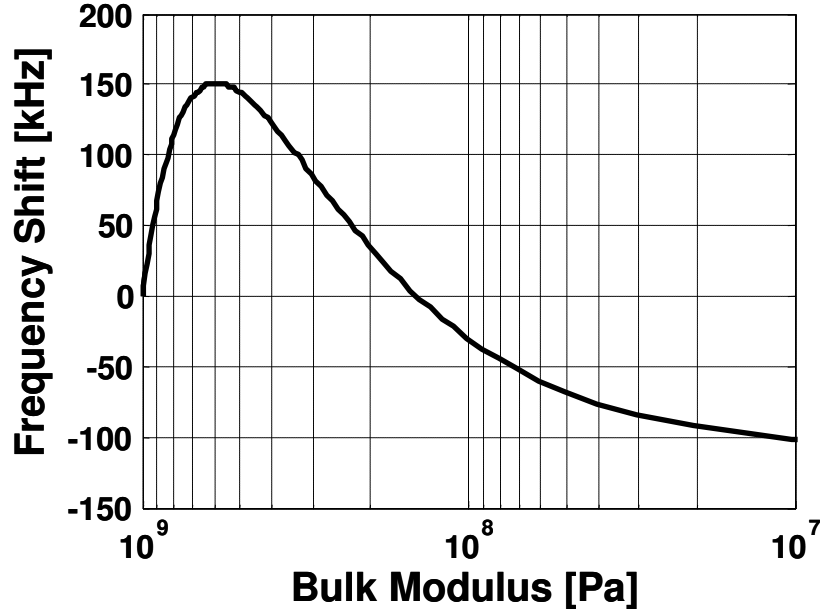
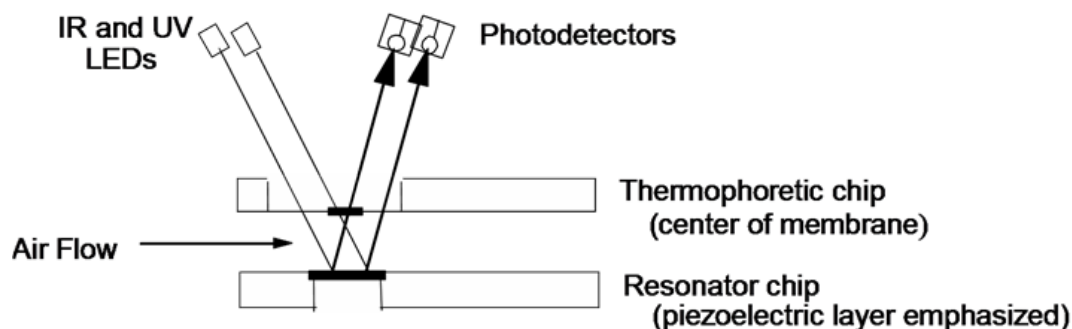


Figure 4.17: Frequency shift as a function of bulk modulus for a 378 nm film on a 1.7 GHz AlN FBAR.

#### 4.6 Discrimination of PM Composition by Optical Interrogation

A key feature of the MEMS PM monitor is the measurement of PM light absorption to obtain information about PM composition. Prior work at LBNL<sup>3</sup> has shown that such optical testing using two (or more) wavelengths can yield information about the chemical nature of the deposit. Figure 4.18 shows conceptually how UV and near-IR light reflected from the FBAR deposit would be monitored by photo-detectors in a ‘reflectance’ configuration. The change in absorbance depends on the thickness and chemical composition of the PM deposit.

## One of a plurality of resonators and TP sources



*Figure 4.18: Concept of simultaneous mass measurement and optical characterization of the deposited PM with one resonator mass-sensing chip and a pair of LEDs and photodetectors for optical characterization of the deposited particles.*

The grey or black appearance of ambient PM is due primarily to the presence of black carbon (BC), most commonly emitted from combustion of fossil fuels. BC absorbs light like a black body throughout the UV, visible and IR spectral regions, and its absorption coefficient varies inversely with wavelength. At 370 nm, a black body absorbs 2.4 times more strongly than at 880 nm ( $880/370 = 2.4$ ). Figure 4.19<sup>4</sup> shows that diesel PM in ambient air absorbed UV at 370 nm  $2.3 \pm 0.1$  times more strongly than IR at 880 nm, indicating that diesel PM absorbs light like a black body. For ambient PM the ratio of UV(370) to IR(880) was  $1.9/0.85 = 2.2 \pm 0.3$ , as expected.

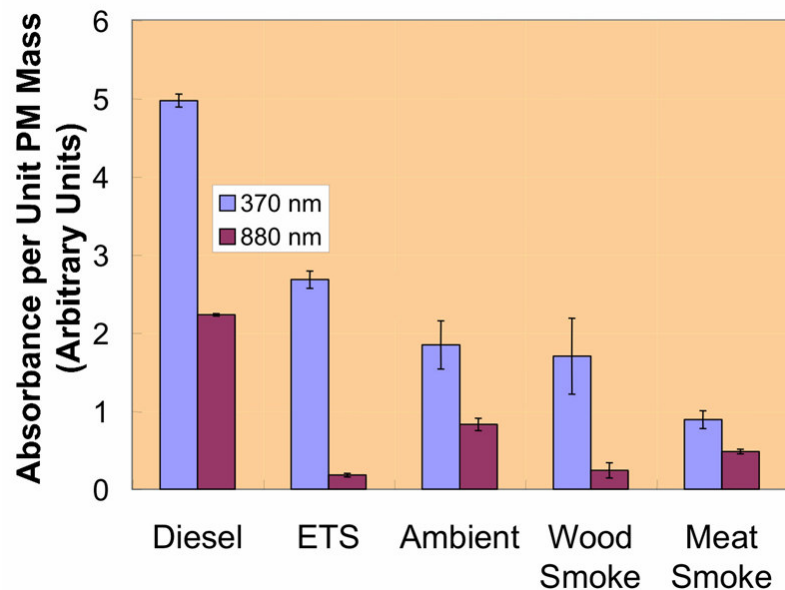
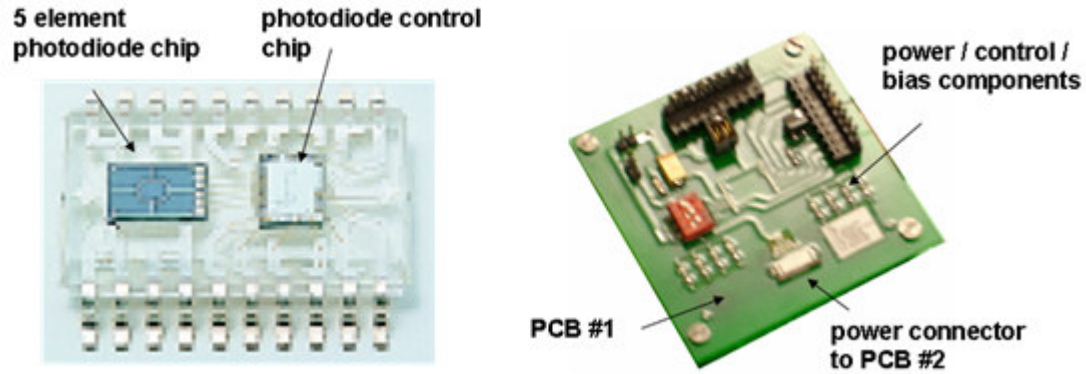


Figure 4.19: Comparison of absorbances in the UV and near-IR for combustion sources that generate airborne PM. At the center of the chart labeled “Ambient” are absorbances of PM collected in Berkeley, CA<sup>4</sup>.

#### 4.6.1 Reflectance-Based Optical Module

A printed-circuit board (PCB) module consisting of a Hamamatsu 5-element photodiode (S6840) and UV (395 nm) and IR (810 nm) LEDs was designed, assembled, and tested (see Figure 18). A key advantage of this particular make of photodiode was its spectral sensitivity to both UV and IR light. The geometry of the four-element FBAR array was designed to align specifically to the photodiode array, with one FBAR per quadrant (the fifth centered, photodiode element was not specific to any one FBAR).



*Figure 4.20: (a) Hamamatsu S6840 photodiode with 5-element sensor array; (b) photograph of optical module PCB #1.*

As shown in Figure 4.20b and Figure 4.21, PCB #1 supports the photodiode and control electronics while a second, thinner PCB (#2) was carefully aligned to the photodiode and attached with glue. As seen in the figure, PCB #2 had a window cut into it which aligned to the photodiode chip, as well as pads and electrical traces (anode and cathode) for  $300\text{ }\mu\text{m} \times 300\text{ }\mu\text{m} \times 500\text{ }\mu\text{m}$  UV and IR LEDs. The UV and IR LEDs were attached with conductive epoxy. The inset perspective view shows the 5-element photodiode array through the window in PCB#2.

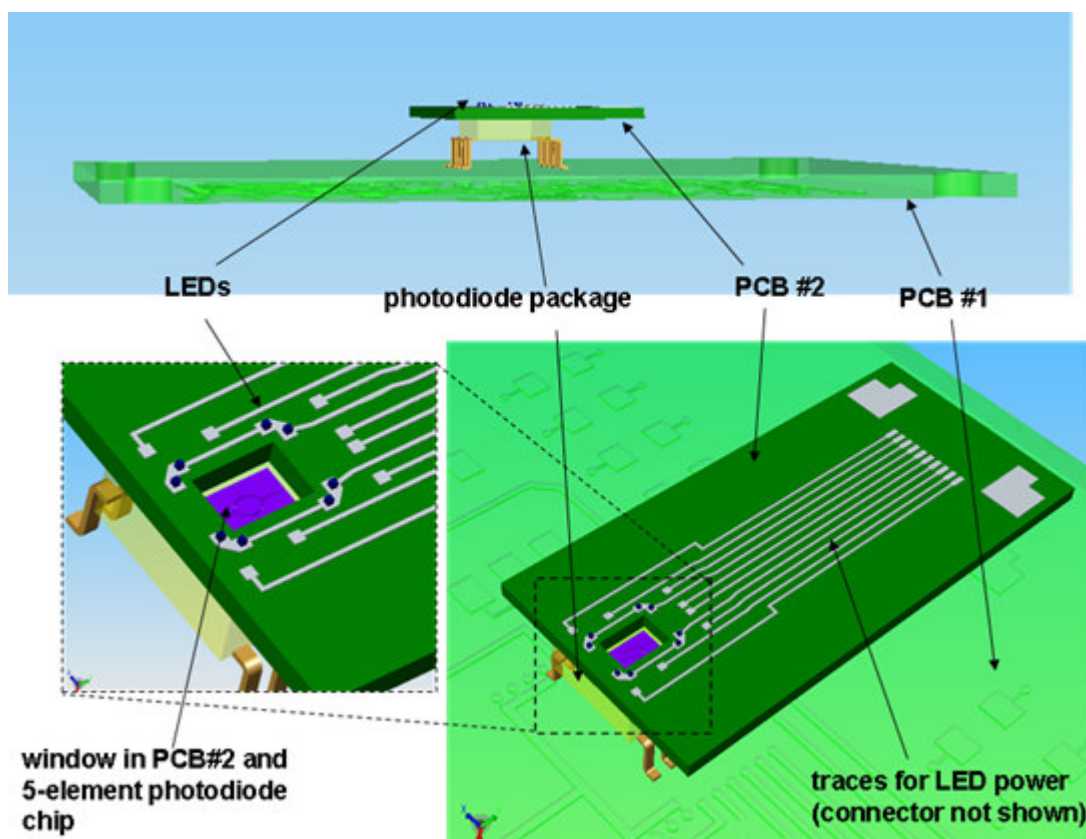
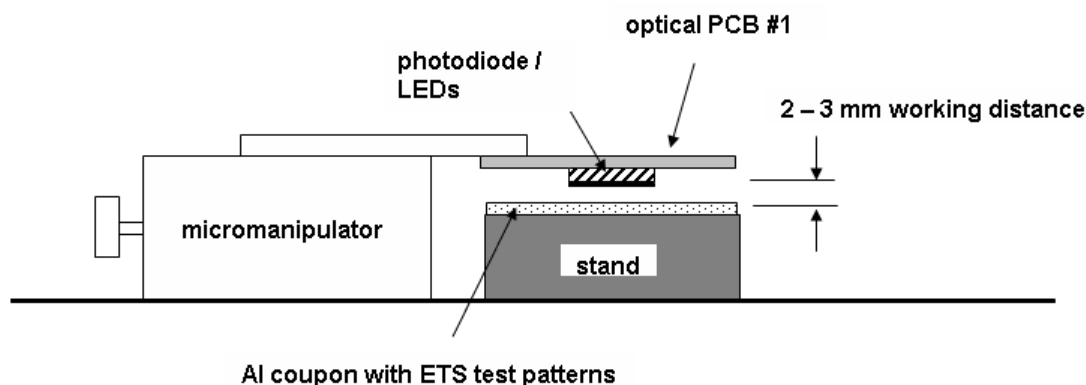


Figure 4.21: Side and perspective views of the optical module (created in SolidWorks by Dr. Rossana Cambie).

Ideally, light emitted from the LEDs reflects off the FBARs and returns through the window in PCB #2 for measurement by the photodiode. To establish a baseline for operation of the optical module, the assembled module was first tested using ETS films deposited onto a highly reflective aluminum surface (200 nm of aluminum evaporated onto a silicon wafer). A linear array of ETS test patterns was formed by pipetting ethanol with dissolved ETS onto the aluminum coupon and allowing the ethanol to evaporate. As shown in Figure 4.22, the window in the optical module was positioned 2 – 3 mm above the aluminum coupon with a micromanipulator. The LEDs and photodiode board were linearly scanned across

the ETS test patterns (out of the page) while the photodiode output voltage was monitored. In this test, the photodiode output voltage was expected to exhibit a spatial dependence that correlated with the position of the ETS test patterns.



*Figure 4.22: Test setup for calibrating the optical module*

Testing showed that light scattered from surfaces of the test fixture and transmitted through PCB #2 overwhelmed the signal reflected from the ETS film on the aluminum coupon. Extensive efforts to overcome noise from scattered light with an AC LED-drive and lock-in-amplifier detection scheme were not successful. An attempt to coat all surfaces with light-absorbing black paint also proved unsuccessful. Therefore, this first optical module design was discarded in favor of a transmission-based design in which a much higher fraction of the light reaching the photodiode passes through the PM deposit.

#### **4.6.2 Transmission-Based Optical Module**

As shown in Figure 4.23, the transmission-based experiments made use of a modified thermophoretic ETS sampling assembly originally developed for the

TRDRP<sup>4</sup>. PM deposition occurred on a thin glass slide situated just above the surface of the LEDs for measurement by direct optical transmission.

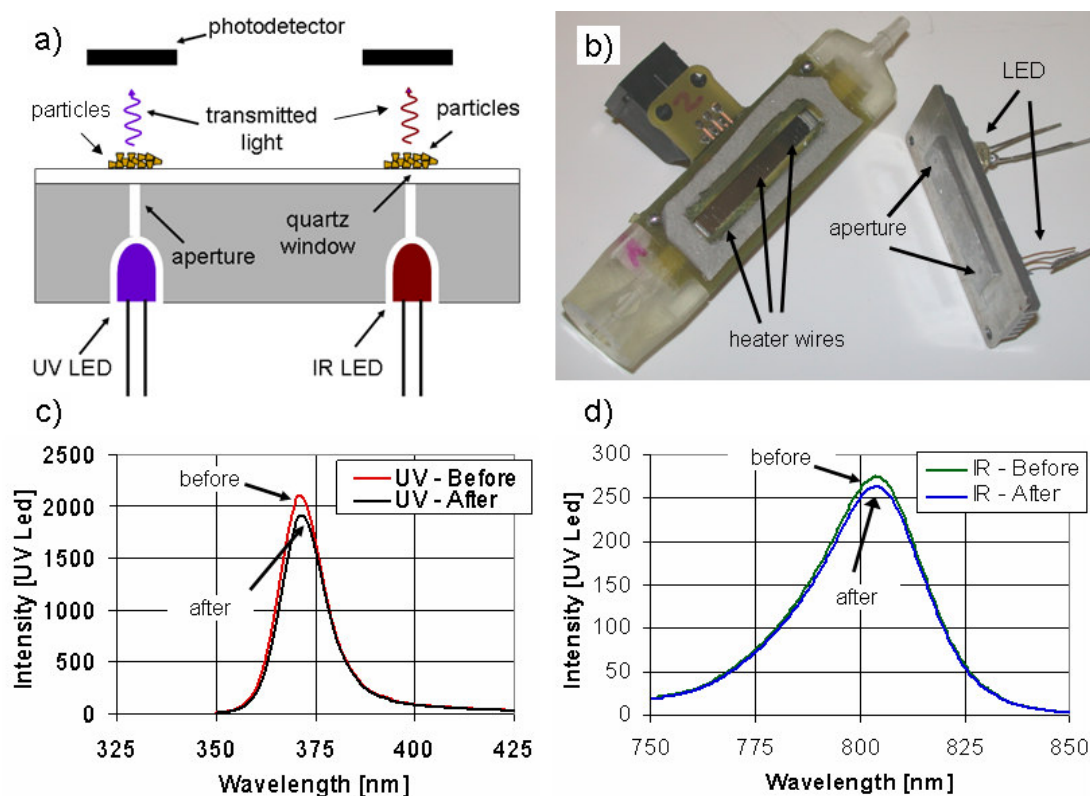


Figure 4.23: (a) Cross-sectional schematic of bottom aluminum casing with IR / UV LEDs and apertures; (b) photograph of the transmission-based optical module consisting of modified ETS sampler; (c), (d) UV and IR transmission characteristics of ETS PM showing differential absorption.

The apparatus for collecting particles consisted of a printed circuit board frame that holds three sets of TP wires, that formed the sides of a flow channel, and that provided a mounting surface for two fin-cooled aluminum PM collection plates. With the Al PM collection plates attached, the device forms an air-tight flow channel with three PM collection areas. A small pump drew PM-laden air through the device at a flow rate of 10 cm<sup>3</sup>/min. Four fine TP wires (California Fine Wire Co., nickel alloy 120) 25  $\mu$ m in diameter and about 5 mm in length were soldered,



physically in parallel and electrically in series, to form a coplanar resistive heater on the collector frame about 5 mm on a side. Three of these heaters were assembled on a single sampler to create three separate TP collection regions (see Figure 4.23b). Application of a voltage to one of the three wire heater circuits created a thermal gradient between the wire and the fin-cooled aluminum collection plate.

A 200  $\mu\text{m}$  thick glass slide was glued to the aluminum collection plate body (see Figure 4.23a) which covered two, 1 mm diameter optical pinholes in the aluminum casing. The pinholes were aligned underneath the two outer TP sources. UV (380 nm) and NIR (810 nm) LEDs, inserted into the back of the aluminum body, transmitted light through the pinholes and any PM film deposited by the TP sources onto the glass slide. A second aluminum body with a reflective surface (not glass) formed the cover on the opposite side of the ETS sampler. Figure 4.23b is a photograph showing the TP ETS sampler and the top Al cover with embedded LEDs.

To characterize the module, eight cigarettes were smoldered simultaneously in the sealed LBNL environmental chamber and ETS PM was collected on the glass surface. After sampling, the components were disassembled and the change in light intensity due to ETS PM was measured with a UV-NIR spectrophotometer (Ocean Optics Inc., Dunedin, FL).

Figure 4.23c and Figure 4.23d show for UV and IR light differential absorption before and after PM deposition. The fractional change in transmission intensity at 375 nm is twice that at 810 nm as expected. The results suggest that the use of absorbance as an alternative to reflection would enable one to quantify the

amount of optically absorbing material thermophoretically deposited in a light path. Due to time constraints, the final integration of LED chips into the MEMS PM monitor was not completed.

#### **4.7 Field Study in Berkeley Residence**

A field study was conducted in a Berkeley residence over two separate periods during May and June of 2006 in order to pursue the following objectives:

- 1) to compare of the time-integrated PM<sub>2.5</sub> concentrations measured with the MEMS PM monitor to filter-based measurements taken over 24- and 4-hr periods (FRM and adapted FRM, respectively);
- 2) to estimate of the limit of detection (LOD) of the MEMS PM monitor for PM<sub>2.5</sub>; and,
- 3) to compare of the response of the MEMS PM monitor to infiltrated ambient air in a residence with the responses from several real-time aerosol instruments.

Analysis of data from the first study (May 2006) strongly suggested that the sensitivity of the FBAR sensor in the MEMS PM monitor had decreased substantially, compared to that when the results of Figure 4.12 were obtained. Two exposures to high concentrations of diesel exhaust may have been the cause. For the second field test (June 2006), a second FBAR oscillator on the same chip was activated. Only data from the June field test are discussed.

#### 4.7.1 Site Description, Instrumentation, and Experimental Methods

The tests were run in a 1200 ft<sup>2</sup>, two-story single-family wood-and-brick dwelling in the Berkeley hills. The instruments used for laboratory studies (described in Section 4.1.1) were set up in the living room according to the floor plan of Figure 4.24. The house had an attic exhaust fan that could draw air from the ceiling of the test area, pulling in outdoor air through the windows and exterior doors near the test equipment.

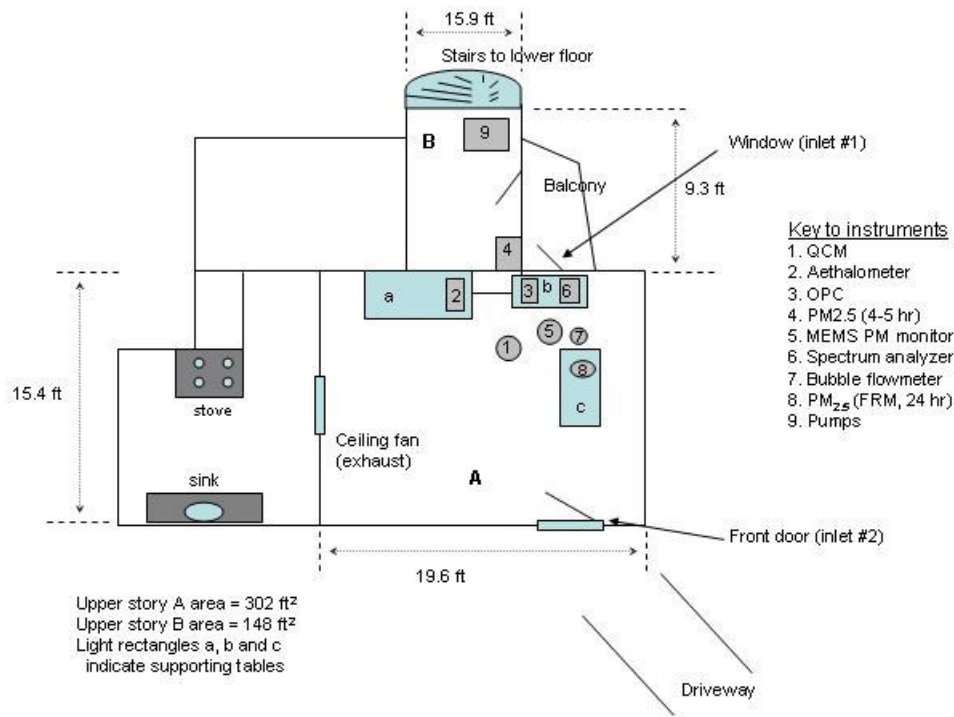


Figure 4.24: Floor plan of house in which field tests were conducted showing locations of instruments, the MEMS PM monitor, and the window and door air inlets.

Two additional experimental methods were used in the field study:

- 1) Average 24-Hour PM<sub>2.5</sub> mass concentrations according to the Federal

*Reference Method:* PM<sub>2.5</sub> was sampled at 16.7 L/min (1 m<sup>3</sup>/hr) onto Teflon

filters (Teflon® membrane, 25 mm diameter, 3 µm pore size, Pall/Gelman, with 99.99% retention of 1 and 2 mm-diameter particles) that clamped into a stainless steel holder. Particles larger than 2.5 µm in diameter were excluded by a Teflon-coated aluminum size selective inlet (URG, Inc.). The filters were equilibrated at RH 38% for 24 hrs before each weighing. A programmable pump (Gilian Aircon-2, Sensidyne) was calibrated frequently, and filters were changed every 24 hr (at midnight).

- 2) *Gravimetric determination of indoor PM<sub>2.5</sub> mass concentrations (µg/m<sup>3</sup>) from particles collected indoors with a High Capacity Integrated Gas and Particle Sampler (Hi-C IOGAPS, URG)<sup>10,11</sup>*: As used in the field study, this sampling method adapted FRM methods for 4-hr, rather than 24-hr, average PM<sub>2.5</sub> concentrations during the periods when infiltrated ambient PM had been intentionally enriched with PM from combustion sources. The high flow rate was necessary because of the low indoor PM concentrations and the short sampling time. The IOGAPS operated with a PM<sub>2.5</sub> inlet (cyclone) and volumetric flow control, and particles were collected on Teflon-coated glass fiber filters (two in series), 90 mm in diameter, equilibrated for 24 hr at 38% RH before weighing on an electronic microbalance. The filter face velocity of the Hi-C IOGAPS at 100 L/min is close to that used to collect PM<sub>2.5</sub> at 16.7 L/min on filters with 47 mm diameter in some versions of the Federal Reference Method for PM<sub>2.5</sub>. The IOGAPS was operated with no denuder (gas strippers) upstream of the filters, therefore semi-volatile organic gases were not removed from the airstream before the particles

reached the filters. The modified IOGAPS sampled PM over 4-hr periods when combustion sources were present outdoors (cigarette smoke or diesel exhaust) or indoors (cooking fumes).

Figure 4.25 is a photographic collage of the aerosol instruments, with the MEMS PM monitor in the center and a typical FBAR resonance curve on the spectrum analyzer to center right.



*Figure 4.25: Field test instrumentation. Top row (L to R): Quartz crystal microbalance (QCM); Aethalometer; optical particle counter (OPC). Middle row: High-flow sampler for measuring episodic source-enriched PM<sub>2.5</sub>; MEMS PM monitor; spectrum analyzer displaying FBAR resonance. Bottom row: Bubble flowmeter for use with MEMS PM monitor; FRM sampler for PM<sub>2.5</sub>; pump and gas meter for FRM sampler.*

#### **4.7.2 Aerosol Monitoring Protocols**

Two aerosol protocols were employed in the field study:

**Protocol 1** Responses to ambient air with windows and doors closed and no nearby combustion sources. The MEMS PM monitor operated continuously, and 24-hr average PM<sub>2.5</sub> concentrations were determined gravimetrically with sampling starting at midnight. The QCM, OPC and Aethalometer operated throughout the field test, but data gaps exist for intervals when the instruments were malfunctioning or overloaded. The FRM was used to collect 24-hr filters for PM<sub>2.5</sub>, from midnight to midnight.

**Protocol 2** Responses to ambient air with an additional nearby indoor or outdoor combustion PM source and with window or door open and the house depressurized slightly with the attic fan operating. The FRM for PM<sub>2.5</sub> was adapted for 4-hr sampling while the combustion sources were operating. The FRM (24-hr gravimetric sampling for PM<sub>2.5</sub>) continued during PM generation. The infiltration rate of source-enriched ambient PM was adjusted based on observed changes in the PM concentrations as registered by real-time instruments, with the goal of adding sufficient PM to roughly double the recently recorded ambient PM<sub>2.5</sub> concentrations.

The building had an air exchange rate of approximately once per hour with the attic fan turned on, about twice that without the fan. Temperature and RH were

monitored in the vicinity of the MEMS PM monitor. Ambient PM was enriched with contributions from PM generated by these sources:

- Cigarette smoke, under Protocol 2. Six cigarettes were lit and smoldered, one at a time, outside a half-open window one meter from the indoor MEMS PM monitor and the other PM monitoring instruments.
- Diesel exhaust, under Protocol 2. A diesel-powered electric generator (Red-D-Arc, Model D302L 3+12 Diesel Welder) operated for 4 hr in the bed of a pickup truck parked adjacent to the opened front door of the house. The generator's electrical output powered a flood light as a load.
- Indoor cooking under Protocol 2. Brown bread was heated in a toaster (two slices at a time) until charred in the same room as the PM monitoring equipment. (Preliminary field sampling in May 2006 at the same location showed that the ratios of UV to IR absorbance of PM from toasting bread and frying eggplant were quite similar to those of wood smoke from a neighbor's fireplace. The weather was much warmer in June, and no wood smoke was detected.)

#### **4.7.3 Calibration of the MEMS PM monitor: Comparison of MEMS PM Monitor Response to Gravimetric Measurements of PM<sub>2.5</sub> and PM<sub>grav</sub>**

As shown in Figure 4.26, comparison of the real-time MEMS PM monitor to gravimetric measurements of ambient PM<sub>2.5</sub> can be made by plotting the average value of  $df/dt$  (over a 4 or 24 hr period) as a function of the gravimetric PM<sub>2.5</sub> average concentration determined from filter sampling. The inset figure at the left of Figure 4.26 shows only the FBAR data for the 24-hr PM<sub>2.5</sub> ambient

measurement periods (open circles). Although these data points lie close to the origin, they appear to have the same relationship to gravimetrically determined PM as for the 4-hr PM<sub>2.5</sub> (solid triangle) and the LBNL chamber results for PM<sub>grav</sub> in ETS (solid circle) described in Section 4.3. Least squares fits to the data yield the same slope for all filter data (0.0025 kHz/min per  $\mu\text{g}/\text{m}^3$ ), in agreement with LBNL chamber results.

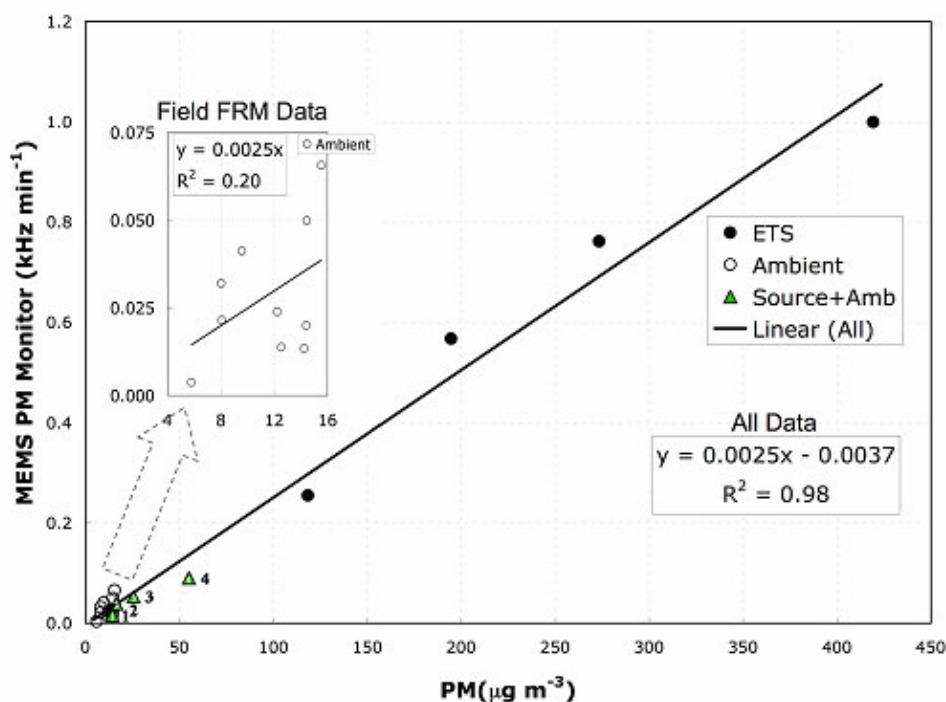


Figure 4.26: Calibration of the MEMS PM monitor based on environmental chamber and field tests. The FBAR signal is plotted on the y-axis as the time-weighted average derivative (kHz/min) for periods during which PM was collected for gravimetric analysis. PM concentrations are plotted on the x-axis: open circles, PM<sub>2.5</sub> determined with the FRM (24 hr, infiltrated ambient air); triangles, PM<sub>2.5</sub> determined with the adapted FRM (4 hr sampling, source-enhanced infiltrated ambient air); and filled circles, PM<sub>grav</sub> (30 min to 4 hr, ETS in the environmental chamber, data of Figure 4.12). The section of ambient PM<sub>2.5</sub> data near the origin of the plot has been expanded into the inset figure on the left. The numbers near the triangles identify the combustion sources as (1) toast, (2) diesel exhaust, (3) ETS, and (4) burnt toast. Least squares fits to the data yield the same slope for all filter data (0.0025 kHz/min per  $\mu\text{g}/\text{m}^3$ ), in agreement with chamber results (Figure 4.12).



The FBAR-derived PM<sub>2.5</sub> limit of detection (LOD) was estimated by Dr. Michael Apte using the Hubaux-Vos detection limit procedure<sup>12</sup>. The method establishes two sensitivity limits: a signal level,  $y_c$ , that determines, within a specified level of confidence, whether the analyte (PM) is present or not, and a detection limit or LOD concentration. Based on the data of Figure 4.26, for the 99% confidence level,  $y_c$  is 9  $\mu\text{g}/\text{m}^3$  and the LOD is 18  $\mu\text{g}/\text{m}^3$ , which satisfies the EPA's Federal Reference Method.

## 4.8 Chapter 4 References

---

<sup>1</sup> J. Wagner, et al., "Environmental tobacco smoke leakage from smoking rooms", *J. Occup. and Environ. Hyg.*, vol. 1, pp. 110–118, 2004.

<sup>2</sup> M.G. Apte, L.A. Gundel, et al., "Indoor measurements of environmental tobacco smoke", Lawrence Berkeley National Laboratory, Final Report to the Tobacco-Related Disease Research Program, Project 6RT-0307, LBNL 49148, 2004.

<sup>3</sup> L.A. Gundel, et al., "Selective monitoring of dilute environmental tobacco smoke in ambient air with other sources", *Proc. 19th Ann. Meeting Amer. Assc. for Aerosol Research*, St. Louis, MO, November 6-10, 2000.

<sup>4</sup> L.A. Gundel and M.G. Apte, Annual Reports to the Tobacco-Related Disease Research Program, Simple Exposure Indicators for Environmental Tobacco Smoke, Project 11RT-0202, 2003-2005.

<sup>5</sup> USEPA 1997, "Ambient Air Monitoring Reference and Equivalent Methods", United States Environmental Protection Agency, Federal Register, 40CFR Parts 50, 53 and 58.

<sup>6</sup> J.-B. Donnet, R.C. Bansal, and M.-J. Wang, *Carbon Black: Science and Technology*, 2<sup>nd</sup> Edition, New York: Marcel Dekker, p. 272, 1993.

- 
- <sup>7</sup> S.J. Martin and G.C. Frye, "Polymer film characterization using quartz resonators", *Proc. Ultrasonics Symp.*, pp. 393-396, 1991.
- <sup>8</sup> J.D. Ferry, *Viscoelastic Properties of Polymers*, New York: John Wiley & Sons, 1970.
- <sup>9</sup> Michael Apte, (private communication), 2006.
- <sup>10</sup> L.A. Gundel and D.A. Lane, "Sorbent-coated diffusion denuders for direct measurement of gas/particle partitioning by semi-volatile organic compounds", in *Advances in Environmental, Industrial and Process Control Technologies. Gas and Particle Partition Measurements of Atmospheric Organic Compounds*, Volume 2, Newark: Gordon and Breach, pp. 287-332, 1999.
- <sup>11</sup> E. Swartz, L. Stockburger, and L. Gundel, "Recovery of semivolatile organic compounds during sample preparation: implications for characterization of airborne particulate matter", *Env. Sci. Technology*, vol. 37, pp. 597-605, 2003.
- <sup>12</sup> A. Hubaux and G. Vos, "Decision and detection limits for linear calibration curves", *Anal. Chem.*, vol. 42, no. 8, pp. 849-855, 1970.

## 5 Conclusions

A compact and sensitive MEMS-based monitor for airborne particles has been designed, fabricated and successfully tested in both an environmental chamber and a dwelling. Challenge aerosols during testing included ETS, diesel, wood smoke, and PM from cooking (eggplant and toast). The prototype monitor is characterized by a minimum detectable added mass of about one picogram. Based on data collected inside an occupied residence, calibrated against the PM<sub>2.5</sub> Federal Reference Method, the limit of detection of the device was  $18 \mu\text{g} / \text{m}^3$ . The FBAR oscillator output frequency was tremendously sensitive to temperature fluctuations ( $-24 \text{ ppm} / ^\circ\text{C}$ ), but simple thermal monitoring and real-time temperature compensation adequately corrected for thermal drift on the time scale of minutes.

The monitor's volume, weight, and power consumption are 114 g,  $250 \text{ cm}^3$ , and no more than 100 mW, respectively. A reduction of the weight and volume by a factor of at least five is readily possible. This device currently contains four selectable deposition and mass-sensing elements, however this number could be increased to further extend the useful life of the instrument.

The primary limitation of the FBAR mass sensor LOD is its TCF. As shown in the literature, the TCF could be reduced to perhaps  $1 - 2 \text{ ppm} / ^\circ\text{C}$  by the addition of an silicon-dioxide layer. This improvement could translate into a twenty-fold improvement in sensitivity, which is equivalent to a LOD of less than  $1 \mu\text{g} / \text{m}^3$  or a mass resolution of about 50 fg.